Universität Hamburg

Study of Kinematic Distributions in W Boson and $D^{(*)}$ Meson Production in pp Collisions

Bachelor Thesis

submitted by
Birger J. M. Bigalke

Institute of Experimental Physics
MIN Faculty, Department of Physics
University of Hamburg

16 April 2024

Supervisors

1. Supervisor: **Professor Kerstin Tackmann**
   University of Hamburg/DESY
   Faculty of Mathematics, Informatics and Natural Sciences/ATLAS group
   Department of Physics - Institute of Experimental Physics

2. Supervisor: **Professor Marjorie Shapiro**
   University of California, Berkeley/Lawrence Berkeley National Laboratory
   Physics faculty/ATLAS group
   Department of Physics

Abstract

The production of a W boson in association with a charm quark is a valuable process to study the relatively unconstrained strange quark parton distribution function of the proton. This work presents an analysis of gluon splitting as an important but not well understood background process to $W + c$ production.
The W boson and the D^+ meson or D^* meson, collectively referred to as $D^{(*)}$ meson, arising from the hadronization of the charm quark, have opposite-sign charge (OS), while gluon splitting has no preferred charge relation. Therefore, Monte Carlo generated predictions of gluon splitting processes are studied using the ratio of SS (same-sign charge) to the difference between OS and SS distributions.
Differential cross sections as a function of the transverse momentum of the $D^{(*)}$ meson, $p_T^{D^{(*)}}$, the absolute pseudorapidity of the $D^{(*)}$ meson, $|\eta(D^{(*)})|$, and the azimuthal angle between the charged lepton and the $D^{(*)}$ meson, $\Delta\phi(\ell, D^{(*)})$, are presented using Monte Carlo generated data. These Monte Carlo samples show that gluon splitting, in comparison to the direct $W + c$ production processes, has dominantly lower $p_T^{D^{(*)}}$, and that the contribution of gluon splitting is enhanced for larger $|\eta(D^{(*)})|$ and for smaller $\Delta\phi(\ell, D^{(*)})$. Furthermore, the two generators `Sherpa_2.2.11` and `MadGraph5_aMCatNLO` are compared. It is shown that `MadGraph` predicts less gluon splitting than `Sherpa` for low $p_T^{D^{(*)}}$ and high $\Delta\phi(\ell, D^{(*)})$ and also that the two generators make different predictions for gluon splitting in the observable $|\eta(D^{(*)})|$.

Zusammenfasssung

Die Produktion eines W-Bosons in Assoziation mit einem Charm-Quark ist ein nützlicher Prozess, um die relativ unbekannte Strange-Quark-Partondichtefunktion des Protons zu untersuchen. In dieser Arbeit wird eine Analyse von Gluonsplitting als wichtiger, aber nicht gut verstandener Hintergrundprozess der $W + c$-Produktion vorgestellt.

Das W-Boson und das aus der Hadronisierung des Charm-Quarks entstehende D^+-Meson oder D^*-Meson, insgesamt als $D^{(*)}$-Meson bezeichnet, haben eine Ladung mit entgegengesetztem Vorzeichen (opposite-sign, OS), während das Gluonsplitting keine bevorzugte Ladungsbeziehung hat. Daher werden Monte-Carlo-generierte Vorhersagen von Prozessen von Gluonsplitting anhand des Verhältnisses von SS (same-sign, Ladung mit gleichem Vorzeichen) zur Differenz zwischen OS- und SS-Verteilungen untersucht.

Differenzielle Wirkungsquerschnitte als Funktion des Transversalimpulses des $D^{(*)}$-Mesons, $p_T^{D^{(*)}}$, der abslouten Pseudorapidität des $D^{(*)}$-Mesons, $|\eta(D^{(*)})|$, und des azimutalen Winkels zwischen dem geladenen Lepton und dem $D^{(*)}$-Meson, $\Delta\phi(\ell, D^{(*)})$, werden anhand von Monte-Carlo-generierten Daten präsentiert. Diese Monte-Carlo-Daten zeigen, dass das Gluonsplitting im Vergleich zu den direkten $W + c$-Produktionsprozessen überwiegend niedrige $p_T^{D^{(*)}}$ hat, dass der Beitrag des Gluonsplittings für größere $|\eta(D^{(*)})|$ verstärkt wird und dass das Gluonsplitting hauptsächlich bei kleineren $\Delta\phi(\ell, D^{(*)})$ auftritt.

Außerdem werden die beiden Generatoren `Sherpa_2.2.11` und `MadGraph5_aMCatNLO` verglichen. Es wird gezeigt, dass `MadGraph` für niedrige $p_T^{D^{(*)}}$ und hohe $\Delta\phi(\ell, D^{(*)})$ weniger Gluonsplitting vorhersagt als `Sherpa` und dass die beiden Generatoren auch unterschiedliche Vorhersagen für Gluonsplitting in der Beobachtungsgröße $|\eta(D^{(*)})|$ machen.

Contents

1 Introduction

The work presented here is primarily motived by and follows the methodology developed in Reference [1].

The internal dynamics of protons are complicated, because they are determined by the quarks' exchanging gluons, and interacting with various vacuum condensates [2]. The most common approach to better understand the intrinsic structure of protons are parton distribution functions (PDFs). The PDFs describe the momentum distributions of quarks and gluons within nucleons; parton distribution functions are explained in more detail in Section 3.1 and 3.2. The general theoretical framework, the Standard Model of particle physics, is explained in Section 2.
Currently, there is limited information available on the PDF of strange quarks within the proton. The sea distributions for the three light quarks, up, down, and strange, may be equivalent due to flavor $SU(3)$ symmetry. Alternatively, the strange quark distribution might be suppressed due to its larger mass. Current understanding of the strange PDF is primarily based on measurements of deep-inelastic lepton-proton scattering [3, 4] and charged-current neutrino scattering [5–7], as well as vector-boson measurements conducted at the Large Hadron Collider [8] such as W^+, W^- and Z/γ^* production [9]. However, the constraints on the strange quark and antiquark PDFs are considerably weaker compared to those on the up and down sea quarks and antiquarks [10].

It was suggested that proton-proton collision events involving a W boson and a charmed hadron could serve as a means to measure the strange parton distribution function of protons [11, 12]. The Tevatron particle accelerator was where the first observation of $W + c$ production occurred [13]. Both the ATLAS and CMS experiments at the Large Hadron Collider have conducted measurements using data collected at $\sqrt{s} = 7\,\text{TeV}$ [14, 15]. Additionally, CMS has conducted measurements using data from collisions at $\sqrt{s} = 13\,\text{TeV}$ [16]. The LHCb collaboration has also performed measurements of $W + c$ production in the forward region [17]. The identification of the charm quark or antiquark is achieved in these measurements either by the presence of a jet of particles containing a secondary vertex, or by the explicit reconstruction of a D^+ or D^{*+} meson or its charge conjugate, collectively referred to as $D^{(*)}$.

The analysis described in this work relies as aforementioned on parts of the analysis presented in Reference [1], which details a study of W boson production alongside a $D^{(*)}$ meson, utilizing data from proton-proton collisions at a center-of-mass energy of $\sqrt{s} = 13\,\text{TeV}$, with an integrated luminosity of $140\,\text{fb}^{-1}$. These data presented in Reference [1] were

recorded by the ATLAS detector at the Large Hadron Collider.
In this thesis, the analysis which is presented in Section 6, is a truth level analysis, i.e. it uses data samples produced using showering Monte Carlo generators, which are explained in Section 5, to study a process called gluon splitting in the $W + D^{(*)}$ production. Nevertheless, both the Large Hadron Collider and the ATLAS experiment are presented in Section 4, because the fiducial cuts, i.e. the object selection (see Section 6.1), are determined by the detector, and the observables themselves were selected on the basis of their measurability at the ATLAS detector. In general, the work presented here was carried out within the framework of the ATLAS collaboration, e.g. data generated for the ATLAS collaboration were used.

Gluon splitting is an important background process of $W + c$ production but it is not well understood. This work aims to gain knowledge about gluon splitting examining the kinematic distribution of this production for three different variables: the transverse momentum of the $D^{(*)}$ meson, $p_T^{D^{(*)}}$, the absolute pseudorapidtiy of the $D^{(*)}$ meson, $|\eta(D^*)|$, and the azimuthal angle between the charged lepton an the $D^{(*)}$ meson, $\Delta\phi(\ell, D^{(*)})$.
The W boson and the $D^{(*)}$ meson have opposite-sign charge (OS), while gluon splitting has no preferred charge relation. Therefore, gluon splitting processes are extracted by the ratio of SS to the difference between OS and same-sign (SS) distributions. This is not possible in $Z + D^{(*)}$ production which is another reason why it is relevant to gain more knowledge about gluon splitting.

Furthermore, the two generators `Sherpa_2.2.11` [18] and `MadGraph5_aMCatNLO` [19] are compared in regards to their predictions on gluon splitting. For this, the ratio of the aforementioned ratio between the two different generators is computed in Section 6.6.

2 The Standard Model of Particle Physics

The surroundings and organisms seem to consist of atoms with a central nucleus and a surrounding shell of electrons, held together by either electric forces - or photons. The nuclei in turn are made up of protons and neutrons, whose numbers essentially determine the mass of atoms, their electric charge and, in part, the chemistry of atoms.

This worldview is undoubtedly too simplistic and not entirely accurate. Starting in the 1930s, a new perspective emerged through experimental discoveries in cosmic rays [20], later mainly at high-energy particle accelerators [21] and increasingly through theoretical insights [22]. This perspective is now known as the Standard Model of particle physics. Among these discoveries is the concept of antimatter [23–25], the identification of a total of twelve fundamental particles (and their antiparticles) sharing similar properties with the electron and over a hundred other fermions that, much like protons and neutrons, can be interpreted as bound states of entities called quarks [26], which are among the aforementioned twelve fundamental particles. From these observations, it was initially theorized that photons are merely the simplest manifestation of a broader concept rooted in symmetries of nature. This concept suggests that in addition to the electromagnetic force, two more fundamental forces can be formulated: the weak [27] and the strong forces. Although formulated in a manner similar to electromagnetism, these forces possess fundamentally different properties. The weak force allows transformations between different types of particles, while the strong force binds quarks into protons and neutrons, which in turn form atomic nuclei [28].

A fundamental insight is that the concept of symmetries enables predictions of natural laws and requires relationships between the numerical values of seemingly unrelated fundamental constants [29]. Many of these predictions have later been experimentally confirmed, including the discovery of the Higgs boson in the year 2012 [30].

However, the current form of the Standard Model is not capable of predicting or explaining how the universe evolved from the hot phase after the Big Bang to its current state. Crucial components are missing, such as an explanation for the large asymmetry in the amount of matter and antimatter, the existence of significant amounts of dark matter, and possibly dark energy [31]. Additionally, effects of gravity, which has not been incorporated into the Standard Model so far, might play a role. These extensions of the Standard Model may have important effects in energy regimes beyond what is currently achievable in laboratories [32]. Therefore, the Standard Model should be understood as an approximation to a more comprehensive theory. Nevertheless, it is already accurate enough to predict experimental observations within their current precision and at currently accessible energies [33].

The primary objective of this thesis is to investigate the kinematic distributions associated with W boson and $D^{(*)}$ meson production in proton-proton collisions, with the aim of enhancing understanding of the background phenomenon of gluon splitting. To accomplish this goal, it is crucial to establish the foundational principles of the theoretical framework within which the analysis is conducted, namely, the Standard Model of particle physics.

2.1 Elementary particles and their interactions

In the framework of the Standard Model (SM), particles are conceptualized as local excitations emerging from quantum fields pervading space. Within the explored energy range to date, the fundamental constituents of matter are deemed elementary particles, denoted as point-like entities incapable of further decomposition.

These particles are characterized by their intrinsic properties, such as spin, mass, and charge quantum numbers. Particles are classified into fermions and bosons based on their spin. Fermions have half-integer spin (s = 1/2, 3/2 ...) and exhibit an anti-symmetric wave function, following Fermi-Dirac statistics and the Pauli exclusion principle. The Pauli principle states that two identical fermions cannot occupy the same quantum state simultaneously. Bosons have a symmetric wave function, which means they follow Bose-Einstein statistics and allow multiple bosons to occupy the same quantum state. In the Standard Model, only elementary fermions and bosons with spin-1/2 and spin-0,1, respectively, are recognized. The particle's charge quantum numbers determine its participation in various interactions.

Figure 1 shows a schematic representation of the elementary particles in the Standard Model. This section provides a brief overview of these particles, based on the descriptions in Reference [26].

2.1.1 Fermions

In the Standard Model, fermions are identified as the fundamental building blocks of matter. This designation arises from their intrinsic property of having a spin of 1/2 and obeying the Pauli exclusion principle. As fermions, quarks and leptons exhibit characteristics that allow for the formation of complex structures such as nuclei and atoms. Unlike bosons (see Section 2.1.2), which can occupy the same quantum state, fermions must obey the Pauli exclusion principle, leading to the formation of distinct energy levels and enabling

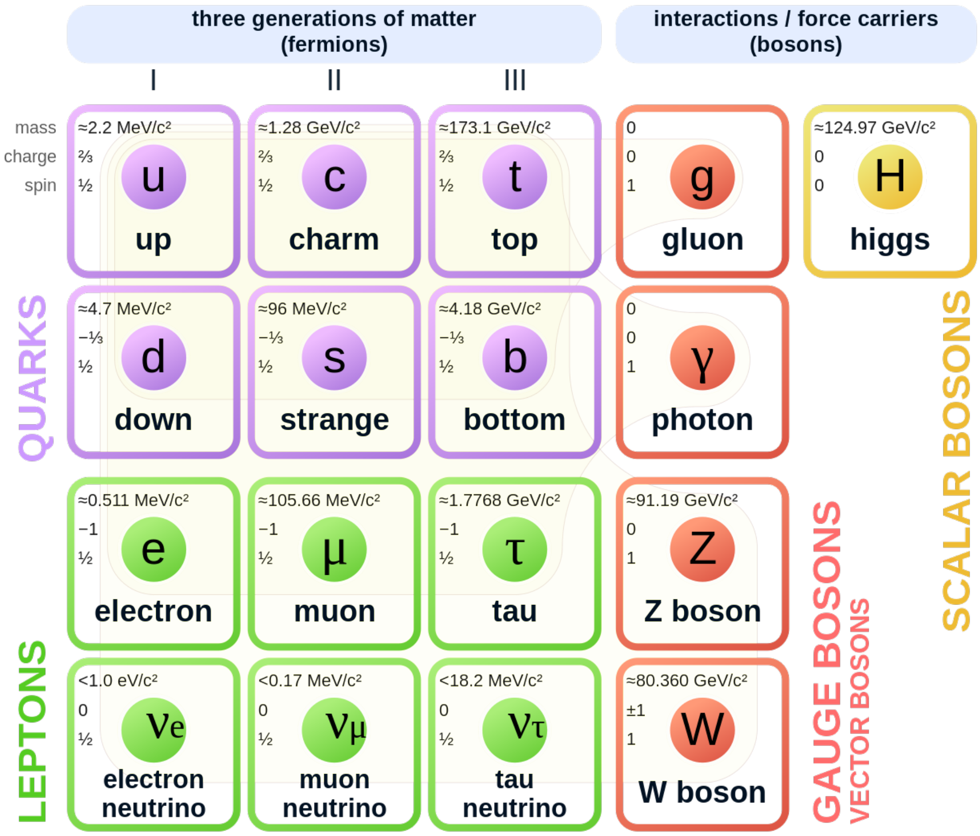

Figure 1: Overview of the particles of the Standard Model of particle physics [34]. They are categorized into fermions and bosons, which can be further categorized into gauge bosons and scalar bosons for the bosons and quarks and leptons for the fermions. Fermions can also be divided into generations of matter, which are each heavier than the previous one. Furthermore, the subtly visible yellow outline indicates which fermions couple to which bosons.

the creation of stable atomic structures.

Fermions are divided into two main groups based on their participation in interactions: leptons and quarks.

The lepton group consists of fermions that only interact through the electroweak force and do not participate in the strong interaction. This group includes three electrically charged particles: the electron (e), the muon (μ), and the tau (τ), as well as their electrically neutral counterparts, known as neutrinos. Specifically, the neutrino subset within this group consists of the electron neutrino (ν_e), the muon neutrino (ν_μ), and the tau neutrino (ν_τ). The electron, muon, and tau have identical negative electrical charges, corresponding to

the elementary charge. In contrast, neutrinos lack any electrical charge.
Thus, charged leptons feel both the electromagnetic and weak forces while the neutrinos feel only the weak force. However, as explained in Section 2.3, the charged current weak interactions are left-handed. The neutral current weak interactions, on the other hand, include both left- and right-handed couplings. Though right-handed neutrinos do not exist in the Standard Model. This requires distinguishing between left-handed and right-handed leptons. Left-handed leptons are organized into three doublets or generations based on the weak isospin quantum number, $T_3 = \pm 1/2$. Each doublet comprises one charged lepton and its corresponding neutrino. While both left-handed and right-handed charged leptons participate in weak interactions, only the charged leptons serve as weak isosinglets. Right-handed neutrinos, although hypothesized in some extensions of the Standard Model [35], have not been detected in experiments and are not included in the conventional framework of the Standard Model. In the SM framework, neutrinos are considered massless. Unlike other fermions, which acquire mass through interactions with the Higgs field (see Section 2.3.2), neutrinos do not directly interact with the Higgs field. The absence of right-handed neutrinos in the SM prevents the possibility of a Higgs-induced mass for neutrinos [36]. However, the electron, muon, and tau have significant masses of approximately $m_e \approx 0.511\,\text{MeV}$, $M_\mu \approx 105.7\,\text{MeV}$, and $m_\tau \approx 1777\,\text{MeV}$, respectively. Table 1 provides a summary of the properties of the leptons.

Table 1: The leptons in the Standard Model are presented alongside their corresponding mass, electric charge, allowable chiralities and the third component of weak isospin. The numerical values for these attributes are obtained from Reference [22].

Lepton			$Q/\lvert e\rvert$	Chirality
electron (e^-) 0.51 MeV	muon (μ^-) 105.66 MeV	tau (τ^-) 1776.86 $\pm$0.12 MeV	-1	left right
electron neutrino (ν_e) < 1.1 eV	muon neutrino (ν_μ) < 0.19 MeV	tau neutrino (ν_τ) < 18.2 MeV	0	left

Quarks are fermions that participate in both the electroweak and strong interactions. This group consists of three up-type quarks, namely up (u), charm (c) and top (t), as well as three down-type quarks, namely down (d), strange (s) and bottom (b). Unlike leptons, quarks have a fractional electrical charge, with up-type quarks having a charge of $Q = +2/3$ and down-type quarks carrying a charge of $Q = -1/3$.
Quarks, like leptons, engage in weak interactions and are organized into three generations

based on the third component of weak isospin. Left-handed quarks form doublets, pairing an up- and a down-type quark, with $T_3 = \pm 1/2$. Conversely, right-handed quarks exist as singlets with $T_3 = 0$.

In addition to the electroweak interactions, quarks possess another attribute known as color charge, which enables them to interact via the strong force. The color charge is exhibited in three forms: red, green, and blue. Section 2.4 provides a comprehensive explanation of Quantum Chromodynamics, the theory that supports the strong interaction in the Standard Model.

Quarks are unable to exist independently due to confinement within the strong interaction and are instead confined within composite bound states called hadrons. Hadrons are classified into two main categories: baryons, which consist of three quarks (or antiquarks), and mesons, which are composed of a quark-antiquark pair. In addition, more exotic forms of hadrons, such as pentaquarks (consisting of three quarks and a quark-antiquark pair) and tetraquarks (composed of two quark-antiquark pairs), have also been observed through experiments [37] [38]. The top quark is the heaviest particle within the Standard Model. Its mass is so significant that its mean lifetime is shorter than the time required for hadronization to occur. As a result, bound states, i.e. hadrons, cannot form before its decay. Table 2 presents details on the masses and properties of the quarks. It is important to note that each fermionic particle in the Standard Model has an antiparticle with an identical mass but opposite quantum numbers, including electric charge, weak isospin, and color charge.

Table 2: The quarks in the Standard Model are presented alongside their corresponding mass, electric charge, allowable chiralities and the third component of weak isospin. The numerical values for these attributes are obtained from Reference [22].

Quark			$Q/\lvert e \rvert$	Chirality
up (u) $2.16^{+0.49}_{-0.26}$ MeV	charm (c) 1.27 ± 0.02 GeV	top (t) 172.4 ± 0.7 GeV	$+\frac{2}{3}$	left right
down (d) $4.67^{+0.48}_{-0.17}$ MeV	strange (s) 93^{+11}_{-5} MeV	bottom (b) $4.18^{+0.03}_{-0.02}$ MeV	$-\frac{1}{3}$	left right

2.1.2 Gauge bosons

In the Standard Model, particles interact through elementary particles called gauge bosons, which have a spin of 1. These bosons follow Bose-Einstein statistics, allowing an unlimited number of them to occupy the same quantum state. The mediators are closely connected to the symmetry groups that govern the three fundamental interactions in the Standard

Model: the unified electromagnetic and weak interactions, described by the $SU(2)_L \times U(1)_Y$ transformation group and the strong interaction, described by the $SU(3)_C$ group. Table 3 compiles the corresponding force mediators with their associated mass and electric charge. The strength of each interaction is determined by its corresponding coupling constant.

Table 3: The bosons in the Standard Model are presented alongside their corresponding force, mass and electric charge. The numerical values for these attributes are obtained from Reference [22].

	Force	Field Particles	Mass in GeV	$Q/\|e\|$
Gauge bosons (spin-1)	electromagnetic	γ	0	0
	weak	$W^{\pm}$	80.4	± 1
	weak	Z^0	91.2	0
	strong	g	0	0
Scalar boson (spin-0)	Higgs	H	125.3	0

The electromagnetic force governs a wide range of physical interactions, including molecular structures, chemical reactions, and various electromagnetic phenomena. All particles with electric charge interact through this force. In regions of phase space where the weak interaction can be neglected, its behavior is explained by quantum electrodynamics (see Section 2.2), with the photon serving as the mediating gauge boson. The photon is a particle that has no electric charge or mass. In quantum electrodynamics it arises from the imposition of local $U(1)_{\mathrm{EM}}$ symmetry on the free Lagrangian of a fermionic field. However, in the framework of the electroweak theory (see Section 2.3), the photon is a linear combination of the $U(1)$ and the $SU(2)_L$ fields with weak isospin $I_3 = 0$. Because it has no charge or mass, the electromagnetic force it carries is theoretically infinite in range.
The weak force is essential in various phenomena, such as the radioactive decay of subatomic particles and nuclear fusion reactions. Within the Standard Model framework, the weak force is unified with the electromagnetic force, both stemming from the $SU(2)_L \times U(1)_Y$ transformation symmetry. The weak interaction is in quantum electrodynamics mediated by three massive gauge bosons: the electrically charged $W^{\pm}$ bosons and the electrically neutral Z^0 boson. Section 2.3.1 provides an explanation of electroweak unification. Fermions interact with weak bosons through the third component of weak isospin. The weak interaction's range is limited to subnuclear scales due to the significant mass of the $W^{\pm}$ and Z^0 bosons.
The strong force is the fundamental interaction responsible for binding quarks and gluons

together to form protons, neutrons, and other hadrons. It also governs the strong nuclear force, which holds the protons and neutrons within atomic nuclei together through the exchange of pions. The theory of quantum chromodynamics elucidates the strong interaction within the framework of the Standard Model, as detailed in Section 2.4. The Lagrangian imposes the $SU(3)_C$ symmetry on this theory. The interaction is mediated by an octet of gluons, which are electrically neutral and massless. Gluons carry both the charge and anti-charge of the force they mediate, known as the color charge. They interact with colored-charged fermions (quarks) and with each other. The strength of the interaction is low at high energy but high at low energy due to the self-interaction of gluons. Therefore, particles with color charge are free at high energies but cannot exist independently due to confinement.

2.1.3 The Higgs boson

The Lagrangian of the Standard Model requires that all fermions and gauge bosons be massless due to its invariance under $SU(2)_L \times U(1)_Y$. However, experimental evidence contradicts this prediction [39]. Therefore, a mechanism is necessary to endow particles with mass without violating the original gauge invariance of the model. The Higgs mechanism accomplishes this in the Standard Model, based on the spontaneous electroweak symmetry breaking (EWSB) mechanism. Although the vacuum state (the ground state of the system) has been altered to no longer exhibit this invariance, EWSB still preserves the model's invariance to different symmetry groups. Section 2.3.2 provides a detailed description of the EWSB process.

The Higgs boson arises from the excitation of the Higgs field. It is a massive spin-0 boson that interacts with all massive particles, including itself. The strength of this interaction is proportional to the mass of the particle. In 2012, the ATLAS [30] and CMS [40] collaborations observed the Higgs boson, which completed the discovery of all particles in the Standard Model. Table 3 provides a summary of its properties.

2.2 Quantum Electrodynamics

This section presents an overview of quantum field theory (QFT) by explaining how electromagnetism is formulated within this mathematical framework; this formulation is known as quantum electrodynamics (QED). The derivation of the electroweak theory (see Section 2.3) and quantum chromodynamics (see Section 2.4) follows a similar methodology. Therefore, detailed derivations are not repeated in the corresponding sections. The aim is to clarify the most important physical implications of each theory. The description of

QED presented here is based on the explanations provided in Reference [2].
QED was first formulated in the 1940s by R. Feynman [41], J. Schwinger [42] and S.I. Tomonaga [43], each independently. QED has successfully predicted phenomena such as the Lamb shift in hydrogen energy levels [44] and the electron's anomalous magnetic dipole moment [45]. The principles that form the basis of this accomplished theory are also used in other QFTs that explain the weak and strong interactions.

2.2.1 The QED Lagrangian

In QFT, particles are represented as quantum fields. The equations governing the behavior of these fields are derived from the Euler-Lagrange equations, which are obtained by applying the principle of stationary action to the Lagrangian density. For a single field $\phi(x)$, the Euler-Lagrange equation is expressed as:

$$\partial_\mu \left(\frac{\partial \mathcal{L}}{\partial(\partial_\mu \phi)} \right) - \frac{\partial \mathcal{L}}{\partial \phi} = 0, \tag{2.1}$$

where $\mathcal{L}$ is the Lagrangian of the theory and ∂_μ represents the four-gradient. The term "Lagrangian density" will be referred to as "Lagrangian" from now on, as is common practice in QFT.
After determining the Lagrangian of the theory, the equations of motion for all involved fields can be derived. This provides a comprehensive understanding of particle behavior within the framework. QED aims to clarify the interactions between electrically charged particles and the electromagnetic field. The QED Lagrangian is formulated by starting with the equation of motion that governs a free, massive, charged particle with spin-1/2, which is known as the Dirac equation:

$$(i\gamma^\mu \partial_\mu - m)\psi(x) = 0, \tag{2.2}$$

Here, $\psi(x)$, a four-component spinor, represents the quantum field associated with the particle, m denotes its mass, and γ^μ refers to the Dirac matrices defined in four-dimensional Minkowski space. In this section, all equations utilize the Einstein notation, which implies a summation over repeated index variables.
The foundational Lagrangian governing the Dirac theory, which yields the Dirac equation of motion through the corresponding Euler-Lagrange equations for $\psi(x)$ and for its adjoint $\bar{\psi} = \psi^\dagger(x)\gamma^0$, is as follows:

$$\mathcal{L} = \bar{\psi}(x)(i\gamma^\mu \partial_\mu)\psi(x) - m\bar{\psi}(x)\psi(x). \tag{2.3}$$

It is evident that this Lagrangian not only maintains Lorentz invariance but also exhibits the abelian $U(1)$ global symmetry, characterized by:

$$\psi(x) \to e^{i\alpha}\psi(x), \tag{2.4}$$
$$\bar{\psi}(x) \to e^{-i\alpha}\bar{\psi}(x). \tag{2.5}$$

The $U(1)$ global symmetry of the Dirac Lagrangian is postulated to be to a local $U(1)$ symmetry (i. e. $\alpha \to \alpha(x)$). However, the original Lagrangian is not invariant due to the presence of the derivative term $\partial_\mu\psi(x)$. To restore invariance, a spin-1 gauge field, $A_\mu(x)$, is introduced, replacing the partial derivative with the gauge covariant derivative:

$$\mathcal{D}_\mu = \partial_\mu + iqA_\mu(x). \tag{2.6}$$

The $A_\mu(x)$ field undergoes transformations under local $U(1)$ transformations, as:

$$A_\mu(x) \to A_\mu(x) - \frac{1}{q}\partial_\mu\alpha(x). \tag{2.7}$$

After incorporating the gauge covariant derivative and the vector field $A_\mu(x)$ into the Dirac Lagrangian, the resulting structure includes an additional term, $-qA_\mu\bar{\psi}\gamma^\mu\psi$, which accounts for the interaction between two fermionic fields mediated by the gauge field. The magnitude of this interaction is determined by the coupling constant q:

$$\begin{aligned} \mathcal{L} &= \bar{\psi}(i\gamma^\mu\mathcal{D}_\mu)\psi - m\bar{\psi}\psi && (2.8)\\ &= \bar{\psi}(i\gamma^\mu\partial_\mu)\psi - m\bar{\psi}\psi - qA_\mu\bar{\psi}\gamma^\mu\psi. && (2.9)\end{aligned}$$

Equation 2.9 specifies the Lagrangian involving the A_μ field, but it does not account for its free propagation. To address this aspect, the starting point involves examining the equation of motion for a free, massive, spin-1 particle, termed as the Proca equation:

$$(\partial_\mu\partial^\mu m_A^2)A^\nu = 0. \tag{2.10}$$

The corresponding Lagrangian integrates the strength field tensor $F^{\mu\nu} = \partial^\mu A^\nu - \partial^\nu A^\mu$:

$$\mathcal{L} = -\frac{1}{4}F^{\mu\nu}F_{\mu\nu} + \frac{1}{2}m_A^2A^\nu A_\nu. \tag{2.11}$$

Equation 2.11 loses its invariance under the local $U(1)$ gauge transformation when the mass term is included. However, if the mass of the vector field is set to zero, the Proca

Lagrangian becomes gauge invariant and transforms into the covariant form of the Maxwell equations. In this form, the A_μ gauge field corresponds to the photon field. Finally, by adding the photon propagation term to Equation 2.11, the Lagrangian of QED reaches its final form:

$$\mathcal{L} = \bar{\psi}(i\gamma^\mu \mathcal{D}_\mu)\psi - m\bar{\psi}\psi - \frac{1}{4}F^{\mu\nu}F_{\mu\nu} \tag{2.12}$$

$$= \bar{\psi}(i\gamma^\mu \partial_\mu)\psi - m\bar{\psi}\psi - q(\bar{\psi}\gamma^\mu\psi)A_\mu - \frac{1}{4}F^{\mu\nu}F_{\mu\nu}. \tag{2.13}$$

Noether's theorem states that a conserved quantity exists for every symmetry present in the Lagrangian. In the case of the abelian $U(1)$ local symmetry within the QED Lagrangian, the conserved current derived from Noether's theorem is represented by $j^\mu = \bar{\psi}\gamma^\mu\psi$, with an associated conserved charge denoted as q. This charge q reflects the strength of the coupling between the fermion fields and the photon field and is recognized as the electric charge linked to the fermionic field.

In summary, the Lagrangian of QED can be constructed by incorporating the equations of motion for massive spin-$\frac{1}{2}$ and spin-1 particles along with gauge invariance under the $U(1)$ local symmetry. This allows for the derivation of all related phenomena.

2.3 Electroweak Interaction

2.3.1 Electroweak Unification

The electroweak theory (EW) unifies the electromagnetic and weak interactions in the SM. It was developed by S. L. Glashow [46], A. Salam and J. C. Ward [47], along with S. Weinberg [48] during the 1960s . The theory is characterized by the symmetry group $SU(2)_L \times U(1)_Y$, where $U(1)$ represents the same symmetry group as in QED in Section 2.2, while $SU(2)_L$ denotes the special unitary group of 2×2 matrices. The conserved quantities associated with $U(1)_Y$ and $SU(2)_L$ are the hypercharge Y and the third component of weak isospin T_3. The Gell-Mann-Nishijima formula explains the relationship between hypercharge, the third component of weak isospin and electromagnetic charge [49]:

$$Q = T_3 + \frac{1}{2}Y. \tag{2.14}$$

The $SU(2)_L$ gauge fields interact exclusively with left-handed fermions, making the Electroweak theory left-chiral. The distinction between left and right-handed particles in the theory is based on the results of the Wu experiment [50], which showed that the weak interaction has no effect on right-handed particles, resulting in a complete violation of parity symmetry.

To express the chirality aspect of the EW theory, the fermion fields are initially broken down into two components: left-handed and right-handed, defined as follows with the product of the four Dirac matrices γ^5:

$$\psi_L(x) = \frac{1}{2}(1 - \gamma^5)\psi(x), \tag{2.15}$$

$$\psi_R(x) = \frac{1}{2}(1 + \gamma^5)\psi(x). \tag{2.16}$$

In non-abelian Yang-Mills gauge theories like $SU(2)_L$, the symmetry governing the Lagrangian is represented by the $U(\theta)$ unitary transformation, where g denotes the gauge coupling strength, T^a stands for the group generators, and θ_a signifies the parameters linked with the unitary transformation:

$$\psi(x) \rightarrow U(\theta)\psi(x), \tag{2.17}$$

$$U(\theta) = e^{igT^a\theta_a}. \tag{2.18}$$

In the case of $SU(2)_L$, the group generators assume the value $T^a = \frac{\sigma^a}{2}$, with σ^i representing the three Pauli matrices, when acting on left-handed fields, while they are defined as $T^a = 0$ when acting on right-handed fields. These generators correspond to three gauge boson fields denoted as $W_i^\mu = W_1^\mu, W_2^\mu, W_3^\mu$. The associated gauge coupling is denoted by g.

The gauge boson field connected with the $U(1)_Y$ symmetry group is represented by B^μ. Being governed by the same $U(1)$ symmetry as the photon field in QED in Section 2.2. Its characteristics are described by the same set of equations. The conserved current linked with this interaction is the hypercharge, with the gauge coupling being denoted by g'.

The Lagrangian obtained by enforcing the $SU(2)_L \times U(1)_Y$ symmetries, excluding the mass terms, incorporates the covariant derivatives acting on left- and right-handed fermion fields, represented as $\mathcal{D}_\mu\psi_L$ and $\mathcal{D}_\mu\psi_R$, while $W_{\mu\nu}^i$ and $B^{\mu\nu}$ denote the strength field tensors corresponding to each gauge boson of the theory:

$$\mathcal{L} = \bar{\psi}_L(i\gamma^\mu\mathcal{D}_\mu)\psi_L + \bar{\psi}_R - (i\gamma^\mu\mathcal{D}_\mu)\psi_R - \frac{1}{4}W_{\mu\nu}^i W^{i,\mu\nu} - \frac{1}{4}B_{\mu\nu}^i B^{i,\mu\nu}; \tag{2.19}$$

$$\mathcal{D}_\mu \psi_L = \left(\partial_\mu - ig\frac{\sigma^i}{2} W_\mu^i - ig'\frac{Y}{2} B_\mu \right) \psi_L, \tag{2.20}$$

$$\mathcal{D}_\mu \psi_R = \left(\partial_\mu - ig'\frac{Y}{2} B_\mu \right) \psi_R; \tag{2.21}$$

$$\tag{2.22}$$

$$B_{\mu\nu} = \partial_\mu B_\nu - \partial_\nu B_\mu, \tag{2.23}$$

$$W_{\mu\nu}^i = \partial_\mu W_\nu^i - \partial_\nu W_\mu^i - g\epsilon^{ijk} W_\mu^j W_\nu^k, \tag{2.24}$$

where in Equation 2.24 the symbol ϵ^{ijk} represents the Levi-Civita tensor. Due to the exclusive influence of $SU(2)_L$ on left-handed particles, the covariant derivatives outlined in the Equations 2.20 and 2.21 exhibit distinct effects on each chirality state. The Lagrangian in Equation 2.19 intentionally omits mass terms for fermion and vector fields to preserve $SU(2)_L$ gauge invariance, which would be compromised otherwise.

The empirically observed charged current interactions arise from a linear combination of the W_μ^1 and W_μ^2 fields:

$$W_\mu^\pm = \frac{1}{\sqrt{2}} \left(W_\mu^1 \mp iW_\mu^2 \right). \tag{2.25}$$

The photon field and the neutral current field of the weak interaction are by contrsast obtained through a rotation of the remaining W_μ^3 and B_μ fields:

$$\begin{pmatrix} A_\mu \\ Z_\mu \end{pmatrix} = \begin{pmatrix} \cos(\theta_W) & -\sin(\theta_W) \\ \sin(\theta_W) & \cos(\theta_W) \end{pmatrix} \begin{pmatrix} B_\mu \\ W_\mu^3 \end{pmatrix}, \tag{2.26}$$

where θ_W represents the Weinberg mixing angle. This angle, expressed in terms of the g and g' couplings, is defined as:

$$\cos(\theta_W) = \frac{g}{\sqrt{g^2 + g'^2}}, \tag{2.27}$$

$$\sin(\theta_W) = \frac{g'}{\sqrt{g^2 + g'^2}}. \tag{2.28}$$

Due to the short range of the weak interaction, it is expected that the $W^\pm$ and Z^0 bosons have mass. However, according to the current formulation of the theory, they are considered to be massless. The following section will discuss the spontaneous symmetry breaking (SSB) mechanism, which is used to introduce masses for the electroweak bosons and fermions within the SM.

2.3.2 Electroweak Symmetry Breaking

The Lagrangian presented in Equation 2.19 for the electroweak theory does not include mass terms to maintain its gauge invariance under $SU(2)_L \times U(1)_Y$ transformations. However, experimental evidence confirms that fermions and the $W^{\pm}$ and Z^0 gauge bosons possess mass. The Higgs-Brout-Englert (HBE) mechanism resolves this apparent contradiction by generating particle masses via SSB. The Lagrangian below expresses the equations governing the dynamics of the new complex scalar field ϕ which forms a doublet under the weak isospin $SU(2)_L$ symmetry:

$$\mathcal{L} = (\mathcal{D}_\mu \phi)^\dagger (\mathcal{D}^\mu \phi) - V(\phi), \tag{2.29}$$

with the Higgs field

$$\phi = \begin{pmatrix} \phi^+ \\ \phi^0 \end{pmatrix} = \frac{1}{2} \begin{pmatrix} \phi_1 + i\phi_2 \\ \phi_3 + i\phi_4 \end{pmatrix} \tag{2.30}$$

and the Higgs potential

$$V(\phi) = \mu^2 |\phi|^2 + \lambda |\phi|^4. \tag{2.31}$$

The Higgs field has four degrees of freedom, represented by the four real scalar fields. The shape of the potential is determined by the values of the real parameters $\mu^2 < 0$, and $\lambda > 0$. It is crucial for λ to be greater than 0 to ensure that the potential remains bounded from below, which guarantees the existence of at least one ground state. If μ^2 were positive, the potential would have a single absolute minimum at $\phi = 0$, which would preclude symmetry breaking. However, since μ^2 is negative, the state where $\phi = 0$ represents an unstable local maximum of the potential. Therefore, the minimum occurs at $\phi \neq 0$, indicating a misalignment between the zero-particle state and the vacuum state. Consequently, the Higgs field exhibits a non-zero vacuum expectation value (VEV), which is denoted as v:

$$\sqrt{-\frac{\mu^2}{2\lambda}} = \frac{v}{2} \neq 0. \tag{2.32}$$

An illustrative depiction of the Higgs potential is presented in Figure 2. In the domain comprising the real and imaginary components of the Higgs field, the potential exhibits symmetry in rotations around the zero-particle state. However, upon positioning the field state at a minimum, the vacuum state no longer maintains this symmetry with the Lagrangian. The Higgs field doublet's ground state can be chosen so that the charged component ϕ^+ has a value of zero, while the neutral component has the vacuum expectation

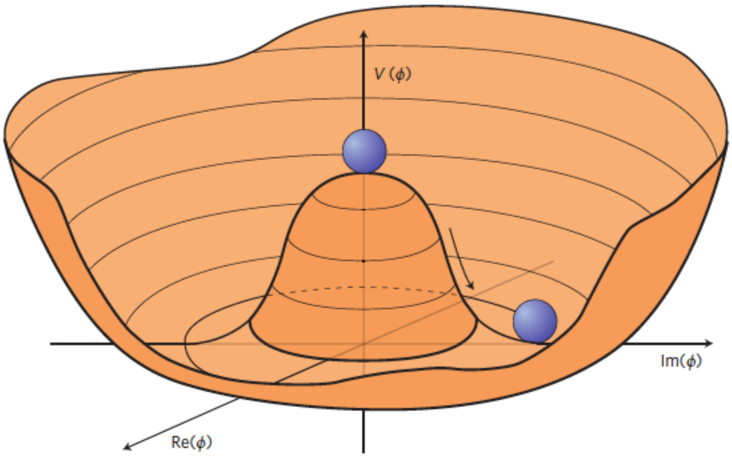

Figure 2: An illustration of the Higgs potential in the case that $\mu^2 < 0$, i.e. that the minimum is at $|\phi|^2 = -\frac{\mu^2}{2\lambda}$ [51]. Selecting any point at the bottom of the potential results in the spontaneous breaking of the rotational $U(1)$ symmetry.

value:

$$\phi_0 = \frac{1}{\sqrt{2}} \begin{pmatrix} 0 \\ v \end{pmatrix}. \tag{2.33}$$

Minor deviations of the scalar field doublet around the vacuum state, in the direction of the zero-particle state, are parameterized as:

$$\phi = \frac{1}{\sqrt{2}} \begin{pmatrix} 0 \\ v + H \end{pmatrix}. \tag{2.34}$$

Here, H represents the Higgs boson and has a mass of $m_H = \sqrt{-\mu^2}$. The assignment of a specific minimum disrupts the $SU(2)_L \times U(1)_Y$ symmetry of the Lagrangian in the vacuum state. The Z^0 and $W^\pm$ bosons of the EW theory assimilate the three remaining degrees of freedom introduced in the ϕ complex scalar field doublet, thereby acquiring mass. The corresponding mass terms in the Lagrangian emerge from incorporating the value of ϕ_0 into the covariant derivative of the EW theory (see Equations 2.20 and 2.21). This results in the subsequent mass terms:

$$\mathcal{L} = \frac{g^2 v^2}{4} W_\mu^+ W^{-,\mu} + \frac{g^2 v^2}{\cos^2(\theta_W)} Z_\mu Z^\mu. \tag{2.35}$$

Thus, the masses of the $W^{\pm}$ and Z^0 boson are:

$$M_{W^{\pm}} = \frac{gv}{2}, \tag{2.36}$$

$$M_Z = \frac{gv}{2\cos(\theta_W)} = \frac{M_W^{\pm}}{\cos(\theta_W)}. \tag{2.37}$$

The process of spontaneous symmetry breaking does not incorporate any quadratic component for the A_μ photon field, thereby maintaining the photon's masslessness.

2.3.3 Masses of fermions

The inclusion of mass terms for the fermionic fields, akin to the weak gauge bosons, disrupts the $SU(2)_L$ symmetry inherent in the Lagrangian. In the SM, to address this issue, fermion masses stem from their interaction with the Higgs field. This interaction is facilitated by coupling the fermions with the Higgs field through a direct linear combination of the fields, known as the Yukawa coupling. The general form of this coupling is outlined in the Lagrangian, where g_Y denotes the coupling constant linked to the interaction:

$$\mathcal{L} = -g_Y \bar{\psi}\phi\psi. \tag{2.38}$$

For all fermions within the SSM, accounting for the absence of right-handed neutrinos in the theory, the complete Yukawa Lagrangian assumes the following structure:

$$\mathcal{L} = -y_l^{ij} l_{L,i}^{\dagger} e_{R,j}\phi - y_q^{ij} q_{L,i}^{\dagger} u_{R,j} i\sigma_2\phi^* - y_q^{ij} q_{L,i}^{\dagger} d_{R,j}. \tag{2.39}$$

Here the index i (or j) pertains to each of the three lepton generations. The matrices y_q^{ij} and y_l^{ij} delineate the Yukawa interactions linking the Higgs field with the quarks and charged leptons, respectively. $e_{R,i}$ represents the right-chiral singlet for weak-isospin leptons, while $u_{R,i}$ (or $d_{R,i}$) designates the right-chiral singlet for up-quarks (or down-quarks) in the weak isospin for each i-th generation. $l_{L,i}$ (or $q_{L,i}$) signifies the left-chiral doublet field for weak-isospin leptons (or quarks) for the i-th generation. σ_2 denotes the second Pauli matrix.
The non-diagonal Yukawa coupling matrices imply that the fermions' mass eigenstates are a linear combination of the electroweak flavor eigenstates. The intermixing among the three quark families is elucidated by the Cabibbo-Kobayashi-Maskawa (CKM) matrix.
Incorporating the SSB mechanism and the VEV of the Higgs field (see Equation 2.34) into Equation 2.39's Lagrangian yields quadratic terms for the fermionic fields. These terms correspond to the fermion fields' mass terms, and the resulting masses for each fermion are

expressed as follows:

$$m_f = y_f \frac{v}{\sqrt{2}}, \tag{2.40}$$

with the Yukawa coupling of the Higgs field y_f. Equation 2.40 suggests that the fermions' mass is directly proportional to their coupling strength with the Higgs boson. Consequently, particles with greater mass exhibit stronger interactions with the Higgs boson.

2.4 Quantum Chromodynamics

2.4.1 Mathematical describtion

In the SM, quantum chromodynamics (QCD) governs the strong interaction. This theory was formulated by H. Fritzsch, H. Leutwyler, and Gell-Mann in the 1970s [52]. It is characterized by the symmetry group $SU(3)_C$, representing the special unitary group of 3×3 matrices. The conserved quantity associated with QCD is the color charge, denoted by the subscript C. QCD distinguishes between three types of color charges: red, green, and blue. Quarks, which carry color charge, are the only fermions that form triplets under the $SU(3)_C$ symmetry group, while leptons, being colorless, form singlets.

The concept of three distinct color quantum numbers was introduced to resolve a discrepancy between the baryon spectrum predicted by the quark model and the spin-statistics theorem. Specifically, the existence of the Δ^{++} baryon, a spin-$\frac{3}{2}$ particle with a charge of $+2|e|$, posed a challenge. It was interpreted as a composite particle consisting of three up quarks, each with zero angular momentum and parallel spins. However, as the Δ^{++} particle is a fermion, its wave function must be anti-symmetric while also being symmetric under the interchange of any quark pairs in space, spin and flavor wave functions. This requirement cannot be satisfied with three identical up quarks. Introducing (at least) three distinct color quantum numbers for the quarks resolved this issue. Since each quark now carries a different color charge, they are no longer identical particles and the problem is resolved within the framework of quantum mechanics.

Similar to the $SU(2)_L$ symmetry group governing the electroweak interaction, the $SU(3)_C$ group in QCD also operates as a non-abelian Yang-Mills gauge theory. Consequently, the symmetry imposed on the Lagrangian is described by the same general $U(\theta)$ unitary transformation as shown in Equation 2.18. Specifically, in the context of $SU(3)_C$, the generators of the group are defined as $T^a = \frac{1}{2}\lambda^a$, where λ^a denotes the Gell-Mann matrices. These matrices adhere to the commutation relation $[\lambda^a, \lambda^b] = if^{abc}\lambda^c$, where f^{abc} represents the structure constants of the $SU(3)$ group. With eight such generators, the associated gauge boson fields, denoted as G^a_μ with a ranging from 1 to 8, correspond to the gluons.

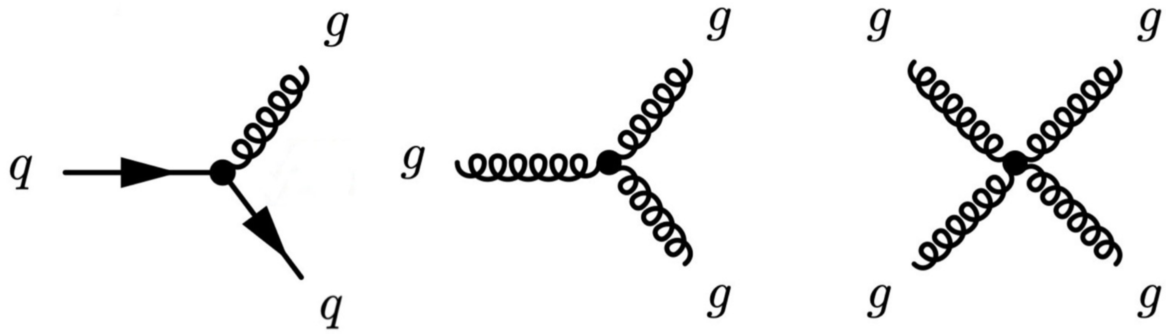

Figure 3: The three interaction vertices of QCD [53].

The Lagrangian derived from imposing the $SU(3)_C$ symmetry is as follows:

$$\mathcal{L} = \bar{\psi}(i\gamma^\mu \mathcal{D}_\mu)\psi - m\bar{\psi}\psi - \frac{1}{4}G_a^{\mu\nu}G_{\mu\nu}^a + \text{h.c.}, \tag{2.41}$$

with the covariant derivative of QCD over fermion fields:

$$\mathcal{D}_\mu \psi = \left(\partial_\mu - ig_s \frac{\lambda^a}{2} G_\mu^a\right)\psi_L, \tag{2.42}$$

and the strong field tensor:

$$G_{\mu\nu}^a = \partial_\mu G_\nu^a - \partial_\nu G_\mu^a - g_s f^{abc} G_\mu^b G_\nu^c. \tag{2.43}$$

The initial component of Equation 2.41 delineates the unhindered movement of quarks and their interaction with gluons, the subsequent element represents the mass factor for fermions and the final portion elucidates the unimpeded movement of a gluon and its interactions with itself. Similar to the fine-structure constant of QED, the gauge coupling linked with the strong interaction is utilized to establish the QCD coupling constant, denoted as:

$$\alpha_s = \frac{g_s^2}{4\pi}. \tag{2.44}$$

Due to the interaction between gluons as illustrated in Figure 3, the gluon field amid a pair of color charges, such as two quarks, takes on a string-like structure with a consistent energy density regardless of the separation distance. As these color charges are pulled apart, there comes a threshold where the field's energy becomes sufficiently high to generate a quark-antiquark pair. Each quark from this new pair then forms a bonded state with one of the original color charges. This phenomenon, recognized as color confinement, renders free observation of color-charged particles unattainable. Nonetheless, the self-interactions of gluons also lead colored particles to exhibit asymptotic freedom, given that the strength of the QCD coupling diminishes at high energies.

2.4.2 Perturbation Theory

Many models formulated within the framework of QFT present equations that are currently unsolvable, indicating that exact analytical solutions for the theory's predictions remain elusive. Both QCD and QED, as well as the entire SM, belong to this category. Consequently, to compute predictions that can be compared with experimental data, researchers usually resort to obtaining solvable approximations of these equations using perturbation theory.

Perturbation theory offers an approximation to the complete solution by expanding around a small parameter within the model, typically the coupling constants in the context of the SM. This approximation remains valid as long as the couplings are small and the degree of similarity between the perturbative calculation and the complete, yet unknown solution depends on the order of the expansion. When considering solely the first order, the calculation is termed as being conducted at the leading order (LO). If the analysis includes the second order as well, it is described as being performed at the next-to-leading order (NLO), and so forth.

The building blocks of perturbative calculations can be distilled into three essential components: interaction vertices, particle propagators, and external lines. Interaction vertices delineate the interactions among multiple particles, while particle propagators quantify the likelihood of a particle to travel from one point in space-time to another. External lines, on the other hand, symbolize the incoming and outgoing particles involved in the interaction. Each of these building blocks corresponds to a distinct mathematical expression derived from the Lagrangian governing the theory. These components form the basis for constructing Feynman diagrams, which graphically represent the various contributions to each order in perturbation theory. Utilizing these diagrams, the Feynman rules offer guidelines for assembling the transition amplitude between any initial and final particle states, facilitating the computation of observable quantities like cross sections and decay rates.

3 $W+$ charm Production

Since this thesis is dedicated to the kinematic distribution in W boson and $D^{(*)}$ meson production, this chapter will take a closer look at $W + D^{(*)}$ production in order to provide an overview of processes that are relevant to the analysis in Section 6. To this end, Section 3.1 first provides a general overview of the physics of proton-proton collisions, in which the concept of the parton distribution function, which is also particularly relevant for this work, is introduced. Subsequently, the $W + D^{(*)}$ production processes will be discussed in Section 3.3.

3.1 Proton-Proton Collisions

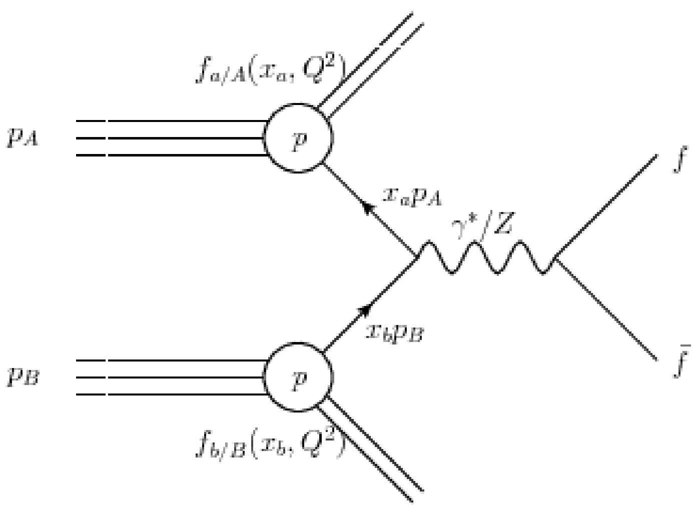

Figure 4: Feynman diagram of a proton-proton collision [54].

Following a collision, particles disperse in all directions. Momentum and energy perpendicular to the beam are termed transverse, denoted as p_T and E_T, respectively. The invariant mass $E_{\text{cms}} = \sqrt{s}$ characterizes the total energy available in the collision. In electron-positron colliders like the Large Electron-Positron Collider (LEP), the colliding entities are elementary, allowing for a well-defined invariant mass of the final state quarks or leptons that participate in the hard scatter, corresponding to the sum of the beam energies.

However, at the Large Hadron Collider (LHC), the colliding particles are protons (see also Section 4.1) composed of two up and one down valence quark, along with gluons and sea quark-antiquark pairs, which is shown in Figure 4. Hence, the proton's momentum must be distributed among its constituents, known as partons. The fraction of the proton momentum carried by each parton is described by the Bjorken variable x which is defined to be the fraction of the protons's momentum that is carried by the parton [55]. While x equals one for elastic scattering, for inelastic reactions $x \in (0, 1)$. As not every parton participates in an interaction, determining the actual E_{cms} of the colliding particles is less straightforward than in electron-positron colliders. The principal quantum numbers of a proton are determined by the valence quarks $p \mathrel{\hat{=}} uud$. Additionally, relativistic quantum field theories permit the continual creation and annihilation of virtual quark-antiquark pairs i.e. spontaneous fluctuations of a quantum field, known as sea quarks, as shown in Figure 6. Their quantum numbers cancel each other out, as they are generated in $q\bar{q}$-pairs. The differential cross section of a reaction depends on the parton distribution functions

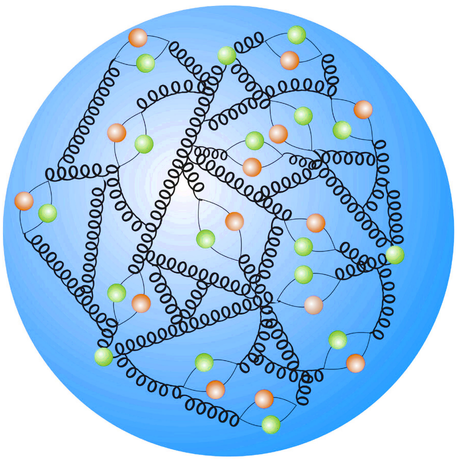

Figure 5: Visualisation of the partons of a proton. The quarks are in green and antiquarks are in red. [56].

(PDFs) $f_i(x)$ of the i-th parton:

$$\frac{d^2\sigma}{dQ^2 dx} \propto \sum_i z_i^2 f_i(x), \tag{3.1}$$

where z_i represents the charge in units of e. The structure function $F_2(x)$ is obtained as the sum in equation 3.1 weighted with x:

$$F_2(x, Q^2) = x \sum_i z_i^2 f_i(x, Q^2). \tag{3.2}$$

In Figure 6, it can be seen that for large values of x, the structure function decreases as Q^2 increases, consistent with the predictions of a simple parton model that includes only valence quarks. However, at low values of x, the structure function increases with higher values for Q^2. This phenomenon is attributed to the presence of sea quarks, anti-quarks, and gluons, which contribute to the increase in F_2 at low x. Scaling violations, on the other hand, arise from the emission of gluons by partons. The resolution of this gluon radiation depends on Q.

The PDFs can be derived from scattering experiments [57]. For proton-proton events, the cross section can be calculated by convolving the PDFs of the two protons with the cross section of the hard parton process $\hat{\sigma}_{ij}$:

$$\sigma_{pp} = \sum_{i,j} \int dx_1 \int dx_2 f_i(x_1, Q^2) f_j(x_2, Q^2) \hat{\sigma}_{ij}(x_1, x_2, Q^2). \tag{3.3}$$

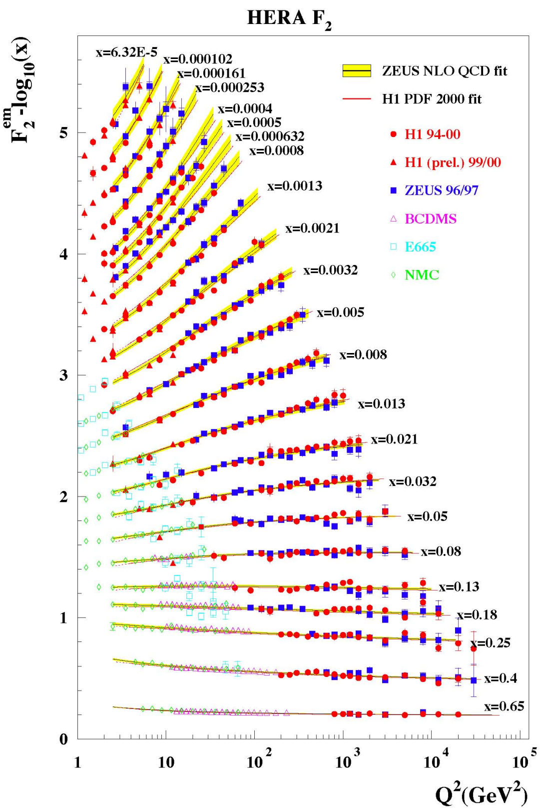

Figure 6: Measured $F_2(Q^2)$ for different x at the Hadron–Electron Ring Accelerator (HERA) at DESY in a fixed target experiment [58]. F_2 decreases with increasing Q^2 for small x, whereas F_2 starts increasing with increasing Q^2 for larger x.

3.2 Strange Quark PDF

Presently, the understanding of the probability distribution functions of strange quarks within the proton is less measured than that of the up and down quarks. There are two potential scenarios regarding the sea distributions of the three light quarks up, down and strange. One possibility is that they are equal, attributed to flavor $SU(3)$ symmetry. Alternatively, the distribution of strange quarks might be suppressed owing to their larger mass. The current insights into the strange PDF primarily stem from observations made during deep-inelastic lepton–proton scattering and charged-current neutrino scattering, along with vector-boson measurements conducted at the Large Hadron Collider. However, limitations on the PDFs of strange quarks and antiquarks are notably looser compared to those on up and down sea quarks and antiquarks.

3.3 W + charm Production Processes

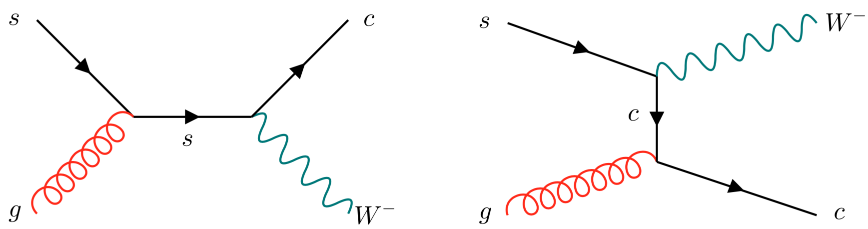

Figure 7: The leading-order Feynman diagrams for the $W^- + c$ production [1].

At lowest order in perturbation theory (see Section 2.4.2), the generation of a W boson coupled with a single charm quark arises from the interaction between a gluon and a down-type quark (either down, strange, or bottom) at leading order, as depicted in Figure 7. The distribution of contributions to the cross-section of $W + c$ production from each of these three distinct quarks depends on their PDFs and the values of the three pertinent terms derived from the Cabbibo–Kobayashi–Maskawa mixing matrix (see Section 2.3.3): V_{cd}, V_{cs}, and V_{cb}. At the Large Hadron Collider, the dominant processes are $gs \to W^-c$ and its charge conjugate, while $gd \to W^-c$ and $g\bar{d} \to W^+\bar{c}$ only contribute approximately 10% and 5% to the W^-c and W^+c rate, respectively. The variance between the contributions from d and $\bar{d}$ can be attributed to the presence of valence down quarks.
The most significant next-to-leading-order contributions are the one-loop corrections to $gs \to W^-c$ and $g\bar{s} \to W^+\bar{c}$, although various other partonic initial states such as qq', gg

and sq or $s\bar{q}$ also play a role.

The production of two different charm hadrons, nameley D^+ and D^*, collectively referred to as $D^{(*)}$, including their charge conjugates, are studied using the following decay modes [1]:

- $D^+ \to K\pi\pi$
- $D^{*+} \to D^0\pi \to K\pi\pi$.

At leading order the W boson and the charm always have an opposite-sign charge symmetry. Gluon splitting is a process whereby a gluon radiates off either of the two quarks, resulting in the production of charm quark pairs (see Figure 8) or bottom quark pairs (see Figure 9), which are considered the signal event. These events have an equal amount of opposite-sign and same-sign charge symmetry.

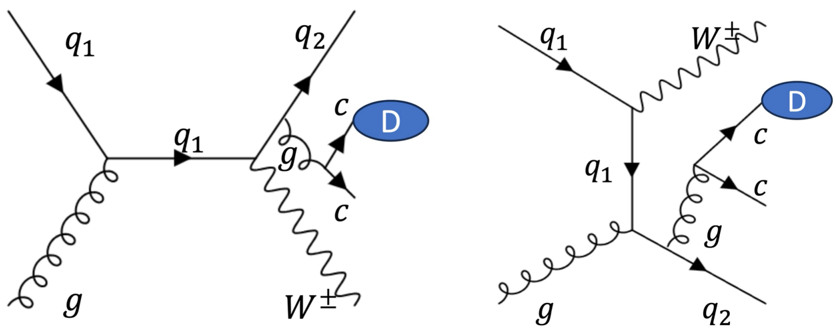

Figure 8: Signal events involving $g \to cc$.

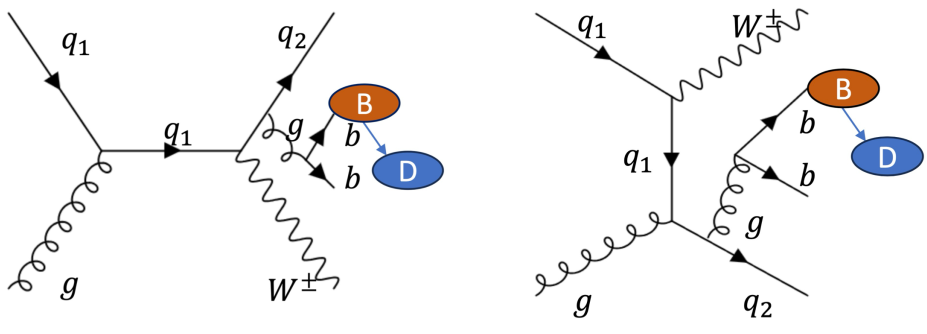

Figure 9: Signal events involving $g \to bb$.

4 Experimental Setup

Particle accelerators are essential tools in scientific engineering, allowing for the study of nature's fundamental components by accelerating subatomic particles to near-light speeds. The Large Hadron Collider (LHC), located at the European Organization for Nuclear Research (CERN) in Geneva, Switzerland, is one of the most prominent technological marvels in this field, leading the way in scientific research and exploration. The LHC is highly regarded for its contribution to understanding the mysteries of the universe.

Particle accelerators, also known as colliders, are examples of precision engineering designed to accelerate subatomic particles to unprecedented speeds. By simulating collisions at energies similar to those of the early universe, these complex devices provide researchers with unparalleled insights into the fundamental building blocks of matter and the forces that govern their interactions.

Since its establishment in 1954, CERN has become a global hub for scientific innovation and collaboration. CERN is a leading institution in particle physics research, promoting international cooperation and advancing human knowledge. Throughout its history, CERN has conducted numerous innovative experiments and developed new technologies, solidifying its position as a top scientific institution.

This chapter provides an examination of the LHC in Section 4.1, followed by a detailed analysis of the ATLAS detector, which is the largest general-purpose particle detector experiment at CERN, as outlined in Section 4.2.

4.1 Large Hadron Collider

The LHC is located near Geneva, Switzerland and is the world's leading synchrotron accelerator with unmatched energy levels. It is situated approximately 100 meters below ground, beneath the French-Swiss border, and occupies the tunnels previously used by its predecessor, the Large Electron-Positron Collider (LEP) experiment [59]. The LHC is a circular tunnel with a circumference of 27 kilometers. It accelerates counter-rotating particle beams that collide at four interaction points (IPs). During early Run I, which began in 2010, the LHC operated at an energy level of $\sqrt{s} = 7\,\text{TeV}$. The design energy of the LHC is $\sqrt{s} = 14\,\text{TeV}$, which is equivalent to $7\,\text{TeV}$ per particle beam. Other important design parameters are summarised in Table 4.

The protons utilized in the LHC's beam originate from hydrogen gas, undergoing a process known as the injection chain [61]. This intricate sequence involves several intermediate accelerators, including the linear accelerator 2 (Linac2), the proton synchrotron booster

Table 4: Important design parameters of the LHC during Run III. Taken from [60].

Design parameters	number
Circumference	26659 m
Dipole operating temperature	1.9 K
Number of magnets	9593
Number of main dipoles	1232
Number of main quadrupoles	392
Number of RF cavities	8 per direction
Energy, protons	6.8 TeV
Energy, ions	2.76 TeV/u
Peak magnetic dipole field	8.3 T
Distance between bunches	7.5 m
Luminosity (protons)	10^{34} cm^{-2} s^{-1}
Number of bunches per proton beam	2808
Number of protons per bunch	1.1×10^{11}
Number of turns per second	11245
Collision rate	40 MHz

(PSB), the proton synchrotron (PS), and the super proton synchrotron (SPS), each elevating the protons' energy levels to as high as 450 GeV before channeling them into the LHC. Subsequently, the protons are injected into the LHC at designated interaction points (IPs), as shown in Figure 10, marking the commencement of collision processes. These IPs are strategic locales along the LHC ring, housing the four primary experiments: ATLAS, CMS, LHCb, and ALICE [62–64]. Among these, ATLAS and CMS serve as comprehensive, multipurpose detectors, collaborating closely to ensure the reliability and reproducibility of experimental outcomes, exemplified notably in the joint discovery of the Higgs boson in 2012 [30, 40]. Additionally, two IPs are dedicated to beam collimation tasks, utilizing the LHC's robust magnetic fields to safeguard the accelerator from stray particles. Notably, the acceleration of proton beams to their ultimate energy of 6.5 TeV is facilitated by superconducting radio-frequency (RF) cavities stationed at a distinct IP [65].

The rate of events recorded per second at each of the detector experiments depends on the luminosity provided by the LHC. Specifically, this is described by the equation

$$\frac{dN}{dt} = \mathcal{L} \cdot \sigma, \tag{4.1}$$

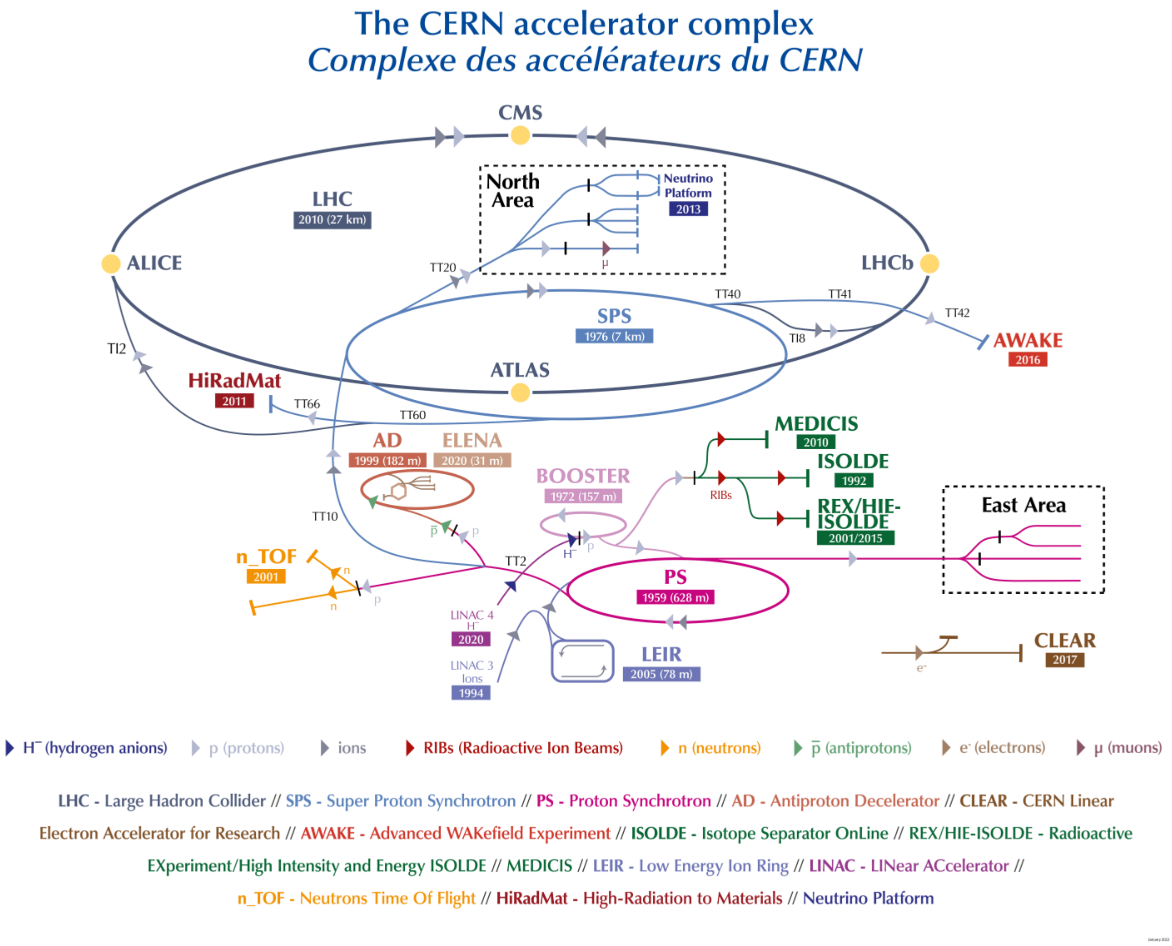

Figure 10: A graphic overview of all accelerators at CERN [66]. The upper legend decodes with different colours what is accelerated. The lower legend explains all acronyms of the different experiments.

where σ is the cross section representing the probability of a particular physics process occurring, and $\mathcal{L}$ is the instantaneous luminosity, which is the rate at which the LHC delivers data based on the properties of the beam and proton bunches. Although the original peak luminosity of the LHC was predicted to be $1 \times 10^{34}\,\mathrm{cm}^{-2}\,\mathrm{s}^{-1}$, the instantaneous luminosity reached levels exceeding $2 \times 10^{34}\,\mathrm{cm}^{-2}\,\mathrm{s}^{-1}$ in 2017 and 2018 due to improvements in the proton beams. Integrating Equation 4.1 over time gives

$$N = \mathcal{L}_{\mathrm{int.}} \cdot \sigma, \tag{4.2}$$

where $\mathcal{L}_{\mathrm{int.}} = \int \mathcal{L} dt$ represents the total data collected over a given period. Consequently, the number of events observed in an experiment N can be predicted for its theoretical cross section σ. For the entirety of the Run II data, the ATLAS experiment certified 140 fb^{-1} of the data provided by the LHC, meeting the quality criteria for use in physics analyses, as shown in Figure 11. Due to the abundance of protons in each beam bunch to achieve the

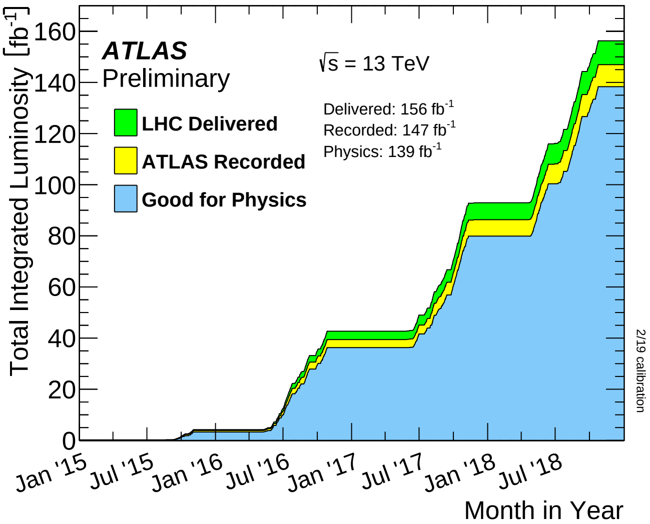

Figure 11: The graph depicts the integrated luminosity over time delivered to (green), recorded by (yellow), and deemed suitable for physics analyses (blue) by the ATLAS experiment [67].

desired luminosity, numerous distinct proton-proton collisions occur at each bundle crossing, a phenomenon known as a pileup. The majority of these collisions produce low-energy particles through soft, inelastic scattering events. Occasionally, collisions involving high momentum transfer take place. Consequently, it is essential for any detector experiment to distinguish between particles produced by the hard scattering process and those produced by pileup in order to detect interesting physics phenomena. The averaged pileup is quantified by the time-averaged number of interactions per bunch crossing, $\langle\mu\rangle$, with the luminosity-weighted distribution of $\langle\mu\rangle$ for each year of ATLAS data collection during Run II shown in Figure 12.

4.2 ATLAS detector

The ATLAS detector is the largest particle detector ever constructed. It measures 46 m in length, 25 m in diameter, and is located approximately 92 m below ground at Point 1. It weighs roughly 7000 t and is one of the two multipurpose detectors at the LHC, the other being the CMS experiment. The ATLAS detector covers almost 4π of solid angle around the pp interaction point with its three layers of subdetectors: the inner detector (ID), the

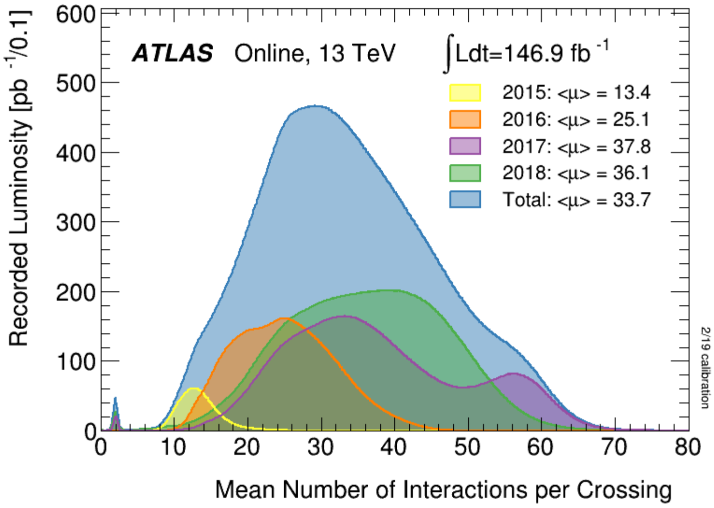

Figure 12: The graph depicts luminosity-weighted sitribution of the mean number of interactions per crossing. [67].

electromagnetic and hadronic calorimeters, and the muon spectrometer (MS) [68]. These subsystems combine to identify specific types of particles sequentially as they traverse the coaxial layers, providing excellent coverage of the wide array of interesting final states that can result from pp collisions. The general geometry of the ATLAS detector is defined by the barrel region and two end-caps, as shown in Figure 13. The following sections discuss the details of each subsystem. Sections 4.2.1 and 4.2.5 provide detailed information on the coordinate system and the ATLAS magnet system, respectively.

4.2.1 Coordinate system

The right-handed coordinate system of the ATLAS detector is located at the interaction point along the beamline at the center of the detector, with the beam direction defining the z-axis. The x-y plane is perpendicular to the beamline and defines the transverse direction, with the positive x-axis pointing from the origin towards the center of the LHC and the positive y-axis pointing from the origin vertically upward towards the surface. The positive z-axis points counterclockwise around the beamline, and with this coordinate system the detector has a forward-backward cylindrical geometry. The coordinates defining the cylindrical geometry are $R = \sqrt{x^2 + y^2}$, the azimuthal angle of the x-axis around the z-axis, ϕ, and z. θ, the spherical polar angle, is the angle from the z-axis and is conveniently

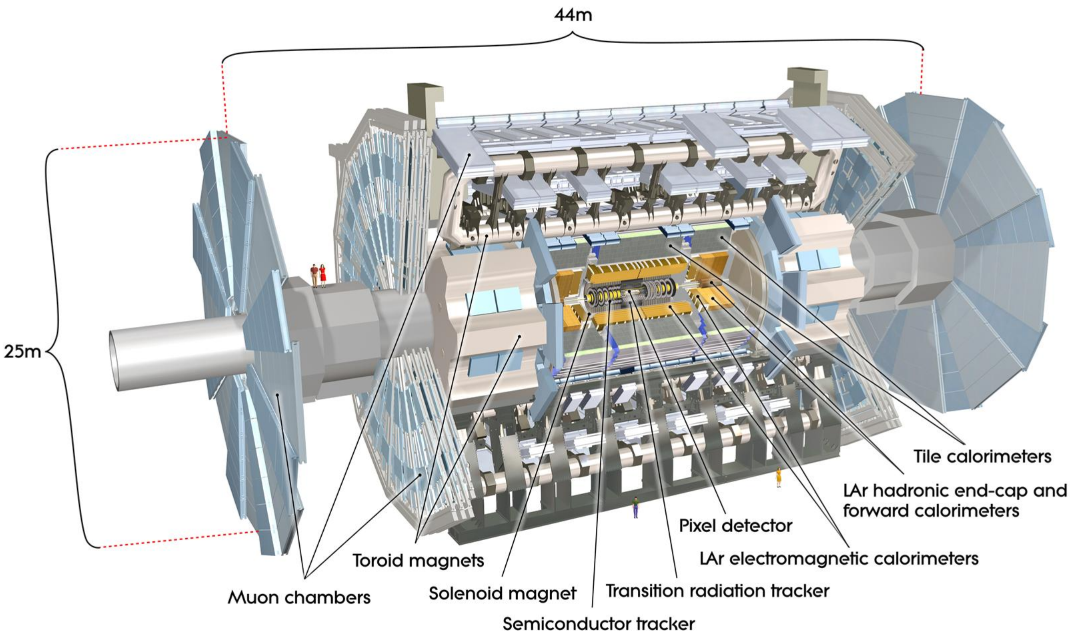

Figure 13: Overview of the ATLAS detector with the different components of the detector and its deimenions [69].

expressed in pseudorapidity. It is defined as

$$\eta = -\ln\left(\tan\left(\frac{\theta}{2}\right)\right). \tag{4.3}$$

This definition takes advantage of cylindrical symmetry, where $\theta = 0$ is along the positive z-axis and $\theta = \frac{\pi}{2}$ is in the transverse plane, while $\eta = 0$ is in the transverse plane and $\eta = \pm\infty$ is along the positive and negative z-axis, respectively, as shown in the Figure 14. Pseudorapidity is also useful because it is Lorentz invariant under boost for massless particles along the z-axis and approximates the rapidity, which is defined as

$$y = \frac{1}{2}\ln\left(\frac{E+p_z}{E-p_z}\right), \tag{4.4}$$

where p_z is the component of the momentum along the beamline, in the massless or ultra-relativistic limit. For any two object system, their angular separation or opening angle is defined as

$$\Delta R = \sqrt{\Delta\eta^2 + \Delta\phi^2}, \tag{4.5}$$

which is also Lorentz invariant for massless particles. Finally, momentum and energy in the transverse direction, $p_T = p\sin(\theta)$ and $E_T = E\sin(\theta)$ respectively, are particularly useful quantities since the initial energy in the transverse plane is zero, and for a momentum- and energy-conserving collision system the summed transverse quantities of all particles after the collision must also vanish [70]. Therefore, it is standard to describe the particles by (p_T, η, ϕ). In this work all of these three variables are of interest.

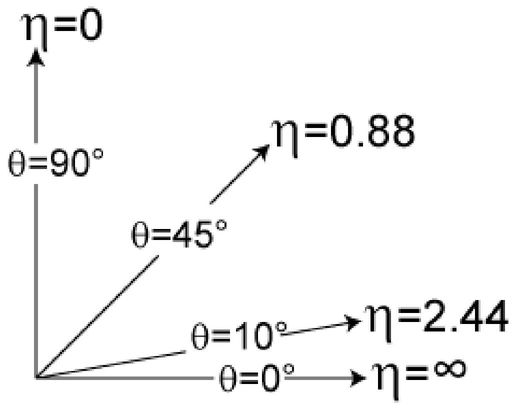

Figure 14: Relationship between azimuthal angle and pseudorapidity [71].

4.2.2 Inner Detector

The inner detector is located within the $|\eta| < 2.5$ range and surrounds the beam pipe. Its main function is to track charged particles as they move within the 2 T magnetic field generated by the central superconducting solenoid that encloses the subdetector. The magnetic field, which is aligned with the beam line, causes the trajectories of charged particles to curve. This enables the ID to determine both their momentum and electrical charge based on the curvature of these paths.

The ID comprises three distinct subsystems: the pixel tracker, the semiconductor tracker (SCT), and the transition radiation tracker (TRT). It consists of cylindrical barrels and two end-cap disks, as shown in Figure 15. These subdetectors have high granularity and work together to achieve precise momentum and vertex reconstruction. This is essential for detecting long-lived particles.

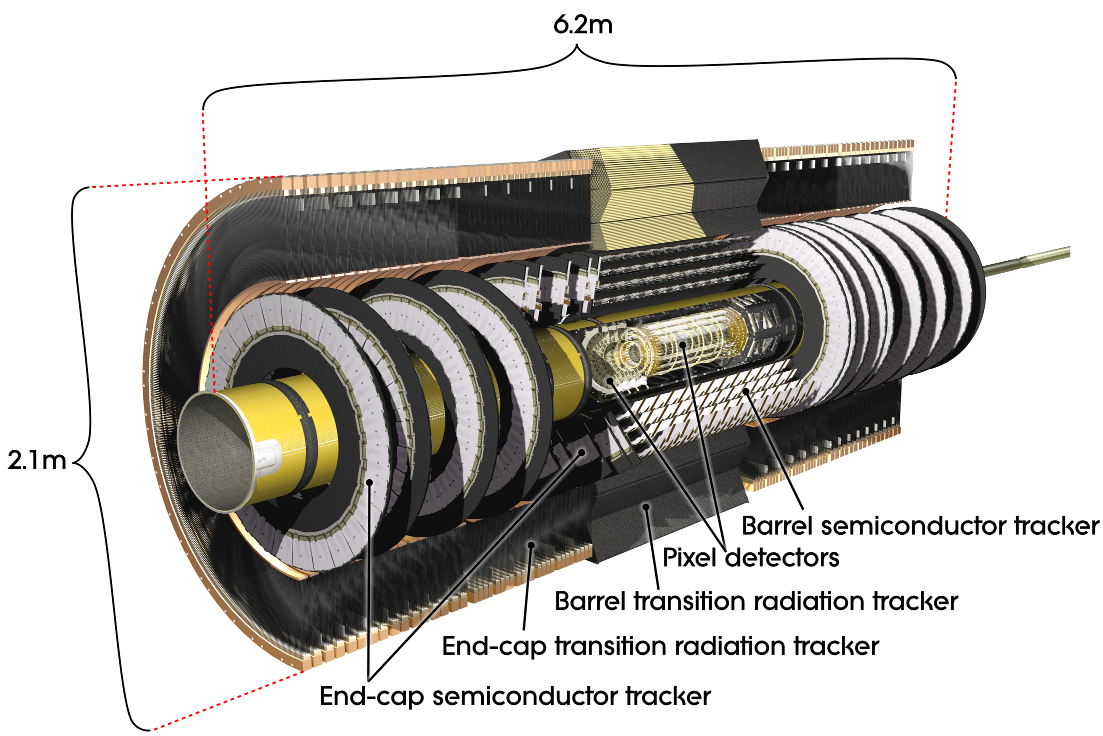

Figure 15: Computer generated image of the inner detector with a section removed for visibility [68].

Pixel Detector

The Pixel detector is the innermost component of the ATLAS tracking system. It has the greatest granularity and a substantial number of readout channels. It is comprised of silicon semiconductor sensors known as pixels and is organized into four cylindrical barrel layers and three end-cap disks. The region it spans is $|\eta| < 2.5$. These pixels are crucial in detecting electrical currents generated by charged particles as they pass through the modules. The signals are then translated into spatial hits that mark specific points along the particle's trajectory. The arrangement of barrels and disks includes over 80 million rectangular pixels, each measuring $10\,\mu\text{m} \times 10\,\mu\text{m}$. This configuration provides spatial resolutions of $10\,\mu\text{m}$ in the transverse plane and $115\,\mu\text{m}$ in the z-direction. Prior to the start of Run II, the insertable B-layer (IBL), which is located at $R = 33\,\text{mm}$, was added to the innermost pixel layer (B-layer) to mitigate resolution degradation caused by radiation damage in Run I and to prepare for the expected increase in pile-up events. The IBL consists of an additional 12 million pixels, each sized at $50\,\mu\text{m} \times 200\,\mu\text{m}$, providing spatial resolutions of $8\,\mu\text{m}$ in the transverse plane and $40\,\mu\text{m}$ in the z-direction. The IBL deployment is crucial for reconstructing secondary vertices in searches for long-lived particles, as it furnishes a fourth hit within the pixel detector.

Semiconductor Tracker

The SCT serves as a tracking subsystem within the ATLAS detector and employs silicon sensors, encircling the pixel detector and spanning the region $|\eta| < 2.5$. The SCT has over 6 million double-sided silicon strips that are $80\,\mu\text{m} \times 12\,\text{cm}$ in size. These strips are distributed across four barrels and nine disks. The strips are inclined at a 40 mrad angle to allow for two-dimensional position determination, resulting in a resolution of $17\,\mu\text{m}$ in the transverse plane and $580\,\mu\text{m}$ in the z-direction. This angular adjustment is necessary to acquire spatial information beyond the transverse/z-ϕ plane constraints that are usually encountered in the barrel/end-cap region when strips are oriented parallel/perpendicular to the beamline. The SCT furnishes eight additional hits conducive to transverse momentum measurements and vertex reconstruction.

Transition Radiation Tracker

The TRT constitutes the outermost component of the ID and encompasses the region $|\eta| < 2.0$. Comprising straw tubes filled with a gas mixture of $Xe/CO_2/O_2$, the TRT surrounds a central anode wire. In some parts of the TRT Xenon has beed replaced with Argon due to gas leak issues druing Run II and in Run III Xenon was completly replaced with Argon. When charged particles pass through the tubes, they ionize the gas, generating a cascade of electrons that drift towards the central wire. This process provides a measurement of the closest approach distance of the particles, with a resolution typically around $130\,\mu\text{m}$. The TRT comprises 52,544 straw tubes oriented parallel to the beam axis in the barrel region, each with a length of 144 cm, covering $|\eta| < 1.0$. Additionally, there are 122,800 straw tubes arranged radially in the end-cap region, with a length of 39 cm, covering $1.0 < |\eta| < 2.0$. On average, the TRT yields 36 additional hits in the transverse/z-ϕ plane in the barrel/end-cap region. This supplementary data aids in resolving tracks from charged particles, particularly those not originating from the pnteraction point, which is crucial for many long-lived particle analyses.
Another notable characteristic of the TRT is its capability to discern different types of charged particles, which sets it apart from the other ID subsystems. Polypropylene fibers are deployed to occupy the gaps between the straw tubes. When charged particles traverse this material, they emit photons through transition radiation, which are then absorbed by the gas mixture, leading to an amplification of the readout signal. This phenomenon is

contingent upon the Lorentz factor and mass of the charged particles. Specifically, it is more pronounced for electrons due to their relatively large Lorentz factor, allowing them to be distinguished from charged hadrons [72].

4.2.3 Calorimeters

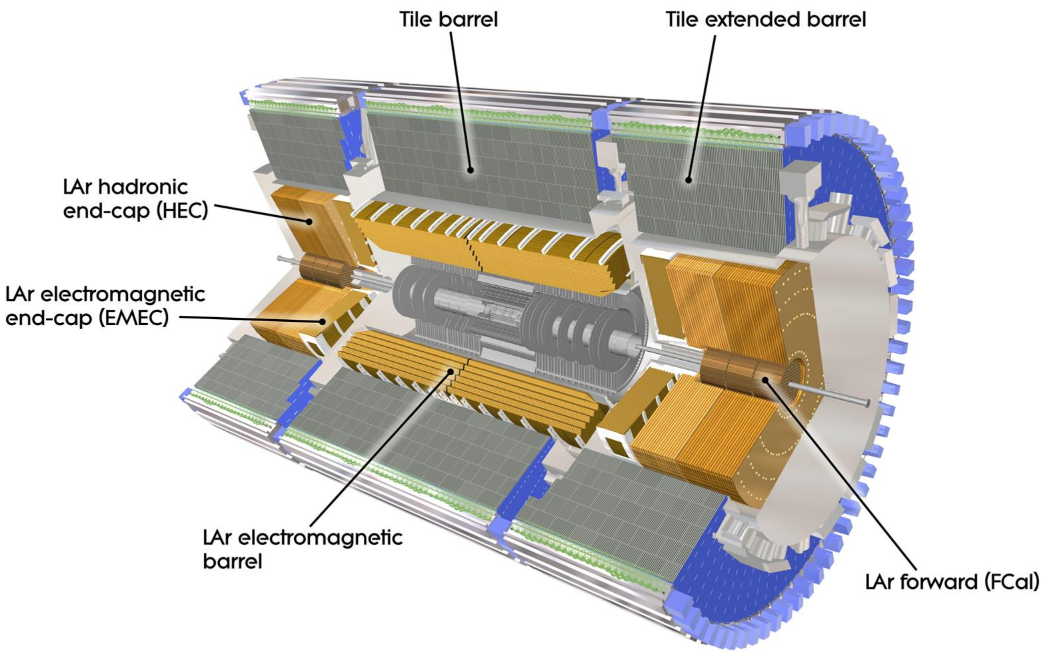

Figure 16: Computer generated image of the calorimeter system with a section removed for visibility [73].

The calorimeters are a crucial part of the ATLAS detector, located between the ID and the MS, and surrounding the central solenoid. They are divided into two main subsystems: the liquid argon (LAr) calorimeters [74] and the tile calorimeters [75], as shown in Figure 16. The calorimeters measure the energy deposited by both charged and neutral particles across the detector's coverage area of $|\eta| < 4.9$. Operating as sampling calorimeters, these devices consist of alternating layers of materials that interact with incoming particles and measure the energy loss from ensuing particle showers. The passive layers within these calorimeters trigger electromagnetic or hadronic showers upon interacting with dense materials. The electromagnetic calorimeter (EMC) measures the energy of induced electromagnetic showers, while the hadronic calorimeter assesses the energy of induced hadronic showers. Usually, only muons and neutrinos are able to pass through the calorimeters, while other particles are stopped, leaving some of their energy in the subsystem. The calorimeters provide precise measurements of energy and position, which are crucial for the trigger system.

Electromagnetic Calorimeter

The EMC is a set of calorimeters positioned outside the central solenoid magnet. Its primary function is to detect photons and electrons while measuring the magnitude, shape, and positioning of their energy deposits. The EMC comprises two main components: the EM barrel (EMB) calorimeter and the EM end-cap calorimeter (EMEC). Both are constructed using LAr technology and cover distinct regions of the detector. The EMB is divided into two identical half-barrels, separated by a 4 mm gap at $z = 0$, to ensure full azimuthal coverage. It consists of sixteen modules, each spanning $\Delta\phi = 22.5°$, and employs "accordion" geometry to eliminate any gaps, as shown in Figure 17. The EMEC is divided into two coaxial wheels, each hosting eight modules, catering to specific $|\eta|$ ranges: $1.375 < |\eta| < 2.5$ and $2.5 < |\eta| < 3.2$. In the transition region between $1.375 < |\eta| < 1.52$, commonly known as the "crack regio", there is a significant amount of inactive material. This material serves the purpose of facilitating ID maintenance, but it may introduce inefficiencies in the reconstruction and identification of objects that pass through this area. The LAr calorimeters use lead as the absorber material due to its heavy nucleus, which facilitates electromagnetic interactions with incident electrons and photons. Liquid argon serves as the active material, measuring the energy deposits of electrons and photons. However, the liquid argon layers, also known as sampling layers, can only measure a fraction of the total energy deposited in each layer, as some energy is lost in the absorber material. Therefore, the initial layer of the barrel LAr calorimeters, located in the region $|\eta| < 1.8$, is known as the presampler. It comprises a slender liquid argon layer intended to counterbalance energy losses caused by electrons and photons in the ID material, without the need for an absorbing layer.

In each absorber layer, electrons and photons interact with the nuclei of the lead material, triggering bremsstrahlung and pair-production electromagnetic showers. These showers are subsequently amplified and measured in the sampling layer. Within the precision region $|\eta| < 2.5$, each LAr module is divided into three layers. The first layer is segmented with fine spatial granularity to offer high-resolution information for photons, which lack identification tracks due to their neutral electrical charge. This layer helps to differentiate between single photons and multi-photon decays. The second layer, which is the longest, captures most of the energy deposited. Finally, the third layer, which is the shortest and

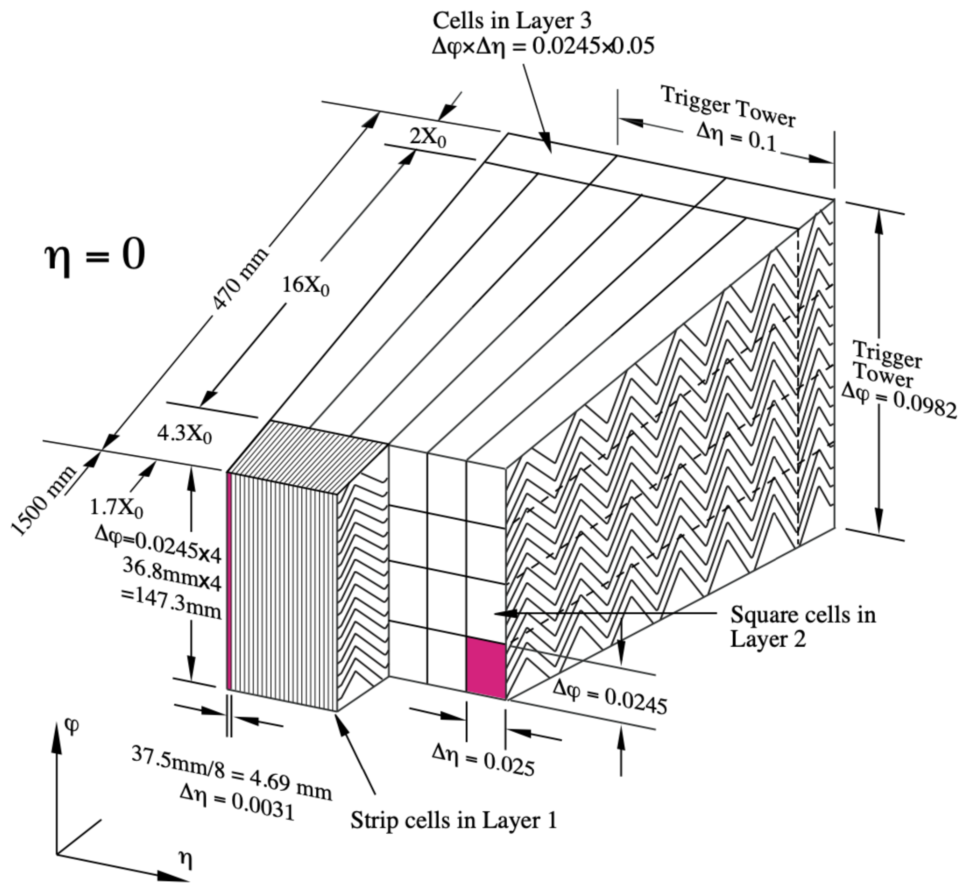

Figure 17: Illustration of a barrel module, showcasing distinct layers with electrodes grouped in the azimuthal direction ϕ. Additionally, the granularity in both pseudorapidity η and azimuthal ϕ directions of the cells within each of the three layers and trigger towers is depicted [68].

coarsest, collects the high-energy electromagnetic shower tails and estimates the energy leakage beyond the electromagnetic calorimeters. The thickness of the LAr modules in the precision area ranges from 22 to 33 times the radiation length X_0, measured in units of $\mathrm{g\,cm^{-2}}$, depending on the η value. In the end-cap region, the module thickness ranges from 24 X_0 to 38 X_0. This coverage of radiation lengths effectively achieves the objective of the EMC to stop all electrons and photons as they pass through the material [74].

Hadronic Calorimeter

Due to their larger masses, hadrons have a lower probability of interacting with the material in the EMC LAr modules, allowing them to pass through to the hadronic calorimeter. The hadronic calorimeter is designed to stop the hadrons that pass through the EMC while measuring their energy deposits and any missing transverse energy E_T^{miss}. It consists of the tile calorimeter (TileCal), the hadronic end-cap calorimeter (HEC), and the forward calorimeter (FCal).

The TileCal spans $|\eta| < 1.7$ and is divided into two sections: the central barrel region ($|\eta| < 1.0$) and the extended barrel region ($0.8 < |\eta| < 1.7$). Each segment comprises 64 wedge-shaped modules arranged in three radial layers. The modules employ alternating layers of steel as the absorber material and plastic scintillators as the active material. Hadronic showers, similar to electromagnetic showers, arise from hadrons interacting with the dense absorber material. These particle showers, mostly consisting of pions, interact with the plastic tiles and produce scintillation light. The light is then transmitted to photomultiplier tubes through wavelength-shifting fibers for cluster hit readout.

The HEC and FCal cover the pseudorapidity ranges of $1.5 < |\eta| < 3.2$ and $3.1 < |\eta| < 4.9$, respectively. Both are composed of LAr calorimeters. The HEC is made up of four layers, with two wheels per end-cap. Each layer consists of 32 wedge-shaped LAr modules that use copper instead of lead as the absorber material. The FCal is positioned between the beam pipe and the HEC wheels and is arranged in three layers along the beam line. Each layer uses liquid argon as the active material. However, the absorber materials used in the detector vary depending on the types of particles being targeted. The first layer utilizes copper as the absorber material, while the subsequent two layers use tungsten to intercept electromagnetically and strongly interacting particles, respectively. In the barrel and forward regions, the thickness of the hadronic calorimeter is 9.7λ and 10λ, respectively, measured in terms of nuclear interaction length λ, effectively stopping strongly interacting particles from passing through the material.

4.2.4 Muon Spectrometer

The MS is the furthest-reaching detector in the ATLAS detector. Its main function is to identify muons and measure their transverse momenta. Muons are able to traverse the calorimeter systems with minimal energy loss due to their relatively heavy mass and electromagnetically penetrative nature. Therefore, the MS is placed outside other subdetectors. The MS is divided into tracking and triggering components. The tracking components consist of Monitored Drift Tube (MDT) chambers or Cathode Strip Chambers (CSCs), while the triggering components include Resistive Plate Chambers (RPCs) or Thin Gap Chambers (TGCs). These subsystems provide almost complete coverage of the ϕ angle, with a small gap at $z = 0$ for accessibility and maintenance purposes. Figure 18 shows the integrated MS subsystems. Similar to the ID, the large toroidal magnets that encircle the

MS bend the muon trajectories, allowing for the determination of muon electric charges and transverse momenta.
The tracking systems together cover the range $|\eta| < 2.7$, while the trigger systems cover the more restricted region $|\eta| < 2.4$. The magnetic field is produced by the barrel toroid within $|\eta| < 1.4$ and the end-cap toroids within $1.6 < |\eta| < 2.7$. The transition zone, $1.4 < |\eta| < 1.6$, experiences a combined magnetic field from both toroidal systems. The tracking systems capture muon pseudorapidity and transverse momentum data, while the triggering systems provide rough momentum assessments, orthogonal spatial measurements in in the azimuthal angle, and identification of bunch crossings. The efficacy of the MS is crucial because the resulting muons often require tracking and trigger data from the MS for reconstruction, due to the ID's limitations in independently reconstructing objects that originate far from the IP.

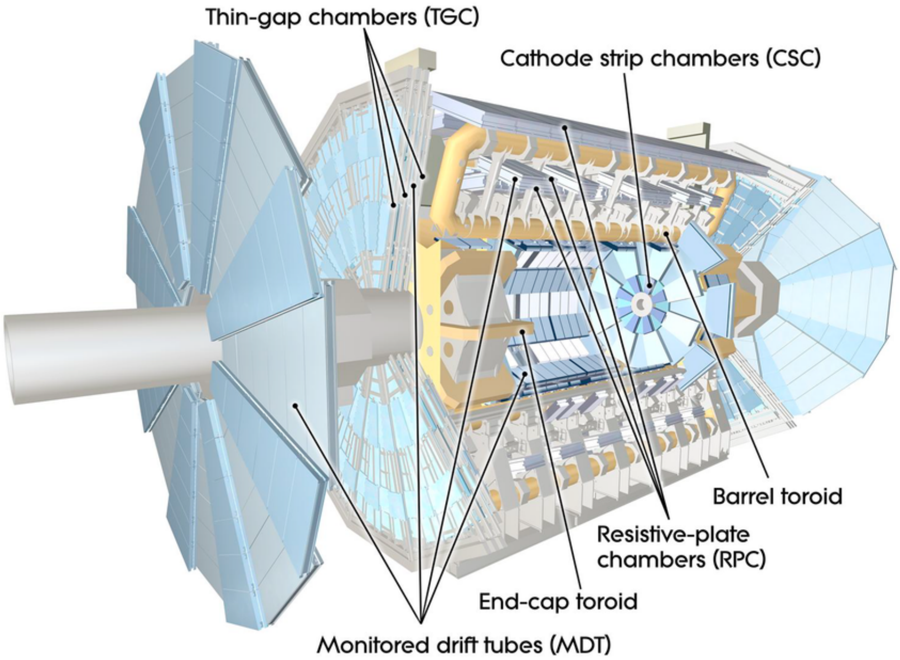

Figure 18: Computer generated image of the muon spectrometer with a section removed for visibility [68].

Monitored Drift Tube Chambers

The main tracking component of the MS relies on MDT chambers, providing accurate momentum measurements within the $|\eta| < 2.7$ region, except for the innermost end-cap layer, which has limited coverage up to $|\eta| < 2.0$. These chambers are organized into three cylindrical barrel layers, covering $|\eta| < 1.1$, and three parallel end-cap wheels, covering the region $1.1 < |\eta| < 2.7$. The chambers consist of drift tubes filled with a 93%/7% Ar/CO_2 gas mixture. Each tube has a diameter of 3 cm and uses a tungsten-rhenium anode central wire. The tubes measure the closest approach distance of incoming muons with an accuracy of 80 µm, following the principles used in TRTs (Transition Radiation Trackers). However, in MDT chambers, the drift tubes are arranged perpendicular to the beam line in the barrel layers and tangentially in the end-cap wheels. This arrangement provides curvature measurements of muon trajectories in the η-z plane with a spatial resolution of 35 µm. Each MDT chamber consists of six to eight drift tube layers and is partitioned into two multilayers of three to four drift tube layers. These multilayers are used to independently construct partial muon tracks, known as tracklets, during muon reconstruction.

Cathode Strip Chambers

The MS tracking subsystem's second element comprises the CSCs, which expand the MDT chambers' coverage to the range of $2.0 < |\eta| < 2.7$ within the innermost end-cap wheel. In this segment, the muon rate exceeds the MDT chambers' maximum counting rates, capped at $150\,\mathrm{Hz\,cm^{-2}}$. To address this, the CSCs, which can operate with much higher hit rates of up to $1\,\mathrm{kHz\,cm^{-2}}$, complement the tracking data provided by the MDT chambers. Each CSC is a multiwire proportional chamber that contains anode wires and cathode strip planes filled with an 80%/20% Ar/CO_2 gas mixture. The chamber features radially aligned multiwires alongside cathode strips oriented alternately in parallel and perpendicular directions to the wires. This configuration facilitates precise spatial measurements in both η and ϕ, achieving a resolution of $60\,\mu\mathrm{m} \times 5\,\mu\mathrm{m}$. Within each end-cap, there are eight small and eight large chambers, each equipped with four CSC planes. As a result, the CSCs provide multiple independent two-dimensional spatial measurements in the region not covered by the MDT chambers.

Resistive Plate Chambers

The RPCs make up the barrel segment in the range of $|\eta| < 1.05$ of the MS's trigger subsystem. They are similar to the MDT chambers in the barrel area and are arranged in three concentric cylindrical layers. Each chamber consists of two parallel resistive plates separated by a 2 mm gap and filled with a norflurane-based ($C_2H_2F_2$) gas mixture. Readout strips are located on both sides of each chamber. Muons passing through the RPCs ionize the gas, and the external readout strips detect any avalanches in the gaps, providing spatial measurements in z and ϕ. The RPCs are arranged in sixteen paired units around ϕ within each layer, positioned either just inside or outside an MDT barrel layer. This arrangement offers six additional measurements across all three layers, resulting in a spatial resolution of 10 mm 10 mm and a time resolution of 1.5 ns. The two innermost layers act as triggers for low-p_T muons, requiring three out of four hit coincidences, while the third layer is designated for high-p_T triggers, requiring one out of two coincidences [76].

Thin Gap Chambers

The end-cap component of the triggering subsystem spans the region $1.05 < |\eta| < 2.4$ and is composed of TGCs. The TGCs provide ϕ spatial measurements up to $|\eta| < 2.7$, similar to the CSCs. The TGCs are multiwire proportional chambers filled with a 55%/45% CO_2/n-pentane (n-C_5H_{12}) gas mixture, enabling radial and bending coordinate measurements, as well as ϕ measurements with resolutions of 7 mmand 2 mm, respectively. The TGCs are configured in four layers of twelve sectors each in the end-cap. They use coincident hits for muon triggers, similar to the RPCs, which results in a time resolution of 4 ns.

4.2.5 Magnet System

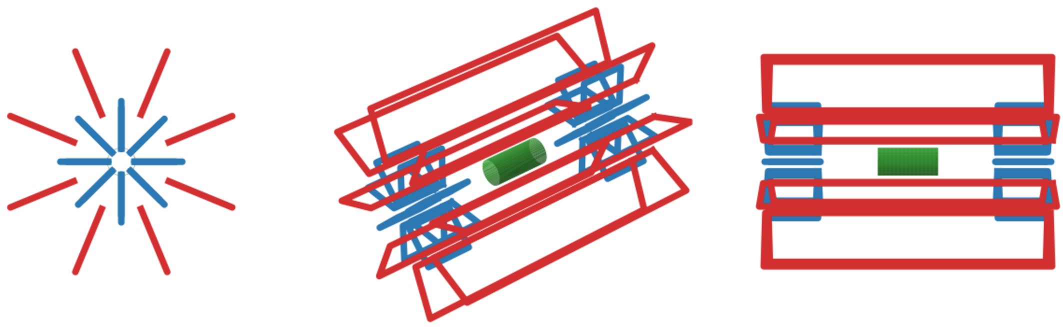

Figure 19: Illustration of the geometry of the magnet system field coils showing the endcap (left), perspective (middle), and the side view (right). The central solenoid (green) is inside the eight windings of the barrel toroid (red). End-cap toroids (blue) appear on either side [77].

The ATLAS Magnet System comprises three superconducting magnet systems: the central solenoid (CS), the barrel toroid (BT), and the two end-cap toroids (ECT). The configuration of these magnets is illustrated in Figure 19. Their primary function is to generate a robust magnetic field necessary for accurately measuring the momenta of charged particles. Each coil constituting the magnets experiences gravitational and magnetic forces. Therefore, they are housed within mechanical structures containing cooling circuits and cryostats to maintain an operational temperature of approximately 4.5 K. The coils are wound with superconducting niobium-titanium embedded in a copper-aluminum matrix. When fully energized, the combined magnetic fields of the four magnets store an energy of 1.3 GJ.

Central Solenoid Magnet

The central solenoid is located between the ID and the calorimeters, producing a 2 tesla magnetic field that is crucial for bending the paths of charged particles within the ID's transverse plane. This bending effect, as discussed in Section 4.2.2, is essential for accurately determining the electrical charges and transverse momenta of the charged particles. The solenoid must minimize its radiative thickness, especially since it is located before the calorimeter systems (see Section 4.2.3). It measures 2.4 meters in diameter and 5.3 meters in length [78].

Toroid Magnets

The BT magnet is a prominent feature of the ATLAS experiment, being the largest magnet within it. It spans 26 meters along the beamline and has a diameter of 20 meters. The magnet is comprised of eight air-cooled coils that envelop sections of the muon spectrometer. Each coil comprises 120 turns wired in series, generating a magnetic field of up to 3.9 T at its peak intensity. Additionally, two air-cooled ECT provide a magnetic field for the MS wheels. The toroids are 5 meters long and have an outer diameter of 10.7 meters. They have an inner diameter of 1.65 meters to allow for beam passage. Each ECT is similar to the BT and consists of eight coils with 116 turns, which are wired in series. The ECTs generate fields that peak at 4.1 T and operate with a current of 20 kA. To maintain superconducting temperatures, tubes carrying 4.5 K helium are attached to the casings of the windings.

4.2.6 Trigger System

The LHC initiates collisions between proton bunches within the ATLAS detector every 24.96 ns, resulting in a crossing frequency of 40 MHz. However, capturing data from these collisions would result in an impractical volume of data, exceeding 60 TB/s, due to the approximately 100 million readout channels combined. Therefore, it is crucial to establish a system for discerning which data to preserve and archive. This need becomes more important when considering the pileup rates. A significant portion of the data comes from low-energy interactions that have minimal scientific interest. To tackle this issue, the ATLAS experiment uses a hardware and software combination to identify potentially significant physics events, reducing the data rate to 1 kHz. The ATLAS trigger system uses a hardware-based level 1 (L1) trigger and a software-based high level trigger (HLT) to select events. The Data Acquisition (DAQ) system processes information from each detector component to reconstruct the chosen events, which are then stored in Data Storage (SFO).

Level 1 Trigger

The L1 trigger, which includes the L1 calorimeter and L1 muon trigger systems, is crucial in reducing the data rate to 100 kHz. It identifies events with high-p_T leptons, photons, jets, and significant total or missing transverse energy $E_{\mathrm{T}}^{\mathrm{miss}}$ within 2.5 µs of the bunch-crossing, based on predefined criteria outlined in a trigger menu. The trigger menu is a compilation of energy thresholds established by various analyses to identify events of interest. Additionally, the L1 trigger identifies regions-of-interest (RoIs) in η and ϕ, highlighting areas where potentially significant features are detected. These RoIs, along with the trigger-selected events, are subsequently transmitted to the HLT.

High Level Trigger

The HLT is a software-driven process that filters and reconstructs physical entities from events selected by the L1 trigger. It uses the data provided by the L1-identified RoIs and reconstructed ID tracks to tentatively identify high-p_T physics objects based on corresponding energy signatures. This system reduces the data rate to 1 kHz, which is a significant improvement compared to the previous practice of retaining all events. This effectively saves only about 1 in every 40,000 collisions. The selected events are then sent to CERN's Tier-0 computing facility for storage and reconstruction [79].

5 Monte Carlo Samples

This work is based entirely on Monte Carlo generated data. Since the properties of simulated particles are fully known at each point of their development, these variables are often referred to as "truth". One can choose at which point of the simulation to "measure" a truth value (e.g. a particle 4-momentum). It should be noted that in the context of the ATLAS experiment the term "simulation" usually refers to the simulation of the ATLAS detector response, which is not done in this work.
First, the different phases of event generation are presented and explained in Section 5.1. The samples used in this analysis are then presented and explained in Section 5.2.

5.1 Event Generation

The simulation of samples begins by generating individual events according to a prescribed theoretical framework. To generate events, a model, such as a function that outlines a differential cross-section, can be used to iteratively and randomly extract samples from the model in accordance with its probability distribution function. As the sample size increases towards infinity, the distribution resulting from the accumulation of all events (e.g. by populating a specific variable in a histogram, which is then normalized - although in practice, this involves a multidimensional phase space) approaches the theoretical model. These methods are commonly known as Monte Carlo methods [80] and the set of generated events is usually referred to as Monte Carlo samples or simply MC.

Fundamentally, MC samples are produced to emulate physics phenomena. In an ideal scenario where the detector can precisely measure each particle, there is a thorough comprehension of the underlying theoretical framework, and the detector response is accurately simulated, it is conceivable to generate an MC sample that accurately replicates the observed data (with the exception of statistical variations). Due to the numerous processes that can result from collisions at the LHC, as shown in Figure 20 for a general overview, and which usually occur in every event, a single MC sample cannot comprehensively depict every sub-product of the primary interaction. Instead, MC samples are tailored to specific processes, adhering to a set of theoretical constraints, including PDF, QCD and EW perturbative orders, flavor considerations, parton showering and hadronization modeling.
The simulation of an event is not completed in a single operation. Instead, particle interactions are broken down into smaller stages, each addressing distinct phenomena and facilitating targeted adjustments. This modular approach enables the development of specialized computational frameworks tailored to simulate particular processes, creating a

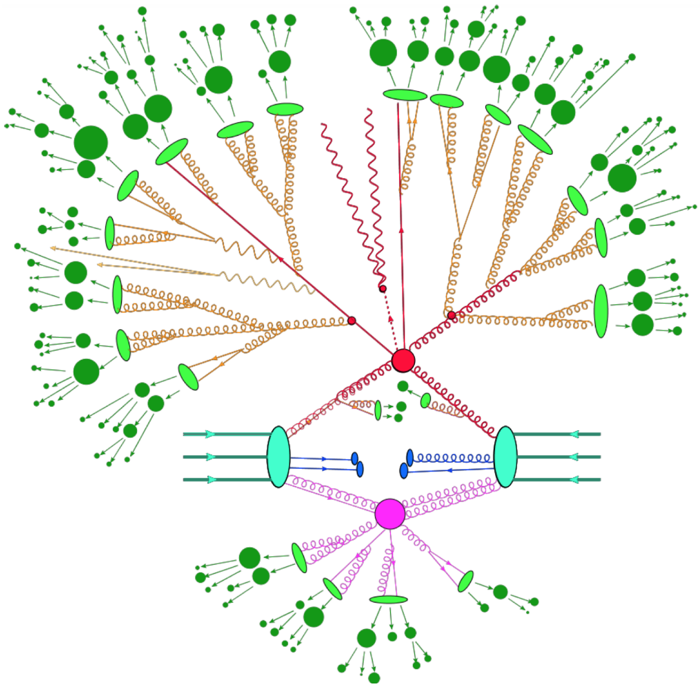

Figure 20: Illustration of a particle collision within the `Sherpa` framework [81]. The incoming beams are shown in cyan on both sides. During the collision, certain partons are involved in hard processes, represented by red blobs, while others participate in underlying processes, depicted by a purple blob. Additionally, there are beam remnants indicated in blue, which do not undergo any interaction. The purple and ochre curly lines represent parton showers. The diagram shows the process of hadronization of partons in light green blobs and the decay of unstable hadrons in dark green blobs and lines. During the collision event, charged particles may emit photons at any time, leading to electromagnetic showers through processes like electromagnetic pair production and annihilation.

flexible platform where the most suitable tool for a given analysis can be integrated or adjusted with relative ease. Figure 20 shows the progression of a particle simulation and its subdivision into intermediate physical states. The following sections provide a brief overview of each stage.

5.1.1 Parton Distribution Functions

The simulation begins by characterizing the partonic composition within each proton using its PDFs. These functions are established in advance through dedicated investigations conducted by research groups worldwide using various methodologies and datasets. PDFs provide a precise description of the partonic composition, at a specific QCD perturbative order (see Section 2.4.2). The PDFs are expressed as a function of the momentum fraction carried by each parton, designated as x, which ranges from 0 to 1. Additionally, the factorization scale and the energy scale of the interaction are taken into account (see Section 3.1).

5.1.2 Hard Scattering

When considering two partons originating from separate protons, each characterized by their respective momentum fractions, the interaction between them, known as hard scattering, where "hard" denotes substantial momentum transfer, can be predicted by theoretical calculations. Partonic cross-sections $\sigma_{a,b\to X}$ are established via series computations using fixed-order perturbation theory to evaluate these processes. The computations are typically expanded around the strong coupling factor α_s:

$$\sigma_{a,b\to X} = \alpha_s^n(\sigma_0 + \alpha_s\sigma_1 + \alpha_s^2\sigma_2 + \alpha_s^3\sigma_3 + \mathcal{O}(\alpha_s^4)), \tag{5.1}$$

where σ_0 is the LO, $\alpha_s\sigma_1$ is the NLO and so forth.

By selecting a particular order, the generated sample will include only a finite number

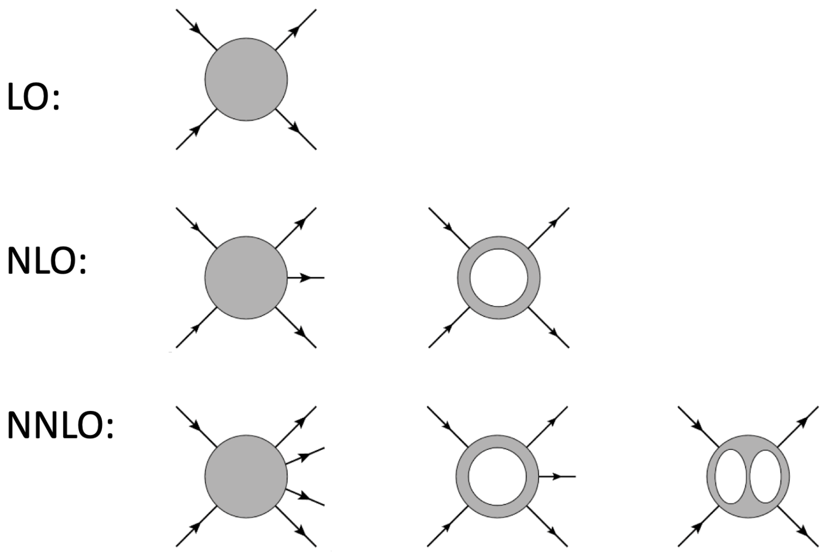

Figure 21: Schematic representation of contributions at various perturbative levels with fixed orders [82].

of contributions, disregarding higher-order loop effects. Figure 21 illustrates the contributions at LO, NLO, and NNLO as shown in Equation 5.1. Examining these diagrams, it's important to consider that at next-to-leading order in perturbative quantum field theory, the inclusion of virtual contributions from higher-order loop diagrams (such as those at

next-to-next-to-leading order) can sometimes result in computational divergences. This can be mitigated by incorporating tree level higher-order NLO diagrams through appropriately conducted phase space integration. This compensation for divergence alone may introduce non-physical features, such as spikes. These spikes may arise due to the presence of large logarithms, which can be problematic for computational accuracy. To mitigate this issue, resummation algorithms are employed to correct for large logarithms and ensure more reliable results. Therefore, higher-order predictions require some form of parton showering through specialized generators (see Section 5.1.3).
By combining the PDFs of both protons with the hard scattering cross sections for the desired process and summing over all possible quark combinations, a prediction can be derived at a fixed order.

5.1.3 Parton Shower

After the initial hard scattering process, subsequent parton showering occurs to simulate the radiation of partons from initial- or final-state particles and gluon splitting on the cross sections obtained from fixed order (FO) predictions based on the process' matrix element. This showering process is modeled using MC parton showering algorithms, which simulate the emission of partons, including soft and collinear emissions. While parton showers inherently resum logarithmic terms associated with these emissions, resummation methods specifically focus on addressing large logarithmic terms in perturbatice calcuations but they are not directly involved in the parton showering process.

Considering the scenario of $p_T^{W^+}$, which represents the next-to-leading order (NLO) transverse momentum of the W^+ boson, as shown in Figure 22. In FO calculations, the NLO prediction exhibits a divergence as $p_T^{W^+}$ approaches zero (i.e. $p_T^{W^+} \ll m_W$), which is attributed to the presence of soft and collinear emissions, resulting in ultraviolet divergence. After the stage where parton showering occurs, resummation corrections address this issue by incorporating a Next-to-next-to-leading logarithm (NNLL) correction (but not via parton showers), resulting in finite cross-section terms (illustrated by the red curve in Figure 22). Several frameworks are utilized for MC-driven parton showering, each selected based on specific investigation requirements and characteristics. Prominent among these are `Herwig` [84], `Sherpa` [81], and `Pythia` [85]. While `Sherpa` is not solely a framework for parton showering, it implements its own parton showering algorithms along with other functionalities. Both `Sherpa` and `Pythia` are employed in this work for their respective capabilities.

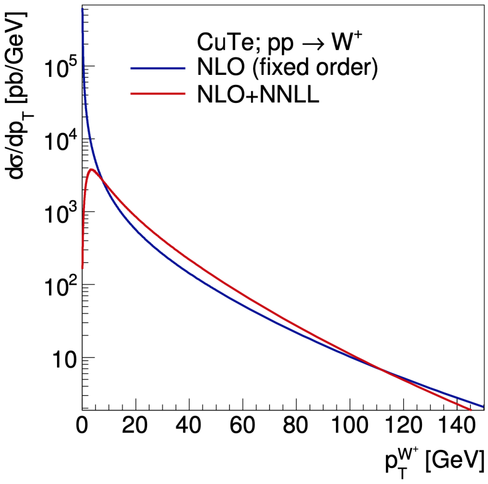

Figure 22: Theoretical predictions for the $p_T^{W^+}$ differential cross section at NLO are shown [83]. Showing the FO prediction in blue alongside the effect of NNLL resummation corrections in red.

5.1.4 Non-perturbative Models

The computation of secondary particle generation and development outside the primary process is challenging due to the numerous variables involved. Non-perturbative models are typically used to calculate these predictions, often calibrated using e^+e^- collision data, which are independent of PDFs. `Pythia` is a commonly used tool for this purpose. A thorough comprehension of these phenomena is essential for analyzing the entire particle spectrum resulting from an LHC collision and accurately identifying signals across the ATLAS detector.

5.2 Data set description

General-purpose event generators play a crucial role in the ATLAS experiment for generating a large number of events. They can be connected to matrix element generators, enabling the generation of parton-level events that can then undergo hadronization. Alongside these, more specialized generators like `MadGraph5_aMCatNLO` [19] are also widely utilized. In the simulation process, `MadGraph5_aMCatNLO`, which is the NLO extension of `MadGraph`, is responsible for calculating the hard scattering process. Subsequently, the results are passed to `Pythia` for the subsequent steps of showering and hadronization.
In this work, two samples from two different generators were used and compared in Section 6.6, where the different simulations regarding gluon splitting are discussed in particular. The samples of the two different generators `Sherpa` and `MadGraph` will now be presented

and explained in Section 5.2.1 and Section 5.2.2 respectively.
The world average data measurement for the generation of a D^+ from a charm quark stands at 24%. `Sherpa` yields a value of 23.7%, while `Pythia8` [86] (see Section 5.2.2) yields 29.3% [87]. Given that only the distribution shapes are examined in this analysis, no scaling factor was applied.

5.2.1 Sherpa

An overview of the two `Sherpa 2.2.11` [18] samples used for this analysis is given in Table 5.
The two Monte Carlo samples simulate proton-proton collisions with a center-of-mass energy of 13 TeV. They specifically focus on the W $(e\ nu)$ + jets process. These simulations utilize NLO-accurate matrix elements for up to two partons and LO-accurate matrix elements for between three and five partons, all computed within the framework of the five-flavor scheme, which includes up, down, strange, charm, and bottom quarks. The computations are performed using the Comix [88] and `OpenLoops` [89–91] libraries.
Within the simulations, bottom and charm quarks are considered massless at the matrix-element level but are treated as massive in the parton shower. The PDF set employed is the Hessian `NNPDF3.0_NNLO` [92]. The default `Sherpa` parton shower, which is based on Catani-Seymour dipole factorization and the cluster hadronization model [93, 94], is utilized.
These MC samples are generated using a dedicated set of tuned parameters developed by the `Sherpa` authors and are based on the `NNPDF3.0_NNLO` set. The NLO matrix elements for each jet multiplicity are matched to the parton shower using a color-exact variant of the `MCatNLO` algorithm [95]. Subsequently, different jet multiplicities are merged into an inclusive sample using an improved CKKW matching procedure [96], which extends to NLO accuracy using the `MEPSatNLO` prescription [97]. The merging scale employed is $Q_{\text{cut}} = 20\,\text{GeV}$.

In both samples a weighting function was applied during event generation. This weighting function ensures that the distribution of events as a function of the transverse hadronic energy and the transverse momentum of the vector boson does not directly reflect the physics cross section. Instead, the weighting function adjusts the number of events at different values for the transverse hadronic energy and the transverse momentum of the vector boson, with more events occuring at higher values of these quantities. However, the weights assigend to each event compensate for this imbalance, ensuring that the overall cross section is correctly reproduced when using the weighted events.

Additionally, both samples apply filters to select special characteristics of the final state. In one sample a filter is applied to select events containing bottom hadrons (BFilter), while in the other events containing charm hadrons are allowed (CFilter) while those containing bottom hadrons are vetoed. These filters impact the composition of the final state particles and the characteristics of the simulated events. However, this is of no further relevance in the course of this analysis as the two samples are merged together.
The plots shown in the Analysis section, in Section 6.5 were all made with these two samples.

5.2.2 MadGraph

Table 6 presents an outline of the `MadGraph` samples utilized in this analysis.
Even with extensive V + jets samples, obtaining statistically significant measurements of the $W + D^{(*)}$ fiducial efficiency remains challenging due to the limited number of $W + D^{(*)}$ events. To address this, filtered, forced decay samples are employed to bolster statistical precision. These filters necessitate the presence of a single lepton with $p_T^{\ell} > 15\,\mathrm{GeV}$ and $|\eta(\ell)| < 2.5$, alongside either a D^* or a D^+ meson with $p_T^{D^*/D^+} > 7\,\mathrm{GeV}$ and $|\eta(D^*/D^+)| < 2.3$. Employing `EvtGen`, all D^0 mesons are directed to decay via the mode $D^0 \to K^-\pi^+$ and D^+ mesons to decay through $D^+ \to K^-\pi^+\pi^+$. Charge conjugate meson decays are also enforced.
The `MadGraph5_aMCatNLO 2.6.5` program is employed to produce weak bosons with up to three additional partons in the final state at NLO precision. Renormalization and factorization scales are set to one half of the transverse mass of all final state partons. Subsequent showering and hadronization are executed using `Pythia 8.240` with the A14 tune. Diverse jet multiplicities are merged employing the FxFx NLO matrix-element and parton shower merging prescription [98]. QED radiation is incorporated via `Pythia8`.
The `MadGraph5_aMCatNLO` calculation adopts a five-flavour number scheme with massless bottom and charm quarks at the matrix-element level, while employing massive quarks in the `Pythia8` shower. At the event-generation stage, jet transverse momentum is mandated to be no less than 10 GeV, with no restrictions on the absolute value of jet pseudorapidity. The PDF set utilized for event generation is `NNPDF3.1nnlo_luxqed`. The merging scale is defined as $Q_{\mathrm{cut}} = 20\,\mathrm{GeV}$.

Table 5: List of `Sherpa_2.2.11` W + jets MC samples used in this analysis. "DSID" stands for Dataset Identification which is a unique identifier assigned to each simulated dataset to distinguish it from others. The k-factor is a scaling factor applied to simulated events to match experimental measurements or theoretical predictions.

Process	Summary Name	DSID	$\sigma\cdot$ BR [pb]	k-factor	ϵ_{filter}	N events
$W\ (e\nu)$ + jets	Sh_2211_Wenu_maxHTpTV2_BFilter	700338	20080	1.000	9.373×10^{-3}	285,190,000
	Sh_2211_Wenu_maxHTpTV2_CFilterBVeto	700339	20080	1.000	1.470×10^{-1}	607,280,000

Table 6: List of `MadGraph` $W + D^{(*)}$ Forced Decay MC samples used in this analysis.

Process	Summary Name	DSID	$\sigma\cdot$ BR [pb]	k-factor	ϵ_{filter}	N events
$W\ (e\nu) + D^{(*)}$	MGpy8EG_Wenu_FxFx_3jets_HT2bias_ForceDplusD0	507716	2207	1.000	2.247×10^{-2}	59,998,00
$W\ (\mu\nu) + D^{(*)}$	MGpy8EG_Wmunu_FxFx_3jets_HT2bias_ForceDplusD0	507717	2219	1.000	2.256×10^{-2}	59,980,000

6 Analysis

In this chapter, kinematic distributions associated with the $W+D^{(*)}$ process are presented. The amount of gluon splitting is estimated as a function of the transverse momentum of the $D^{(*)}$ meson $p_T^{D^{(*)}}$, the absolute pseudorapidity of the $D^{(*)}$ meson $|\eta(D^{(*)})|$, and the azimuthal angle between the charged lepton and the $D^{(*)}$ meson $\Delta\phi(\ell, D^{(*)})$.

Section 6.1 explains the fiducial selection for the analysis. Section 6.2 gives an overview of the observables examined. Section 6.3 explains and motivates the OS-SS subtraction. The choice of binning is presented in Section 6.4. The analysis, i.e. the kinematic distribution, is presented in Section 6.5 for all three observables separately. Finally, in Section 6.6 the disagreement between the two different generators used in this analysis regarding the gluon splitting is illustrated.

6.1 Object Selection

The fiducial region is determined by the general characteristics of the detector (see Section 4.2). The cuts made here follow these characteristics and thereby define the fiducial region. Events are singled out by requiring the presence of exactly one lepton with a transverse momentum p_T^ℓ (for the definition see Section 4.2.1) greater than 30 GeV and an absolute pseudorapidity $|\eta(\ell)|$ (the definition is given in Equation 4.3) less than 2.5. This lepton must come from the decay of a W boson, with τ decays excluded from the fiducial range.

Table 7: Fiducial selection for $W + D^{(*)}$.

Selection	$W^\pm + D^{(*)}$
p_T^ℓ	$> 30\,\text{GeV}$
$\lvert\eta(\ell)\rvert$	< 2.5
$N(D^{(*)})$	≥ 1
$p_T^{D^{(*)}}$	$> 8\,\text{GeV}$
$\lvert\eta(D^{(*)})\rvert$	< 2.2

Incoming particles before the collision (initial state radiation) and outgoing particles after the collision (final state radiation) (see Section 5.1.3) can emit photons. Dressed leptons are reconstructed leptons whose momenta have been adjusted to include the effects of the electromagnetic interactions. The momenta of the leptons are computed using dressed containers, which merge photons from the final state radiation with the lepton's four vector.

$D^{(*)}$ mesons are required to have a transverse momentum $p_T^{D^{(*)}}$ to be greater than 8 GeV and an absolute pseudorapidity $|\eta(D^{(*)})|$ to be less than 2.2.
No cuts on the neutrino momentum or the transverse mass are imposed.

An overview of the fiducial event selection is given in Table 7.

6.2 Observables

In this work, variables are sought that make it possible to distinguish between $W + D^{(*)}$ events where there are no additional charm quarks in the hard scattering and W + gluon splitting events that contain both a charm and an anti-charm hadron. For this purpose, different kinematic distributions are considered.

Table 8: An overview of the observables, the different channels and where to find the corresponding plots.

Observable	Channel	Figure
$p_T^{D^{(*)}}$	$W^+ + D^-$	23
	$W^+ + D^{*-}$	24
	$W^- + D^+$	25
	$W^- + D^{*+}$	26
$\lvert\eta(D^{(*)})\rvert$	$W^+ + D^-$	27
	$W^+ + D^{*-}$	28
	$W^- + D^+$	29
	$W^- + D^{*+}$	30
$\Delta\phi(\ell, D^{(*)})$	$W^+ + D^-$	31
	$W^+ + D^{*-}$	32
	$W^- + D^+$	33
	$W^- + D^{*+}$	34

Three variables are examined in more detail below. Namely the transverse momentum of the D meson $p_T^{D^{(*)}} = p^{D^{(*)}} \sin(\theta)$ as defined in Section 4.2.1, the absolute value of the pseudrapidity of the $D^{(*)}$ meson $|\eta(D^{(*)})|$ as defined in Equation 4.3 and the azimuthal angle $\Delta\phi(\ell, D^{(*)})$ between the $D^{(*)}$ meson and the lepton.

Table 8 gives an overview of the different channels, variables and where the corresponding plots can be found in Section 6.5.

6.3 OS-SS Substraction

The calculation of the charge asymmetry of the opposite-sign same-sign provides valuable insights into the distinction between a charmed meson produced by gluon splitting and those produced by other mechanisms (see Section 3.2).

In processes involving gluon splitting, gluons can divide into quark-antiquark pairs. This mechanism plays a role in the generation of charmed mesons in proton-proton collisions. Gluon splitting can yield quark-antiquark pairs with varying flavors and charges, resulting in the production of both positively and negatively charged charmed hadrons.
The OS-SS asymmetry observed in $W + D^{(*)}$ events allows for the investigation of the relative contributions of processes involving gluon splitting compared to other production mechanisms. This asymmetry arises because gluon-splitting processes tend to produce pairs of oppositely charged $W + D^{(*)}$ as frequently as pairs with the same charge. Analyzing the OS-SS asymmetry enables to glean insights into the dynamics of gluon splitting and its significance in hadron production processes, as the $W + D^{(*)}$ production originating not from gluon splitting always have opposite-sign electric charges.

In this analysis, the selected events are categorized based on the charge combination of the charged particles originating from the $W + D^{(*)}$ decay. Events where the lepton and the charged charm hadron have opposite charge (same charge) are classified as OS (SS).

6.4 Binning

For this analysis, different histograms with different binning schemes are used to capture the distributions of the relevant observables as outlined in Section 6.2. These histograms are filled with events that meet certain criteria, allowing to study the properties of gluon splitting in the $W + D^{(*)}$ production.

Both uniform and non-uniform binning is used for the two different variables. Uniform binning is employed for the absolute pseudorapidity $|\eta(D^{(*)})|$ and the azimuthal angle $\Delta\phi(\ell, D^{(*)})$, while non-uniform binning is utilized for the transverse momentum $p_T^{D^{(*)}}$.
The binning for the differential $p_T(D^{(*)})$ distributions in this thesis is based on Reference [1]'s argument. Table 9 provides the bin edges of the five differential $p_T(D^{(*)})$ bins, with the last bin starting at 80 GeV and having no upper limit. The bin size and edges were selected to achieve an expected statistical uncertainty of approximately 1% – 2% in the first four bins.

To ensure percent-level precision, five bins are chosen in $|\eta(D^{(*)})|$, similar to the $p_T^{D^{(*)}}$ bins.

Table 9: The differential $p_T^{D^{(*)}}$, $|\eta(D)|$ and $\Delta\phi$ bins used in this analysis. The last $p_T^{D^{(*)}}$ bin has no upper limit. Each of the five bins is actually divided into five equally sized bins, resulting in a total of 25 bins.

Observable	1	2	3	4	5
$p_T^{D^{(*)}}$ bin edges in GeV	[8, 12]	[12, 20]	[20, 40]	[40, 80]	[80, ∞)
$\lvert\eta(D^{(*)})\rvert$ bin edges	[0.0, 0.5]	[0.5, 1.0]	[1.0, 1.5]	[1.5, 2.0]	[2.0, 2.5]
$\Delta\phi(\ell, D^{(*)})$ bin edges	[0.0, 0.63]	[0.64, 1.28]	[1.28, 1.92]	[1.92, 2.56]	[2.56, 3.2]

Furthermore, to reduce statistical uncertainty, the absolute value of the pseudorapidity is used, as there is no additional discriminating power in measuring the sign of the pseudorapidity. The bin edges for $|\eta(D^{(*)})|$ are also provided in Table 9 as well as the bin edges for $\Delta\phi(\ell, D^{(*)})$.

This analysis achieves a higher resolution by dividing each of the five bins into five equally sized bins, resulting in a total of 25 bins, as it is displayed in the Figures 23 - 34. These binning schemes enable studying the kinematics of $W + D^{(*)}$ production and investigate various distributions effectively.

6.5 Kinematic Distributions

In this chapter, kinematic distributions in events with a W boson and a $D^{(*)}$ meson are considered as a function of $p_T^{D^{(*)}}$ (see Section 6.5.1), $|\eta(D^{(*)})|$ (see Section 6.5.2) and $\Delta\phi$ (see Section 6.5.3). A distinction is made between the OS-SS and the SS charge symmetric case. The ratio SS/OS-SS is also calculated. This can then be used to make statements about gluon splitting as a function of these three variables.

In order to analyze this, a Rivet (Robust Independent Validation of Experiment and Theory) [99] analysis was extended as part of this thesis. Rivet is particle physics MC analysis toolkit.

The plots shown in this section are all made using `Sherpa` samples. The corresponding plots made with `MadGraph` used later for the generator comparison in Section 6.6 can be found in the appendix (see Figures 42 - 53) as well as the tables giving an overview of the integrals of the histograms (see Tables 16 - 18).

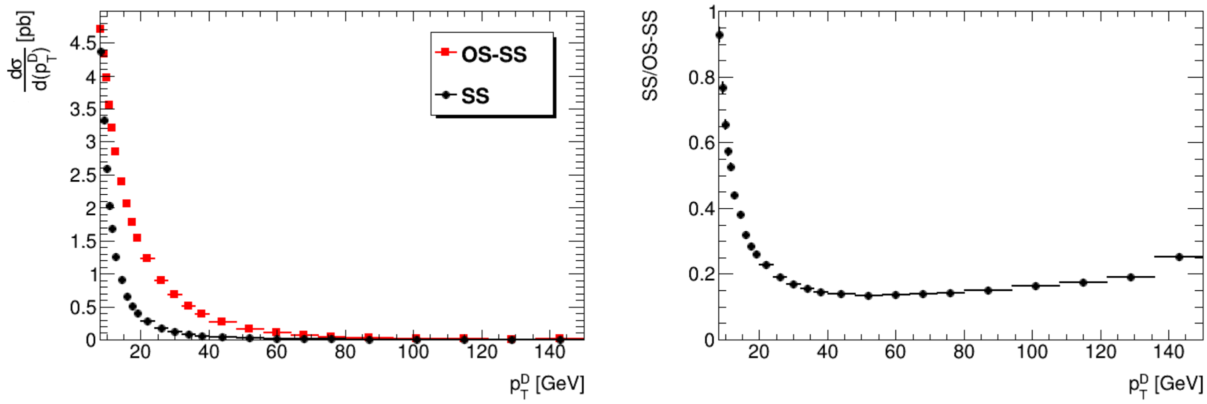

(a) (b)

Figure 23: Plots showing p_T^D in the W^+D^- channel. (a) displays the charge symmetric component in black and the OS-SS subtraction in red. (b) shows the corresponding ratio of SS/OS-SS.

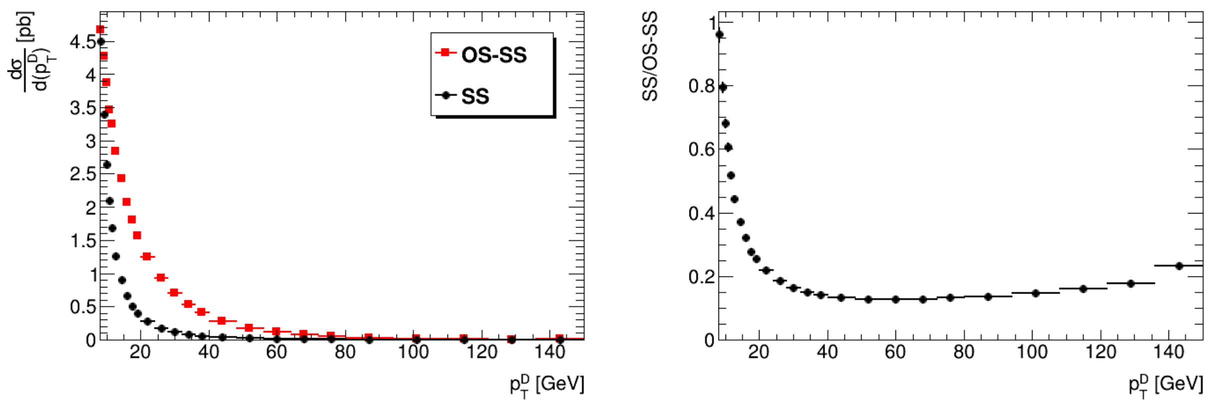

(a) (b)

Figure 24: Plots showing $p_T^{D^*}$ in the W^+D^{*-} channel. (a) displays the charge symmetric component in black and the OS-SS subtraction in red. (b) shows the corresponding ratio of SS/OS-SS.

6.5.1 Transverse Momentum

The four Figures 23 - 26 show the cross section for the transversal momentum of the $D^{(*)}$ meson, $p_T^{D^{(*)}}$. These SS and OS-SS plots (see (a)) show a similar shape for the different channels. The SS and OS-SS cross sections fall rapidly with the transverse momentum $p_T^{D^{(*)}}$.

By computing the SS/OS-SS ratio, it is possible quantify the relative contribution of gluon splitting to the background in different kinematic regions. The ratio plots (see (b)) in the

Figures 23 - 26 show that gluon splitting has dominantly low $p_T^{D^{(*)}}$ and rises slightly again at high $p_T^{D^{(*)}}$ values.

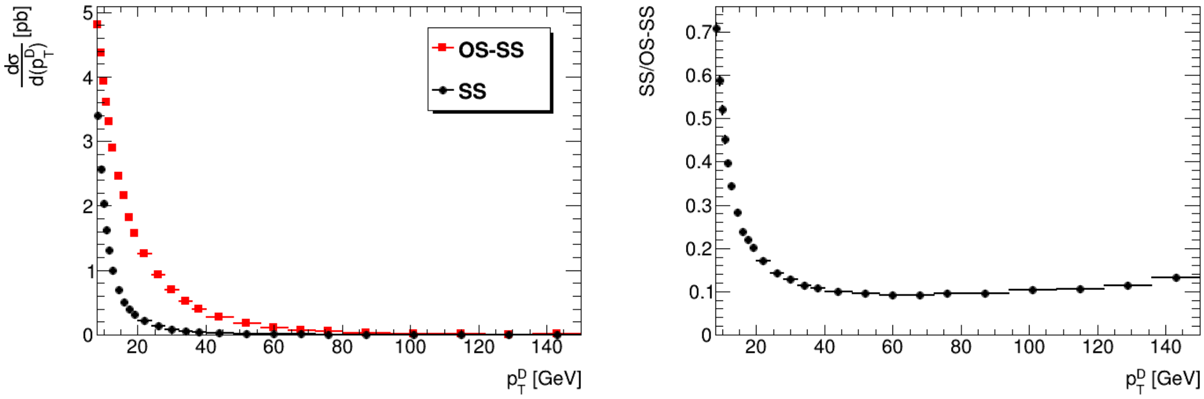

(a) (b)

Figure 25: Plots showing p_T^D in the W^-D^+ channel (a) displays the charge symmetric component in black and the OS-SS subtraction in red. (b) shows the corresponding ratio of SS/OS-SS.

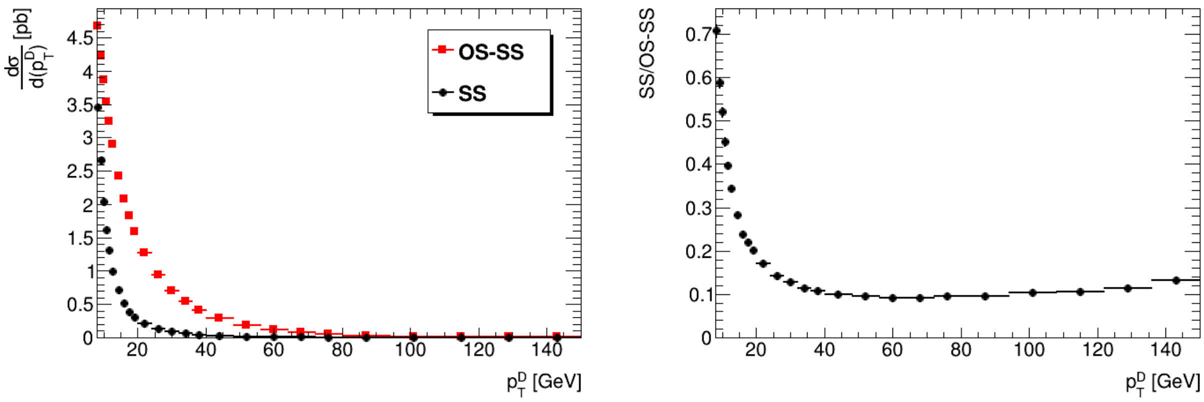

(a) (b)

Figure 26: Plots showing $p_T^{D^*}$ in the W^-D^{*+} channel. (a) displays the charge symmetric component in black and the OS-SS subtraction in red. (b) shows the corresponding ratio of SS/OS-SS.

The integral of these histograms are displayed in Table 10. The integrals across all bins are shown there for the four different channels, for the SS and OS components and OS-SS as well as the ratio SS/OS-SS. They are also shown separately for bins 1 to 12 and bins 13 to 25. The ratio of the yields for these two $p_T^{D^{(*)}}$ ranges indicates the relative importance of gluon splitting in the two regions.

Table 10: Integrals of histograms for $p_T^{D^{(*)}}$ from Sherpa. Bin 1-12 correspond to the bin edges 8 GeV to 28 GeV, whereas bin 13-25 correspond to the bin edges starting with 28 GeV and having no upper limit. The right column shows the ratio of the integral of the first 12 bins over the integral of the remaining bins from bin 13 to 25. The values are in pb.

Channel	Charge	Integral			Ratio
		Total	Bin 1-12	Bin 13-25	
$W^- + D^+$	SS	16.184 ± 0.031	14.796 ± 0.031	1.3885 ± 0.0042	10.660 ± 0.038
	OS	71.221 ± 0.077	56.937 ± 0.077	14.284 ± 0.016	3.98 ± 0.4
	OS-SS	55.0372 ± 0.084	42.142 ± 0.084	12.896 ± 0.017	3.27 ± 0.22
	SS/OS-SS	5.630 ± 0.026	4.260 ± 0.026	1.36974 ± 0.00049	3.11 ± 0.73
$W^+ + D^-$	SS	20.832 ± 0.036	18.963 ± 0.036	1.869 ± 0.005	10.146 ± 0.015
	OS	74.482 ± 0.071	60.215 ± 0.071	14.266 ± 0.016	4.218 ± 0.025
	OS-SS	53.650 ± 0.079	41.252 ± 0.079	12.397 ± 0.017	3.329 ± 0.029
	SS/OS-SS	7.643 ± 0.037	5.556 ± 0.037	2.0878 ± 0.00062	2.66 ± 0.11
$W^- + D^{*-}$	SS	16.37 ± 0.03	14.95 ± 0.03	1.4234 ± 0.0041	10.51 ± 0.14
	OS	71.601 ± 0.072	56.655 ± 0.072	14.947 ± 0.016	3.789 ± 0.037
	OS-SS	55.228 ± 0.078	41.704 ± 0.078	13.523 ± 0.016	3.082 ± 0.031
	SS/OS-SS	5.697 ± 0.026	4.372 ± 0.026	1.32479 ± 0.00047	3.298 ± 0.036
$W^+ + D^{*-}$	SS	21.056 ± 0.034	19.167 ± 0.034	1.8890 ± 0.0048	10.14 ± 0.14
	OS	75.651 ± 0.066	60.610 ± 0.066	15.041 ± 0.016	4.03 ± 0.04
	OS-SS	54.595 ± 0.074	41.443 ± 0.074	13.152 ± 0.017	3.155 ± 0.033
	SS/OS-SS	7.585 ± 0.037	5.633 ± 0.037	1.95194 ± 0.00056	2.884 ± 0.059

6.5.2 Pseudorapidity

The four Figures 27 - 30 show the cross section for the absolute pseudorapidity of the $D^{(*)}$ mesons, $|\eta(D^{(*)})|$. The SS and OS-SS plots (see (a)) show a similar shape for the different channels. The cross section decreases with increasing absolute pseudorapidity. The OS-SS subtraction has a greater negative gradient than the SS component.

The ratios, shown in Figures 27 - 30 (see (b)), increase with increasing $|\eta(D^{(*)})|$. The increase in SS/OS-SS with increasing $|\eta(D^{(*)})|$ is indicative of the enhanced contribution from gluon splitting processes at large $|\eta(D^{(*)})|$.

The integrals of these histograms are displayed in Table 11. The integrals across all bins are shown there for the four different channels, for the SS and OS components and OS-SS as well as the ratio SS/OS-SS. They are also shown separately for bins 1 to 12 and bins 13 to 25, as a lot of gluon splitting takes place in bins 1-12 in particular.

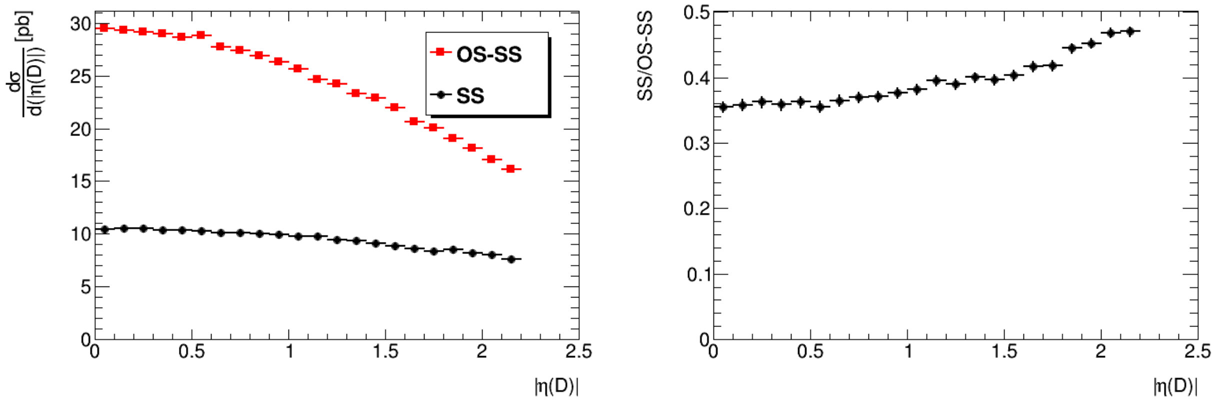

(a) (b)

Figure 27: Plots showing $|\eta(D)|$ in the W^+D^- channel. (a) displays the charge symmetric component in black and the OS-SS subtraction in red. (b) shows the corresponding ratio of SS/OS-SS.

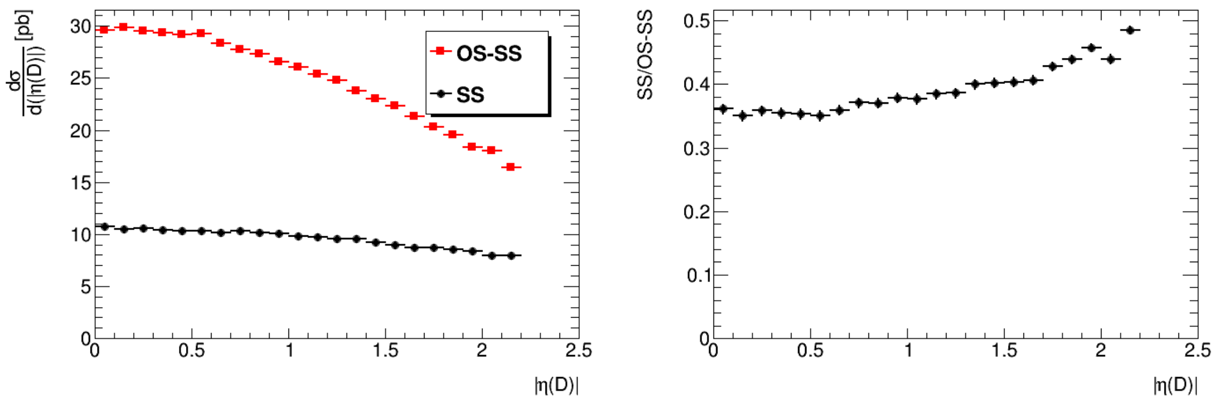

(a) (b)

Figure 28: Plots showing $|\eta(D^*)|$ in the W^+D^{*-} channel. (a) displays the charge symmetric component in black and the OS-SS subtraction in red. (b) shows the corresponding ratio of SS/OS-SS.

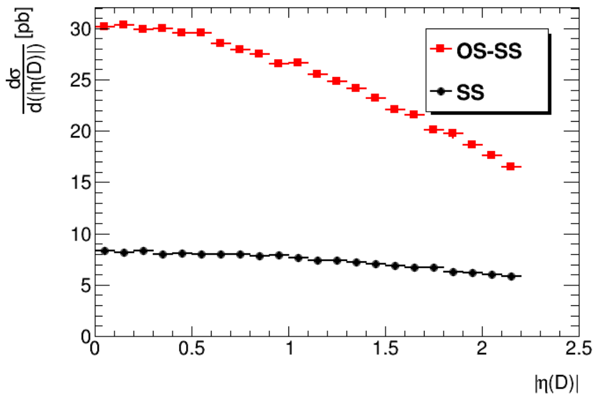

(a)

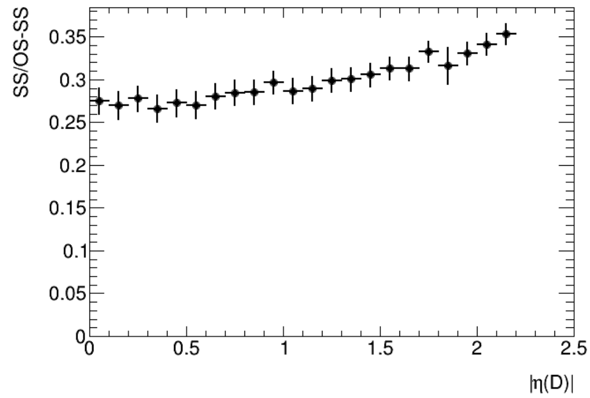

(b)

Figure 29: Plots showing $|\eta(D)|$ in the W^-D^+ channel. (a) displays the charge symmetric component in black and the OS-SS subtraction in red. (b) shows the corresponding ratio of SS/OS-SS.

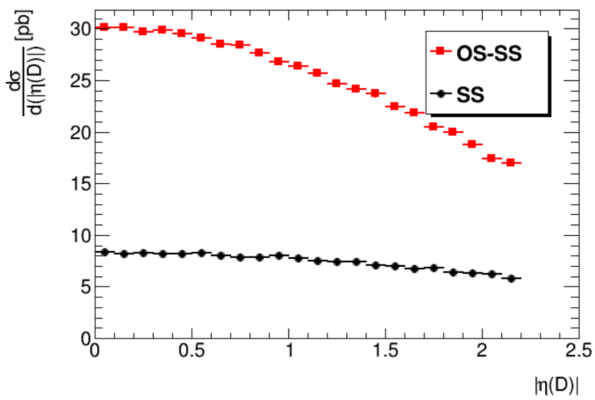

(a)

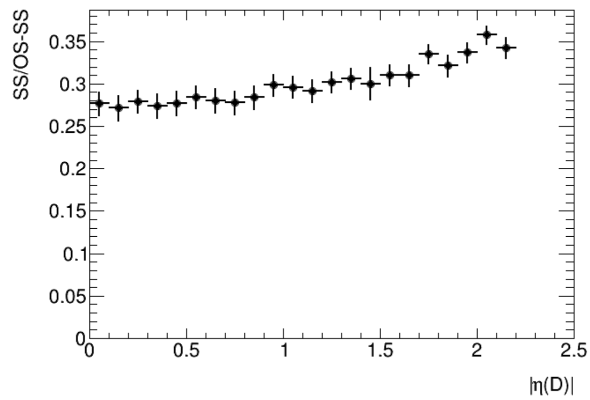

(b)

Figure 30: Plots showing $|\eta(D^*)|$ in the W^-D^{*+} channel. (a) displays the charge symmetric component in black and the OS-SS subtraction in red. (b) shows the corresponding ratio of SS/OS-SS.

Table 11: Integrals of histograms for $|\eta(D^{(*)})|$ from Sherpa. Bin 1-12 correspond to the bin edges 0.0 to 1.3, whereas bin 13-25 correspond to the bin edges 1.3 to 2.5. The right column shows the ratio of the integral of the first 12 bins over the integral of the remaining bins from bin 13 to 25. The values are in pb.

Channel	Charge	Integral			Ratio
		Total	Bin 1-12	Bin 13-25	
$W^- + D^+$	SS	16.184 ± 0.024	9.554 ± 0.024	6.630 ± 0.021	1.438 ± 0.044
	OS	71.221 ± 0.055	43.771 ± 0.055	27.450 ± 0.057	1.59 ± 0.07
	OS-SS	55.04 ± 0.06	34.22 ± 0.06	20.820 ± 0.061	1.642 ± 0.088
	SS/OS-SS	6.56 ± 0.07	3.356 ± 0.053	3.205 ± 0.046	1.047 ± 0.098
$W^+ + D^-$	SS	20.832 ± 0.027	12.230 ± 0.027	8.602 ± 0.024	1.423 ± 0.065
	OS	74.482 ± 0.056	45.535 ± 0.056	28.948 ± 0.046	1.573 ± 0.084
	OS-SS	53.650 ± 0.062	33.304 ± 0.062	20.346 ± 0.052	1.6 ± 0.1
	SS/OS-SS	8.678 ± 0.038	4.414 ± 0.029	4.264 ± 0.024	1.035 ± 0.087
$W^- + D^{*+}$	SS	16.374 ± 0.023	9.644 ± 0.023	6.73 ± 0.02	1.433 ± 0.056
	OS	71.601 ± 0.051	43.837 ± 0.051	27.764 ± 0.053	1.577 ± 0.071
	OS-SS	55.228 ± 0.056	34.193 ± 0.056	21.035 ± 0.057	1.627 ± 0.083
	SS/OS-SS	6.610 ± 0.064	3.389 ± 0.048	3.221 ± 0.042	1.05 ± 0.12
$W^+ + D^{*-}$	SS	21.056 ± 0.026	12.295 ± 0.026	8.760 ± 0.023	1.403 ± 0.077
	OS	75.651 ± 0.052	46.106 ± 0.052	29.545 ± 0.043	1.561 ± 0.077
	OS-SS	54.595 ± 0.058	33.810 ± 0.058	20.785 ± 0.049	1.629 ± 0.091
	SS/OS-SS	8.620 ± 0.036	4.371 ± 0.028	4.250 ± 0.023	1.029 ± 0.084

6.5.3 Azimuthal Angle

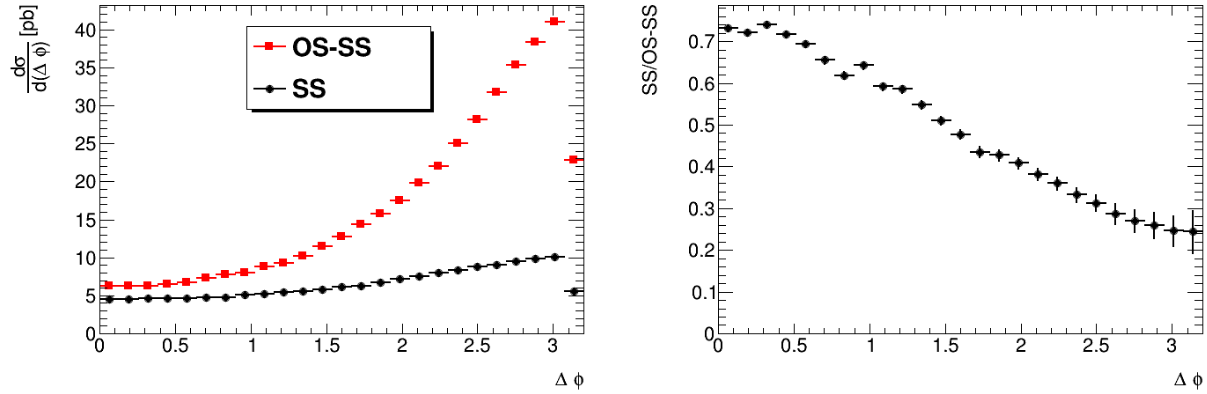

(a) (b)

Figure 31: Plots showing $\Delta\phi(\ell, D)$ in the W^+D^- channel (a) displays the SS charge symmetry in black and the OS-SS subtraction in red. (b) shows the corresponding ratio of SS/OS-SS.

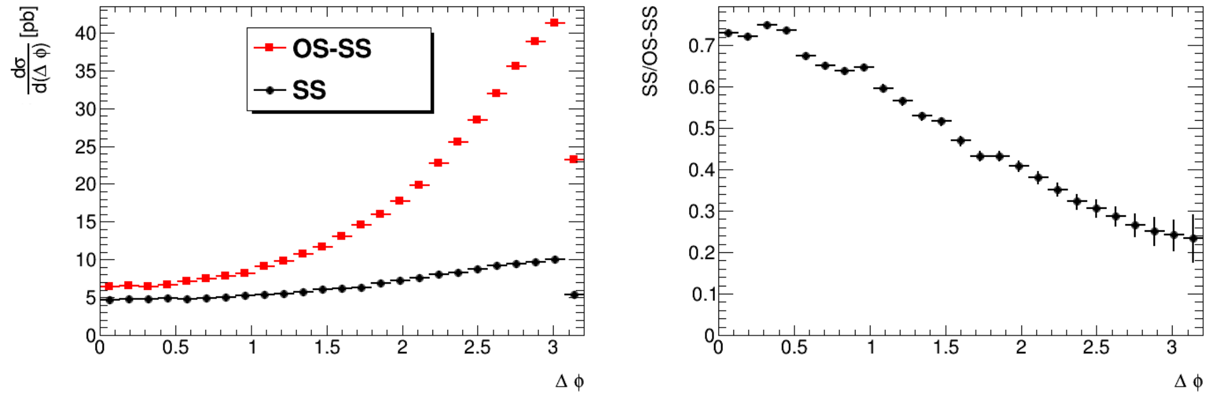

(a) (b)

Figure 32: Plots showing $\Delta\phi(\ell, D^*)$ in the W^+D^{*-} channel (a) displays the SS charge symmetry in black and the OS-SS subtraction in red. (b) shows the corresponding ratio of SS/OS-SS.

The four Figures 31 - 34 show the cross section for the azimuthal angle between the $D^{(*)}$ meson and the lepton, $\Delta\phi(\ell, D^{(*)})$. The OS-SS plots (see (a)) show a similar shape for all four channels. The cross section increases with increasing $\Delta\phi(\ell, D^{(*)})$, where the OS-SS subtraction has a much larger slope than the charge symmetric component.

The ratio plots in the Figures 31 - 34 (see (b)) show a decreasing behavior with increasing azimuthal angle. From this it can be concluded that gluon splitting occurs primarily at smaller azimuthal angles.

The integrals of these histograms are displayed in Table 12. The integrals across all bins are shown there for the four different channels, for the SS and OS components and OS-SS as well as the ratio SS/OS-SS. They are also shown separately for bins 1 to 12 and bins 13 to 25, as a lot of gluon splitting takes place in bins 1-12 in particular.

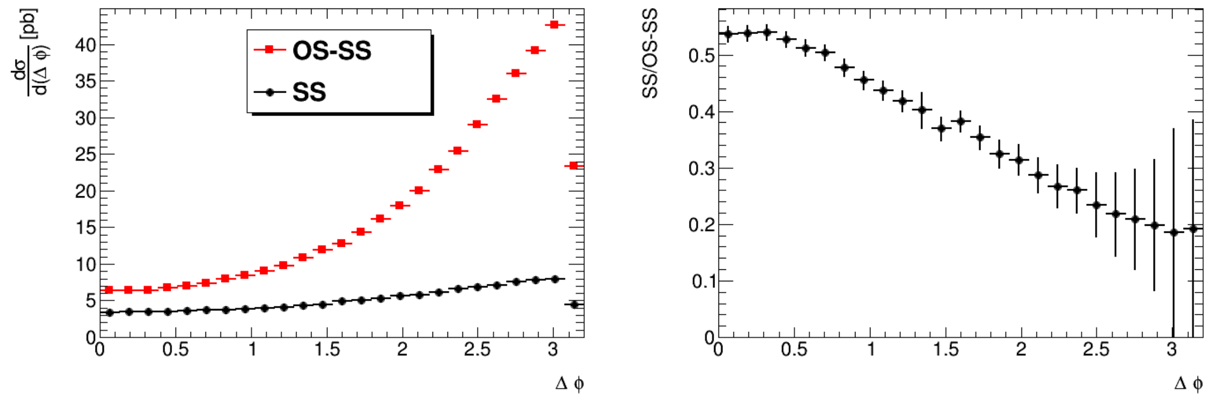

(a) (b)

Figure 33: Plots showing $\Delta\phi(\ell, D)$ in the W^-D^+ channel (a) displays the SS charge symmetry in black and the OS-SS subtraction in red. (b) shows the corresponding ratio of SS/OS-SS.

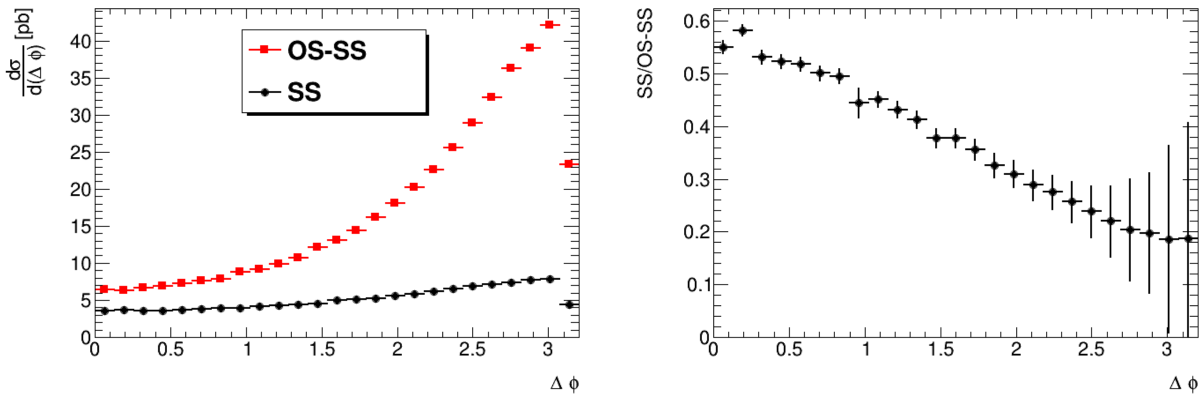

(a) (b)

Figure 34: Plots showing $\Delta\phi(\ell, D^*)$ in the $W^- D^{*+}$ channel (a) displays the SS charge symmetry in black and the OS-SS subtraction in red. (b) shows the corresponding ratio of SS/OS-SS.

Table 12: Integrals of histograms for $\Delta\phi(\ell, D^{(*)})$ from Sherpa. Bin 1-12 correspond to the bin edges 0.0 to 1.664, whereas bin 13-25 correspond to the bin edges 1.664 to 3.2. The right column shows the ratio of the integral of the first 12 bins over the integral of the reamining bins from 13 to 25. The values are in pb.

Channel	Charge	Integral			Ratio
		Total	Bin 1-12	Bin 13-25	
$W^- + D^+$	SS	16.18 ± 0.02	5.83 ± 0.02	10.353 ± 0.024	0.562 ± 0.062
	OS	71.221 ± 0.052	18.392 ± 0.052	52.829 ± 0.059	0.348 ± 0.029
	OS-SS	55.037 ± 0.056	12.562 ± 0.056	42.476 ± 0.064	0.296 ± 0.028
	SS/OS-SS	9.147 ± 0.334	5.718 ± 0.062	3.430 ± 0.328	1.67 ± 0.60
$W^+ + D^-$	SS	20.832 ± 0.023	7.645 ± 0.023	13.188 ± 0.028	0.579 ± 0.054
	OS	74.482 ± 0.041	19.756 ± 0.041	54.727 ± 0.060	0.361 ± 0.032
	OS-SS	53.650 ± 0.047	12.111 ± 0.047	41.539 ± 0.066	0.29 ± 0.03
	SS/OS-SS	12.196 ± 0.097	7.755 ± 0.033	4.441 ± 0.091	1.747 ± 0.261
$W^- + D^{*+}$	SS	16.374 ± 0.019	6.025 ± 0.019	10.349 ± 0.023	0.582 ± 0.058
	OS	71.601 ± 0.049	18.773 ± 0.049	52.828 ± 0.055	0.355 ± 0.033
	OS-SS	55.228 ± 0.053	12.748 ± 0.053	42.480 ± 0.059	0.299 ± 0.031
	SS/OS-SS	9.242 ± 0.344	5.818 ± 0.056	3.424 ± 0.339	1.701 ± 0.598
$W^+ + D^{*-}$	SS	21.056 ± 0.022	7.881 ± 0.022	13.174 ± 0.026	0.598 ± 0.066
	OS	75.651 ± 0.038	20.391 ± 0.038	55.260 ± 0.056	0.369 ± 0.034
	OS-SS	54.595 ± 0.044	12.509 ± 0.044	42.086 ± 0.062	0.297 ± 0.031
	SS/OS-SS	12.133 ± 0.099	7.750 ± 0.030	4.384 ± 0.095	1.769 ± 0.243

6.6 Generator Comparison

The samples, which are discussed in more detail in Section 5, will now be compared with each other. For this purpose, the two `Sherpa` samples and the two `MadGraph` samples were merged and the ratio, which is now considered for the two observances and for all covered channels, is as follows:

$$r = \frac{(\mathrm{SS/OS-SS})_{\mathrm{MadGraph}}}{(\mathrm{SS/OS-SS})_{\mathrm{Sherpa}}}. \tag{6.1}$$

This approach aims for a comparison regarding the shape of the OS-SS plots. Thus in the following only the shape of the plots will be discussed.

6.6.1 Transverse Momentum

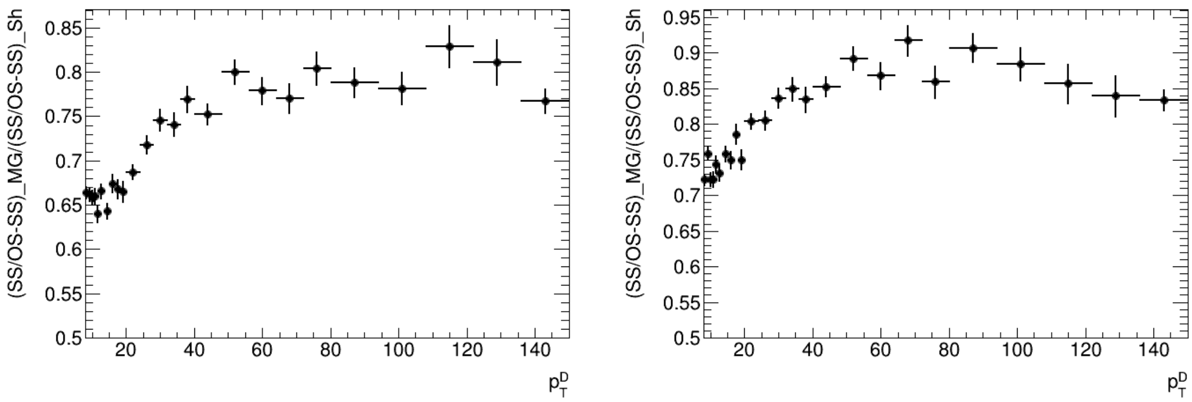

(a) (b)

Figure 35: Plots showing the ratio of the cross section ratio SS/(OS-SS) for `MadGraph` to the same observable for `Sherpa` as a function of $p_T^{D^{(*)}}$ with a W^+. (a) shows the W^+D^- channel whereas (b) corresponds to the W^+D^{*-} channel.

Figure 37 shows the SS/OS-SS ratio for `Sherpa` (see Figure 37a) and for `MadGraph` (see Figure 37b) side by side. The actual generator comparison is then done in Figure 36a. The Figures 35 and 36 show the comparison for $p_T^{D^{(*)}}$. Figures 35a and 35b are very similar and show that the ratio increases for small values of p_T and falls again slightly for higher p_T. This means that `MadGraph` predicts less gluon splitting for low and particularly high values of p_T in comparison to `Sherpa`.

A similar behavior can be seen in the Figures 36a and 36b. The ratio increases with

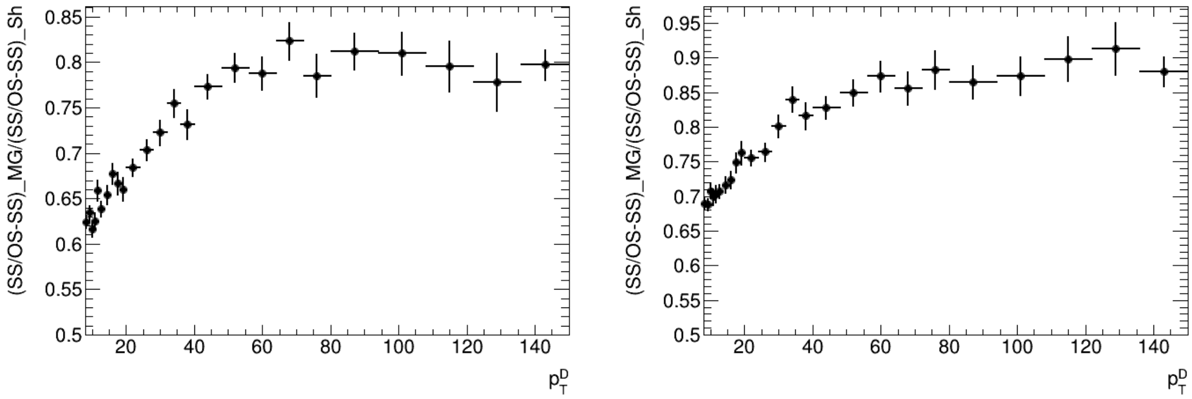

(a) (b)

Figure 36: Plots showing the ratio of the cross section ratio SS/(OS-SS) for `MadGraph` to the same observable for `Sherpa` as a function of $p_T^{D^{(*)}}$ with a W^-. (a) shows the W^-D^+ channel whereas (b) corresponds to the W^-D^{*+} channel.

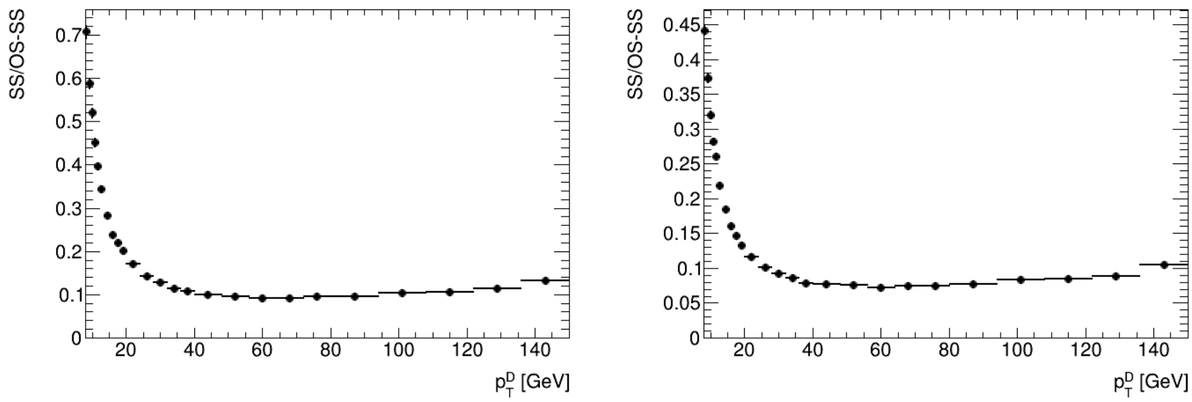

(a) (b)

Figure 37: Plots showing the ratio SS/OS-SS in the observable $p_T(D^+)$ with a W^-. (a) shows Sherpa samples (similar as in Figure 25), whereas (b) corresponds to the MadGraph samples. The comparison between these two is shown in Figure 36a.

increasing p_T, especially rather fast for low p_T. This indicates that there is a discrepancy between the predictions of `Sherpa` and `MadGraph` in this kinematic regime.
The integrals of the different generator comparison plots for p_T can be found in Table 13.

6.6.2 Pseudorapidity

If the pseudorapdity of the $D^{(*)}$ meson is now considered in the Figures 38 and 39, it is noticeable that the `MadGraph` and `Sherpa` are consistent with having the same shape but

Table 13: Integrals of (SS/OS-SS)MG/(SS/OS-SS)Sh for $p_T^{D()}$, along with their uncertainties and the ratio of the two bin ranges.

Channel	Total	Bin 1-12	Bin 13-25	Ratio
$W^- + D^+$	18.008 ± 0.083	7.843 ± 0.037	10.165 ± 0.075	0.772 ± 0.023
$W^+ + D^-$	18.14 ± 0.07	8.005 ± 0.033	10.139 ± 0.062	0.789 ± 0.033
$W^- + D^+$	19.847 ± 0.098	8.668 ± 0.043	11.179 ± 0.089	0.775 ± 0.038
$W^+ + D^{*-}$	20.286 ± 0.084	9.05 ± 0.04	11.232 ± 0.074	0.805 ± 0.041

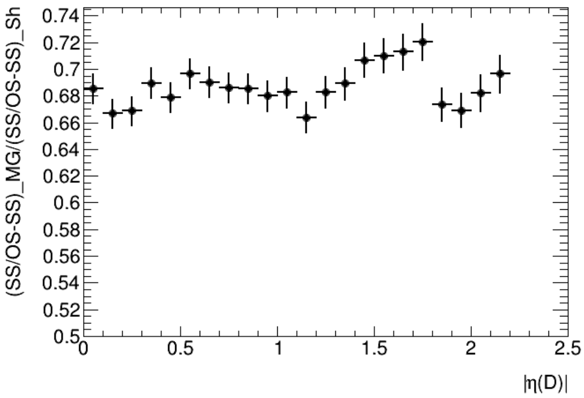

(a)

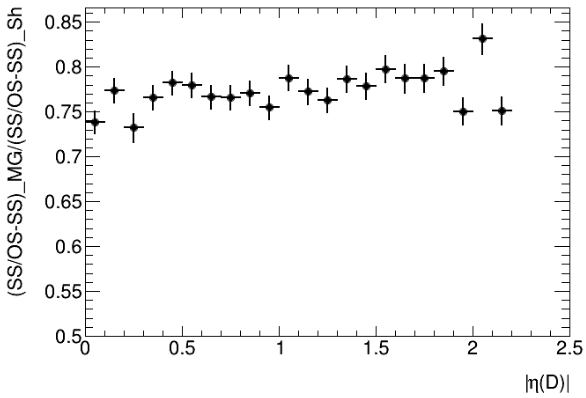

(b)

Figure 38: Plots showing the ratio of the cross section ratio SS/(OS-SS) for `MadGraph` to the same observable for `Sherpa` as a function of $|\eta(D^{(*)})|$ with a W^+. (a) shows the W^+D^- channel whereas (b) corresponds to the W^+D^{*-} channel.

different normalization in comparison to the transverse momentum. Nevertheless, there are fluctuations that indicate that the two generators make different statements about gluon splitting.

The integrals of these ratios can be seen in Table 14.

Table 14: Integrals of (SS/OS-SS)MG/(SS/OS-SS)Sh for $|\eta(D^{(*)})|$, along with their uncertainties and the ratio of the two bin ranges.

Channel	Total	Bin 1-10	Bin 11-25	Ratio
$W^- + D^+$	14.749 ± 0.063	6.650 ± 0.039	8.100 ± 0.049	0.821 ± 0.061
$W^+ + D^-$	15.119 ± 0.057	6.828 ± 0.036	8.291 ± 0.044	0.822 ± 0.061
$W^- + D^+$	16.289 ± 0.073	7.375 ± 0.046	8.914 ± 0.057	0.828 ± 0.062
$W^+ + D^-$	17.018 ± 0.068	7.629 ± 0.043	9.389 ± 0.053	0.812 ± 0.059

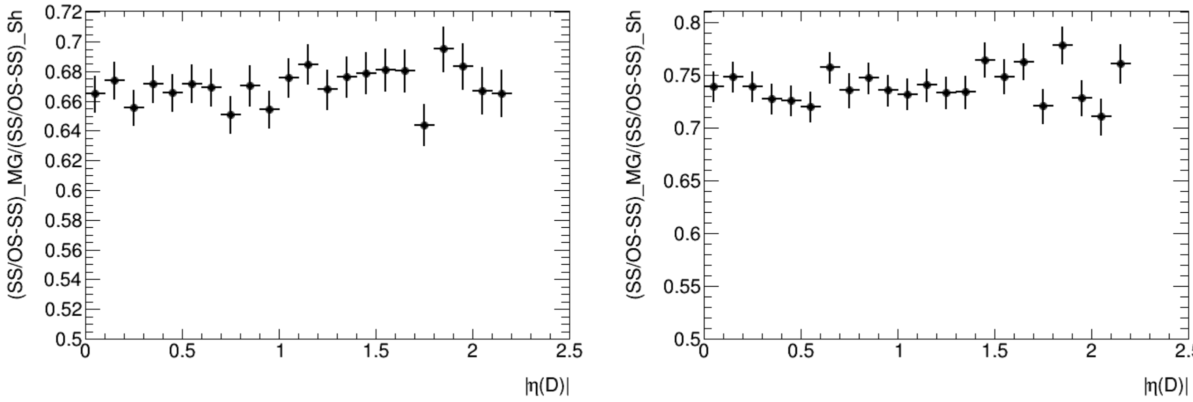

(a)

(b)

Figure 39: Plots showing the ratio of the cross section ratio SS/(OS-SS) for `MadGraph` to the same observable for `Sherpa` as a function of $|\eta(D^{(*)})|$ with a W^-. (a) shows the W^-D^+ channel whereas (b) corresponds to the W^-D^{*+} channel.

6.6.3 Azimuthal Angle

Finally, the two generators are considered in relation to the statements regarding gluon splitting in the variable azimuthal angle. Figures 40 and 41 show that the ratio (SS/OS-SS)$_{\mathrm{MG}}$/(SS/OS-SS)$_{\mathrm{Sh}}$ also increases with increasing $\Delta\phi(\ell, D^{(*)})$. Again, this shows that `MadGraph` predicts less gluon splitting than `Sherpa`, this time at higher values for $\Delta\phi(\ell, D^{(*)})$. An overview of the corresponding integrals is given in Table 15.

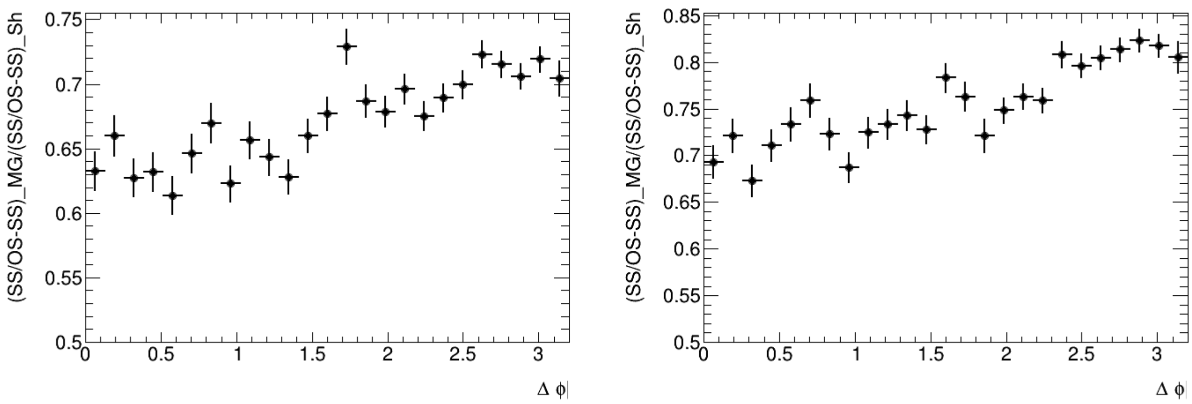

(a)

(b)

Figure 40: Plots showing the ratio of the cross section ratio SS/(OS-SS) for `MadGraph` to the same observable for `Sherpa` as a function of $\Delta\phi(\ell, D^{(*)})$ with a W^+. (a) shows the W^+D^- channel whereas (b) corresponds to the W^+D^{*-} channel.

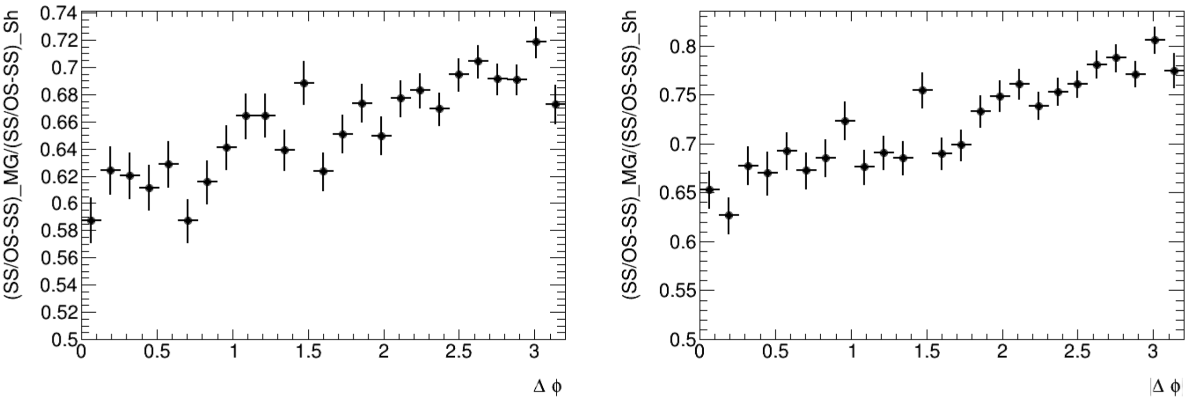

(a) (b)

Figure 41: Plots showing the ratio of the cross section ratio SS/(OS-SS) for `MadGraph` to the same observable for `Sherpa` as a function of $\Delta\phi(\ell, D^{(*)})$ with a W^-. (a) shows the W^-D^+ channel whereas (b) corresponds to the W^-D^{*+} channel.

Table 15: Integrals of (SS/OS-SS)MG/(SS/OS-SS)Sh for $\Delta\phi(\ell, D^{(*)})$, along with their uncertainties and the ratio of the two bin ranges.

Channel	Total	Bin 1-12	Bin 13-25	Ratio
$W^- + D^+$	16.372 ± 0.073	7.573 ± 0.056	8.799 ± 0.046	0.861 ± 0.078
$W^+ + D^-$	16.793 ± 0.066	7.692 ± 0.050	9.100 ± 0.042	0.845 ± 0.075
$W^- + D^+$	18.012 ± 0.084	8.207 ± 0.065	9.804 ± 0.053	0.837 ± 0.079
$W^+ + D^{*-}$	18.836 ± 0.078	8.630 ± 0.059	10.206 ± 0.052	0.846 ± 0.077

7 Conclusion and Outlook

In this work, the kinematic distribution in W boson and $D^{(*)}$ meson production in proton-proton collisions was analyzed using Monte Carlo data. Three different observables were analyzed. The analysis indicates that gluon splitting has dominantly low $p_T^{D^{(*)}}$. Furthermore, the results indicate that especially for large absloute pseudorapidity of the $D^{(*)}$ meson, $|\eta(D^{(*)})|$, the contribution of gluon splitting is enhanced. The analysis also yields information that gluon splitting occurs primarily at smaller azimuthal angles $\Delta\phi(\ell, D^{(*)})$ between the $D^{(*)}$ meson and the charged lepton.

Furthermore, the two generators used for the aforementioned analysis, namely `Sherpa` and `MadGraph`, were compared with each other. This comparison showed that `MadGraph` predicts less gluon splitting than `Sherpa` for both low $p_T^{D^{(*)}}$ and high $\Delta\phi(\ell, D^{(*)})$. The comparison in the obseravble $|\eta(D^{(*)})|$ also showed that the two generators make different predictions with regard to gluon splitting, even though in $|\eta(D^{(*)})|$ there is no distinguished range in which particularly high discrepancies occur.

For further analysis, it would first be interesting to make a distinction between the processes presented in Section 3.3. In other words, a quantitative analysis that distinguishes between the events $g \to c\bar{c}$ and $g \to b\bar{b}$.
Furthermore, it would be interesting to extend the truth level analysis and look at more different samples with other production processes.
It might be relevant to look for other variables that are also or even better suited for the analysis of gluon splitting.
In addition, it would of course be interesting and relevant to bring the analysis up to a reconstruction level, i.e. to work with reconstructed simulated data and then compare it with data from the ATLAS experiment.

In summary, it can be said that the work presented here has provided some indications of the behavior of gluon splitting in $W + D^{(*)}$ events and a further, more in-depth analysis could provide interesting results that could contribute to more accurate measurements of the strange PDF.

References

[1] ATLASCollab., “Measurement of the production of a w boson in association with a charmed hadron in pp collisions at $\sqrt{s} = 13$ TeV with the atlas detector,” *Phys. Rev. D*, vol. 108, p. 032012, Aug 2023. [Online]. Available: https://link.aps.org/doi/10.1103/PhysRevD.108.032012

[2] M. E. Peskin and D. V. Schroeder, *An Introduction to quantum field theory.* Reading, USA: Addison-Wesley, 1995.

[3] HermesCollab., “Measurement of parton distributions of strange quarks in the nucleon from charged-kaon production in deep-inelastic scattering on the deuteron,” *Phys. Lett. B*, vol. 666, p. 446, 2008.

[4] ZEUSCollab., “Charm production in charged current deep inelastic scattering at hera,” *JHEP*, vol. 05, p. 201, 2019.

[5] CcfrCollab., “Determination of the strange quark content of the nucleon from a next-to-leading order qcd analysis of neutrino charm production,” *Z. Phys.*, vol. C, no. 65, p. 189, 1995.

[6] NuTeVCollab and M. of, “the nucleon strange-antistrange asymmetry at next-to-leading order in qcd from nutev dimuon data,” *Phys. Rev. Lett.*, vol. 99, 2007.

[7] NomadCollab., “A precision measurement of charm dimuon production in neutrino interactions from the nomad experiment,” *Nucl. Phys. B*, vol. 876, p. 339, 2013.

[8] ATLASCollab., “Determination of the parton distribution functions of the proton using diverse atlas data from pp collisions at $\sqrt{s}$= 7,” *8 and*, vol. 82, p. 438, 2021.

[9] ——, “Precision measurement and interpretation of inclusive w^+,” *W^- and Z/γ^* production cross sections with the ATLAS detector, Eur. Phys. J.*, vol. C, no. 77, p. 367, 2017.

[10] F. Faura, S. Iranipour, E. R. Nocera, J. Rojo, and M. Ubiali, “The strangest proton?” *Eur. Phys. J.*, vol. C, no. 80, p. 1168, 2020.

[11] U. Baur, F. Halzen, S. Keller, M. L. Mangano, and K. Riesselmann, “The charm content of $w + 1$ jet events as a probe of the strange quark distribution function,” *Phys. Lett. B*, vol. 318, p. 544, 1993.

[12] W. T. Giele, S. Keller, and E. Laenen, "Qcd corrections to w boson plus heavy quark production at the tevatron," *Phys. Lett. B*, vol. 372, p. 141, 1996.

[13] CdfCollab., "Observation of the production of a w boson in association with a single charm quark," *Phys. Rev. Lett.*, vol. 110, 2013, article 071801.

[14] ATLASCollab., "Measurement of the production of a w boson in association with a charm quark in pp collisions at $\sqrt{s} = 7$ with the atlas detector," *JHEP*, vol. 05, p. 068, 2014.

[15] CMSCollab., "Measurement of associated w + charm production in pp collisions at $\sqrt{s} = 7$," *JHEP*, vol. 02, p. 013, 2014.

[16] ——, "Measurement of associated production of a w boson and a charm quark in proton-proton collisions at $\sqrt{s} = 7$," *Eur. Phys. J.*, vol. C, no. 79, p. 269, 2019.

[17] LHCbCollab., "Study of w boson production in association with beauty and charm, phys," *Rev.*, vol. 92, 2015, article 052001.

[18] E. Bothmann *et al.*, "Event generation with sherpa 2.2," 2019, sciPost Phys. 7 034.

[19] J. Alwall, R. Frederix, S. Frixione *et al.*, "The automated computation of tree-level and next-to-leading order differential cross sections, and their matching to parton shower simulations," *J. High Energ. Phys.*, vol. 2014, p. 79, 2014.

[20] H. Geiger, L. Rutherford, E. Regener, F. A. Lindemann, C. T. R. Wilson, J. Chadwick, L. H. Gray, G. T. P. Tarrant, G. M. B. Dobson, W. Bragg, O. W. Richardson, A. Eddington, F. Soddy, and S. Chapman, "Discussion on ultra-penetrating rays," *Proceedings of the Royal Society of London. Series A, Containing Papers of a Mathematical and Physical Character*, vol. 132, no. 819, pp. 331–352, 1931. [Online]. Available: http://www.jstor.org/stable/95583

[21] P. J. Bryant, "A brief history and review of accelerators," 1994. [Online]. Available: https://api.semanticscholar.org/CorpusID:53570660

[22] ParticleDataGroup, "Review of Particle Physics, 2020-2021. RPP," *PTEP*, vol. 2020, no. 8, p. 083C01, 2020. [Online]. Available: https://cds.cern.ch/record/2729066

[23] P. A. M. Dirac, "The quantum theory of the electron," *Proceedings of the Royal Society of London. Series A, Containing Papers of a Mathematical and*

Physical Character, vol. 117, no. 778, pp. 610–624, 1928. [Online]. Available: http://www.jstor.org/stable/94981

[24] P. Stewart, "Charles janet: Unrecognized genius of the periodic system," *Foundations of Chemistry*, vol. 12, pp. 5–15, 04 2010.

[25] M. Kaku and J. Thompson, *Beyond Einstein: The Cosmic Quest for the Theory of the Universe*, ser. Oxford paperbacks. Oxford University Press, 1997.

[26] D. Griffiths, *Introduction to Elementary Particles*, ser. Physics textbook. Wiley, 2008.

[27] E. Fermi, "Versuch einer theorie der β-strahlen." *Zeitschrift für Physik*, vol. 88, pp. 161–177, 1934. [Online]. Available: https://api.semanticscholar.org/CorpusID:125763380

[28] F. Wilczek, "Quantum chromodynamics: The modern theory of the strong interaction," *Annual Review of Nuclear and Particle Science*, vol. 32, pp. 177–209, 1982. [Online]. Available: https://api.semanticscholar.org/CorpusID:260497955

[29] A. Jain, "Notes on symmetries in particle physics," 2021.

[30] "Observation of a new particle in the search for the standard model higgs boson with the atlas detector at the lhc," *Physics Letters B*, vol. 716, no. 1, p. 1–29, Sep. 2012. [Online]. Available: http://dx.doi.org/10.1016/j.physletb.2012.08.020

[31] S. Carroll and T. Company, *Dark Matter, Dark Energy: The Dark Side of the Universe*, ser. Great courses. Teaching Company, LLC, 2007. [Online]. Available: https://books.google.de/books?id=oSGEXwAACAAJ

[32] J. D. Lykken, "Beyond the standard model," 2011.

[33] J. Woithe, G. J. Wiener, and F. F. V. der Veken, "Let's have a coffee with the standard model of particle physics!" *Physics Education*, vol. 52, no. 3, p. 034001, mar 2017. [Online]. Available: https://dx.doi.org/10.1088/1361-6552/aa5b25

[34] Cush. (2019) Standard model of elementary particles.svg. [Online]. Available: https://en.wikipedia.org/wiki/File:Standard_Model_of_Elementary_Particles.svg

[35] M. Drewes, "The phenomenology of right handed neutrinos," *Int. J. Mod. Phys. E*, vol. 1330019, 2013.

[36] F. Capozzi, E. Lisi, A. Marrone, D. Montanino, and A. Palazzo, "Neutrino masses and mixings: Status of known and unknown 3ν parameters," *Nuclear Physics B*, vol. 908, p. 218–234, Jul. 2016. [Online]. Available: http://dx.doi.org/10.1016/j.nuclphysb.2016.02.016

[37] LHCbCollab., "First observation of a doubly charged tetraquark and its neutral partner," *Phys. Rev. Lett.*, vol. 131, no. 4, 2023.

[38] L. collaboration, R. Aaij, C. Abellan Beteta, B. Adeva, M. Adinolfi, C. Aidala, Z. Ajaltouni, S. Akar, P. Albicocco, J. Albrecht, F. Alessio, M. Alexander, A. Albero, G. Alkhazov, P. Cartelle, J. Alves, S. Amato, Y. Amhis, L. An, and S. Zucchelli, "Observation of a narrow pentaquark state, $p_c(4312)^+$, and of two-peak structure of the $p_c(4450)^+$,″ 042019.

[39] T. Aaltonen *et al.*, "High-precision measurement of the W boson mass with the CDF II detector," *Science*, vol. 376, no. 6589, pp. 170–176, 2022.

[40] S. Chatrchyan, V. Khachatryan, A. Sirunyan, A. Tumasyan, W. Adam, T. Bergauer, M. Dragicevic, J. Erö, C. Fabjan, M. Friedl, R. Frühwirth, V. Ghete, J. Hammer, M. Hoch, N. Hörmann, J. Hrubec, M. Jeitler, W. Kiesenhofer, and D. Wenman, "Observation of a new boson at a mass of 125 gev with the cms experiment at the lhc," *Physics Letters B*, vol. 716, pp. 30–61, 08 2012.

[41] R. P. Feynman, "Space - time approach to quantum electrodynamics," in *Phys*, Rev., Ed. L. M. Brown, Ed: vol. 76, 1949, pp. 769–789.

[42] J. S. Schwinger, "On quantum electrodynamics and the magnetic moment of the electron," *Phys. Rev.*, vol. 73, pp. 416–417, 1948.

[43] S. Tomonaga, "On a relativistically invariant formulation of the quantum theory of wave fields," *Prog. Theor. Phys.*, vol. 1, pp. 27–42, 1946.

[44] N. Bezginov *et al.*, "A measurement of the atomic hydrogen lamb shift and the proton charge radius," *Science*, vol. 365, no. 6457, pp. 1007–1012, 2019.

[45] ACMECollab., "Improved limit on the electric dipole moment of the electron," *Nature*, vol. 562, no. 7727, pp. 355–360, 2018.

[46] S. L. Glashow, "Partial symmetries of weak interactions," *Nucl. Phys.*, vol. 22, pp. 579–588, 1961.

[47] A. Salam and J. C. Ward, "Electromagnetic and weak interactions," *Phys. Lett.*, vol. 13, pp. 168–171, 1964.

[48] S. Weinberg, "A model of leptons," *Phys. Rev. Lett.*, vol. 19, pp. 1264–1266, 1967.

[49] T. Nakano and K. Nishijima, "Charge independence for v-particles," *Prog. Theor. Phys.*, vol. 10, pp. 581–582, 1953.

[50] C. S. Wu *et al.*, "Experimental test of parity conservation in β decay," *Phys. Rev.*, vol. 105, pp. 1413–1414, 1957.

[51] J. Ellis, "Higgs physics," 2013.

[52] H. Fritzsch, M. Gell-Mann, and H. Leutwyler, "Advantages of the color octet gluon picture," *Phys. Lett. B*, vol. 47, pp. 365–368, 1973.

[53] T. Potter. Lecture notes 7. [Online]. Available: https://www.hep.phy.cam.ac.uk/~chpotter/particleandnuclearphysics/Lecture_07_QCD.pdf

[54] [Online]. Available: https://cds.cern.ch/record/1699952/files/Figures_T_Cross-section_at_LHC.png

[55] B. Povh, K. Rith, C. Scholz, and F. Zetsche, *Povh, B: Teilchen und Kerne.: Eine Einführung in die physikalischen Konzepte.*, ser. Physics and astronomy online library. Springer, 2004.

[56] (2015) Das genaueste bild des protons. [Online]. Available: https://www.desy.de/aktuelles/news_suche/index_ger.html?openDirectAnchor=829

[57] R. D. Ball, V. Bertone, S. Carrazza, L. D. Debbio, S. Forte, P. Groth-Merrild, A. Guffanti, N. P. Hartland, Z. Kassabov, J. I. Latorre, E. R. Nocera, J. Rojo, L. Rottoli, E. Slade, and M. Ubiali, "Parton distributions from high-precision collider data: Nnpdf collaboration," *The European Physical Journal C*, vol. 77, no. 10, Oct. 2017. [Online]. Available: http://dx.doi.org/10.1140/epjc/s10052-017-5199-5

[58] D. Hassel. (2024) The zeus experiment. [Online]. Available: https://www.mit.edu/~hasell/DKH_zeus.html

[59] *LEP design report*, ser. Report. Geneva: CERN, 1984, copies shelved as reports in LEP, PS and SPS libraries. [Online]. Available: https://cds.cern.ch/record/102083

[60] O. Press, "CERN Brochure - LHC Guide FAQ's," 2010. [Online]. Available: https://cds.cern.ch/record/2851505

[61] O. S. Brüning, P. Collier, P. Lebrun, S. Myers, R. Ostojic, J. Poole, and P. Proudlock, *LHC Design Report*, ser. CERN Yellow Reports: Monographs. Geneva: CERN, 2004. [Online]. Available: https://cds.cern.ch/record/782076

[62] CMSCollab., "The CMS experiment at the CERN LHC. The Compact Muon Solenoid experiment," *JINST*, vol. 3, p. S08004, 2008, also published by CERN Geneva in 2010. [Online]. Available: https://cds.cern.ch/record/1129810

[63] "The LHCb Detector at the LHC," *JINST*, vol. 3, p. S08005, 2008, also published by CERN Geneva in 2010. [Online]. Available: https://cds.cern.ch/record/1129809

[64] "The alice experiment at the cern lhc," *Journal of Instrumentation*, vol. 3, 2008.

[65] D. Boussard and T. P. R. Linnecar, "The LHC Superconducting RF System," CERN, Geneva, Tech. Rep., 1999. [Online]. Available: https://cds.cern.ch/record/410377

[66] F. Landua, "The CERN accelerator complex layout in 2022. Complexe des accélérateurs du CERN en janvier 2022," 2022, general Photo. [Online]. Available: https://cds.cern.ch/record/2813716

[67] ATLASCollab. (2023) Public atlas luminosity results for run-2 of the lhc. [Online]. Available: https://twiki.cern.ch/twiki/bin/view/ATLASPublic/LuminosityPublicResultsRun2

[68] ——, "The atlas experiment at the cern large hadron collider: A description of the detector configuration for run 3," 2023.

[69] (2024) Atlas overview. [Online]. Available: https://mediaarchive.cern.ch/MediaArchive/Photo/Public/2008/0803012/0803012_01/0803012_01-A4-at-144-dpi.jpg

[70] B. Cote, "A search for long-lived neutral particles decaying to oppositely charged lepton pairs in pp collisions at $\sqrt{s} = 13$ TeV with the ATLAS detector," 2023, presented 20 Nov 2023. [Online]. Available: https://cds.cern.ch/record/2882651

[71] JabberWok. Pseudorapidity2. [Online]. Available: https://commons.wikimedia.org/wiki/File:Pseudorapidity2.png

[72] DESY, "Particle Identification Performance of the ATLAS Transition Radiation Tracker," *ATLAS*, 2011. [Online]. Available: https://bib-pubdb1.desy.de/record/94409

[73] ATLASCollab. (2024) Calorimeter. [Online]. Available: https://ATLAS.cern/Discover/Detector/Calorimeter

[74] H. Zhang and A. Group, "The atlas liquid argon calorimeter: Overview and performance," *Journal of Physics Conference Series*, vol. 293, pp. 2044–, 04 2011.

[75] "Atlas tile calorimeter: Technical design report," 12 1996.

[76] G. Aielli *et al.*, "The rpc first level muon trigger in the barrel of the atlas experiment," *Nuclear Physics B*, vol. 158, p. 11, 2006.

[77] A. S. White, *Searches for the Rare Decay of the Higgs Boson to Two Muons and for New Physics in Dilepton Final States with the ATLAS Experiment.* University of Michigan, 2021.

[78] A. Yamamoto *et al.*, "Progress in atlas central solenoid magnet," *IEEE Transactions on Applied Superconductivity*, vol. 10, p. 353, 2000.

[79] S. M. Shaw and A. Collaboration, "The Run-2 ATLAS Trigger System," 2016. [Online]. Available: https://cds.cern.ch/record/2127944

[80] P. Clifford, "5 - monte carlo methods," in *Statistical Methods for Physical Science, volume 28 of Methods in Experimental Physics*, J. L. Stanford and S. B. Vardeman, Eds. Academic Press, 1994, pp. 125–153.

[81] T. Gleisberg *et al.*, "Event generation with sherpa 1.1," *Journal of High Energy Physics*, vol. 2009, no. 02, 2009.

[82] G. Luisoni. An introduction to powheg. [Online]. Available: https://indico.cern.ch/event/656211/contributions/2673382/attachments/1498653/2333153/luisoni_powheg.pdf

[83] "Studies of theoretical uncertainties on the measurement of the mass of the W boson at the LHC," CERN, Geneva, Tech. Rep., 2014, all figures including auxiliary figures are available at https://ATLAS.web.cern.ch/ATLAS/GROUPS/PHYSICS/PUBNOTES/ATL-PHYS-PUB-2014-015. [Online]. Available: https://cds.cern.ch/record/1956455

[84] M. Bähr *et al.*, "Herwig++ physics and manual," *The European Physical Journal C*, vol. 58, no. 4, pp. 639–707, 2008.

[85] C. Bierlich *et al.*, "A comprehensive guide to the physics and usage of pythia 8.3," *2022*, 2022.

[86] C. Bierlich, S. Chakraborty, N. Desai, L. Gellersen, I. Helenius, P. Ilten, L. Lönnblad, S. Mrenna, S. Prestel, C. T. Preuss *et al.*, "A comprehensive guide to the physics and usage of pythia 8.3," *SciPost Phys. Codeb.*, vol. 2022, 2022.

[87] "Reweighting heavy-flavor production fractions to reduce flavor modelling uncertainties for ATLAS," CERN, Geneva, Tech. Rep., 2022, all figures including auxiliary figures are available at https://ATLAS.web.cern.ch/ATLAS/GROUPS/PHYSICS/PUBNOTES/ATL-PHYS-PUB-2022-035. [Online]. Available: https://cds.cern.ch/record/2816367

[88] T. Gleisberg and C. S. Höche, "a new matrix element generator," 2008, jHEP 12 039, [hep-ph].

[89] F. Buccioni *et al.*, "Openloops 2," 2019, eur. Phys. J. C 79 866, [hep-ph].

[90] F. Cascioli, P. Maierhöfer, and S. Pozzorini, "Scattering amplitudes with open loops," 2012, phys. Rev. Lett. 108 111601, [hep-ph].

[91] A. Denner, S. Dittmaier, and L. Hofer, "Collier: A fortran-based complex one-loop library in extended regularizations," 2017, comput. Phys. Commun. 212 220, [hep-ph].

[92] R. D. Ball *et al.*, "Parton distributions for the lhc run ii," 2015, jHEP 04 040, [hep-ph].

[93] S. Schumann and F. Krauss, "A parton shower algorithm based on catani–seymour dipole factorisation," 2008, jHEP 03 038, [hep-ph].

[94] J.-C. Winter, F. Krauss, and G. Soff, "A modified cluster-hadronization model," 2004, eur. Phys. J. C 36 381.

[95] S. Höche, F. Krauss, M. Schönherr, and F. Siegert, "A critical appraisal of nlo+ps matching methods," 2012, jHEP 09 049, [hep-ph].

[96] S. Catani, F. Krauss, B. R. Webber, and R. Kuhn, "Qcd matrix elements + parton showers," 2001, jHEP 11 063.

[97] S. Höche, F. Krauss, M. Schönherr, and F. Siegert, "Qcd matrix elements + parton showers," 2013, the NLO case, JHEP 04 027, [hep-ph].

[98] R. Frederix and S. Frixione, "Merging meets matching in mc@nlo," *JHEP*, vol. 12, p. 061, 2012.

[99] C. Bierlich, A. Buckley, J. Butterworth, C. H. Christensen, L. Corpe, D. Grellscheid, J. F. Grosse-Oetringhaus, C. Gutschow, P. Karczmarczyk, J. Klein *et al.*, "Robust independent validation of experiment and theory: Rivet version 3," *SciPost Phys.*, vol. 8, 2020.

A MadGraph Plots

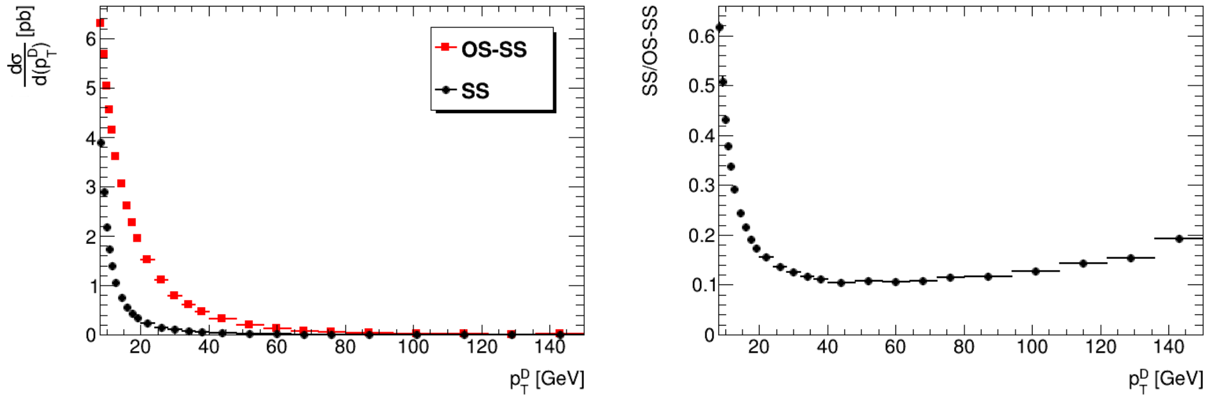

(a) (b)

Figure 42: Plots showing p_T^D in the W^+D^- channel (a) displays the SS charge symmetry in black and the OS-SS subtraction in red. (b) shows the corresponding ratio of SS/OS-SS.

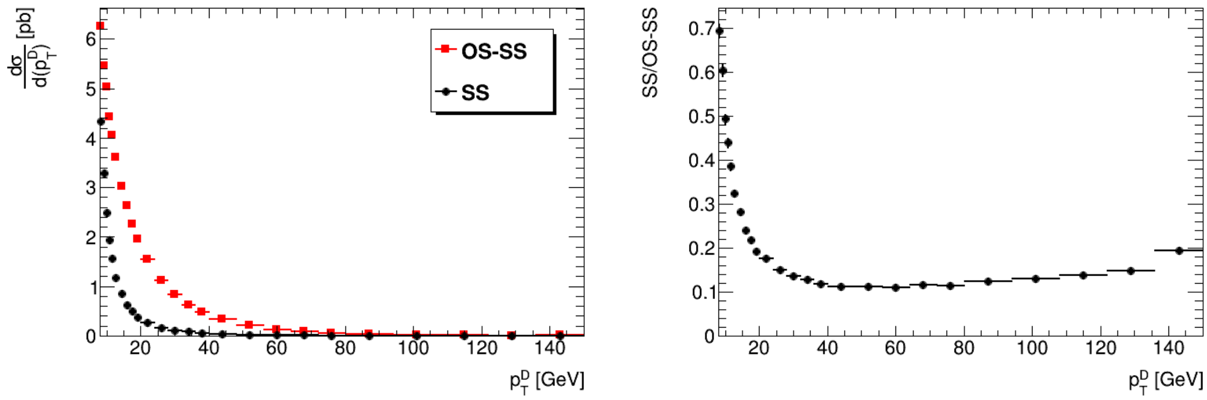

(a) (b)

Figure 43: Plots showing $p_T^{D^*}$ in the W^+D^{*-} channel (a) displays the SS charge symmetry in black and the OS-SS subtraction in red. (b) shows the corresponding ratio of SS/OS-SS.

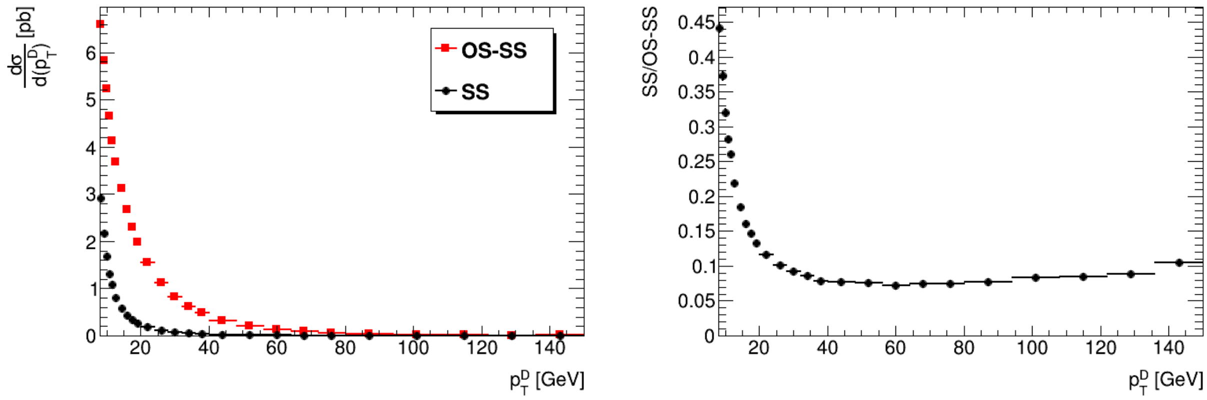

(a) (b)

Figure 44: Plots showing p_T^D in the W^-D^+ channel (a) displays the SS charge symmetry in black and the OS-SS subtraction in red. (b) shows the corresponding ratio of SS/OS-SS.

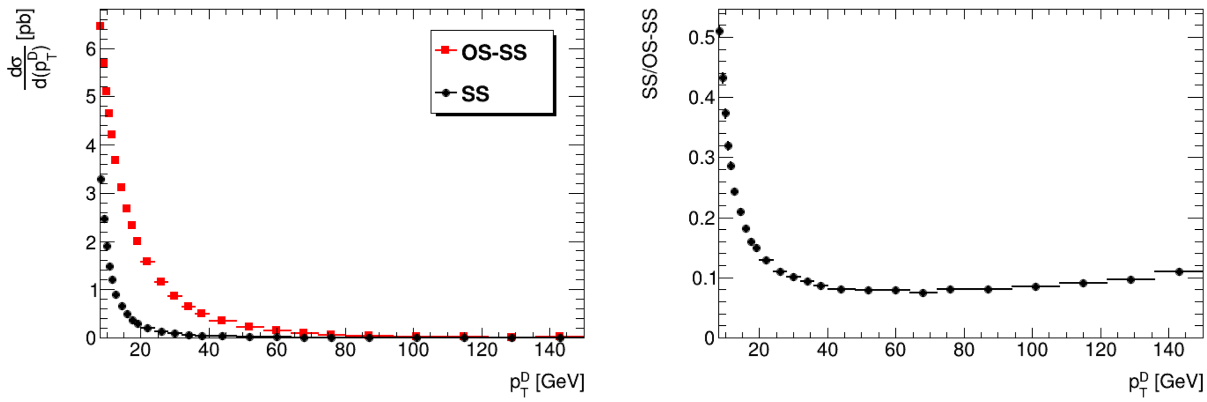

(a) (b)

Figure 45: Plots showing $p_T^{D^*}$ in the W^-D^{*+} channel (a) displays the SS charge symmetry in black and the OS-SS subtraction in red. (b) shows the corresponding ratio of SS/OS-SS.

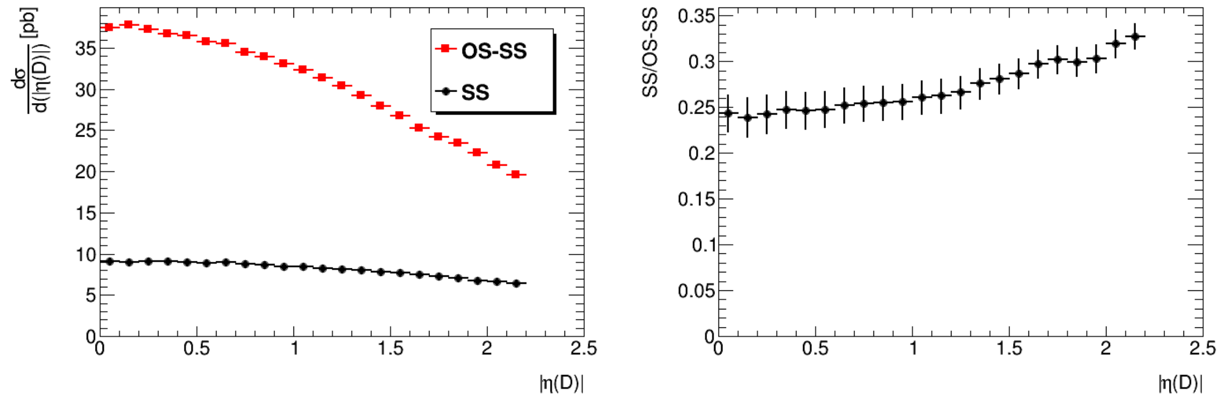

(a) (b)

Figure 46: Plots showing $|\eta(D)|$ in the W^+D^- channel (a) displays the SS charge symmetry in black and the OS-SS subtraction in red. (b) shows the corresponding ratio of SS/OS-SS.

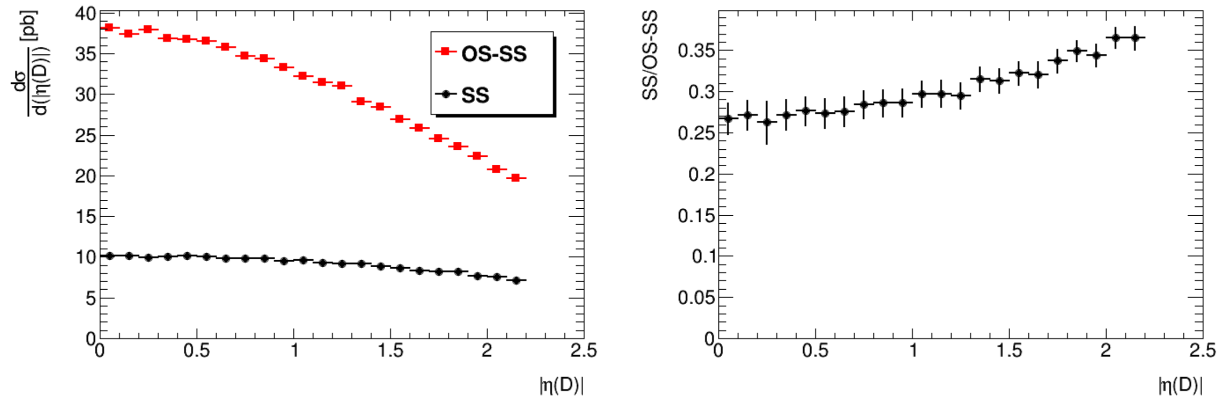

(a) (b)

Figure 47: Plots showing $|\eta(D^*)|$ in the W^+D^{*-} channel (a) displays the SS charge symmetry in black and the OS-SS subtraction in red. (b) shows the corresponding ratio of SS/OS-SS.

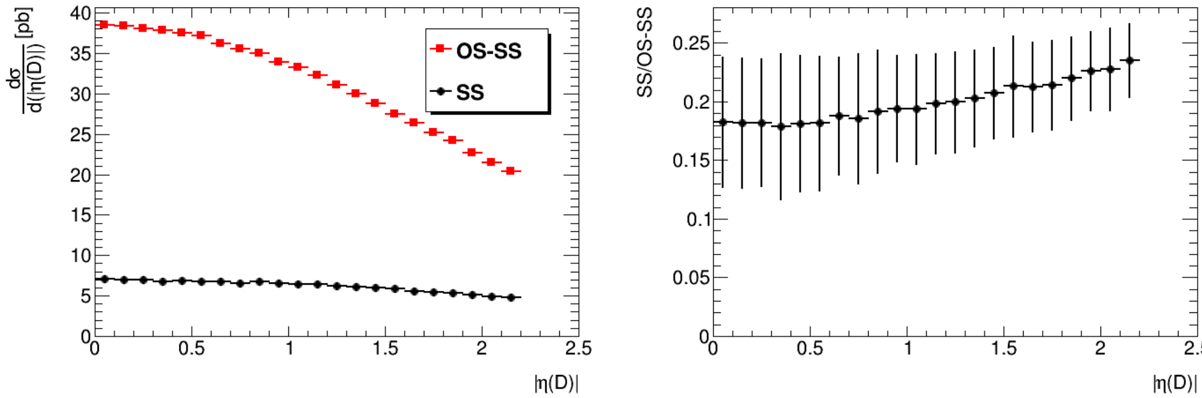

(a) (b)

Figure 48: Plots showing $|\eta(D)|$ in the W^-D^+ channel (a) displays the SS charge symmetry in black and the OS-SS subtraction in red. (b) shows the corresponding ratio of SS/OS-SS.

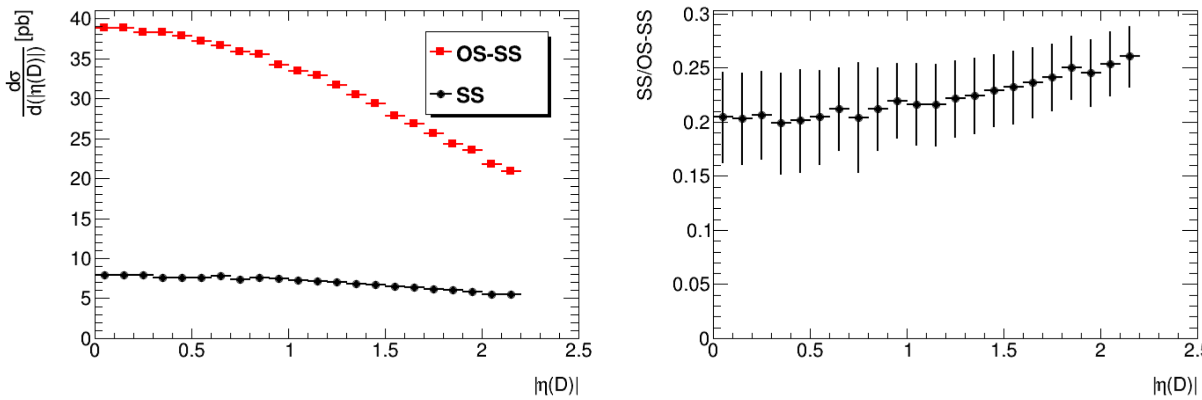

(a) (b)

Figure 49: Plots showing $|\eta(D^*)|$ in the W^-D^{*+} channel (a) displays the SS charge symmetry in black and the OS-SS subtraction in red. (b) shows the corresponding ratio of SS/OS-SS.

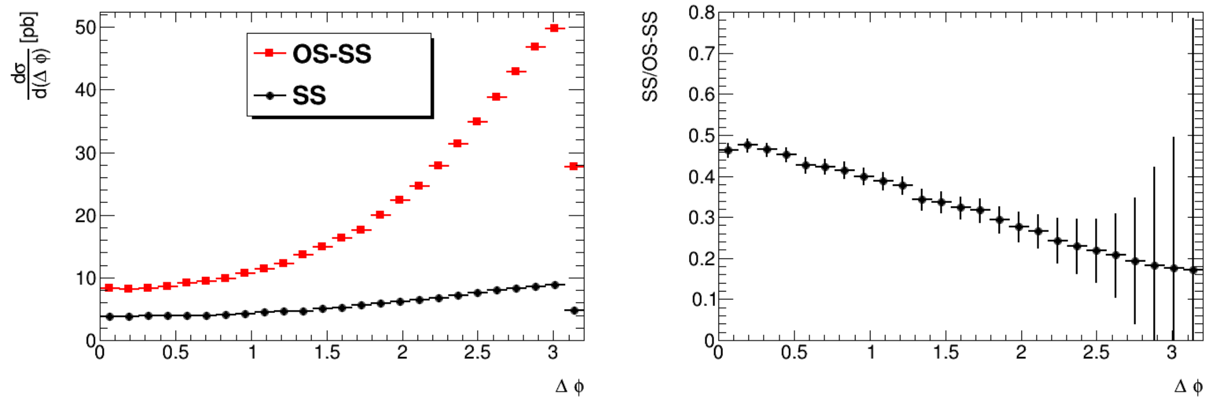

(a) (b)

Figure 50: Plots showing $\Delta\phi$ in the W^+D^- channel (a) displays the SS charge symmetry in black and the OS-SS subtraction in red. (b) shows the corresponding ratio of SS/OS-SS.

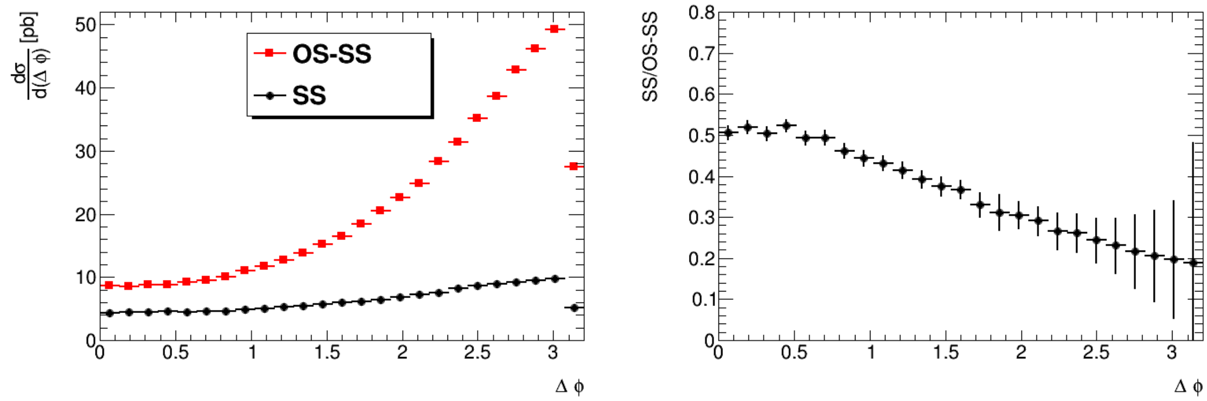

(a) (b)

Figure 51: Plots showing $\Delta\phi$ in the W^+D^{*-} channel (a) displays the SS charge symmetry in black and the OS-SS subtraction in red. (b) shows the corresponding ratio of SS/OS-SS.

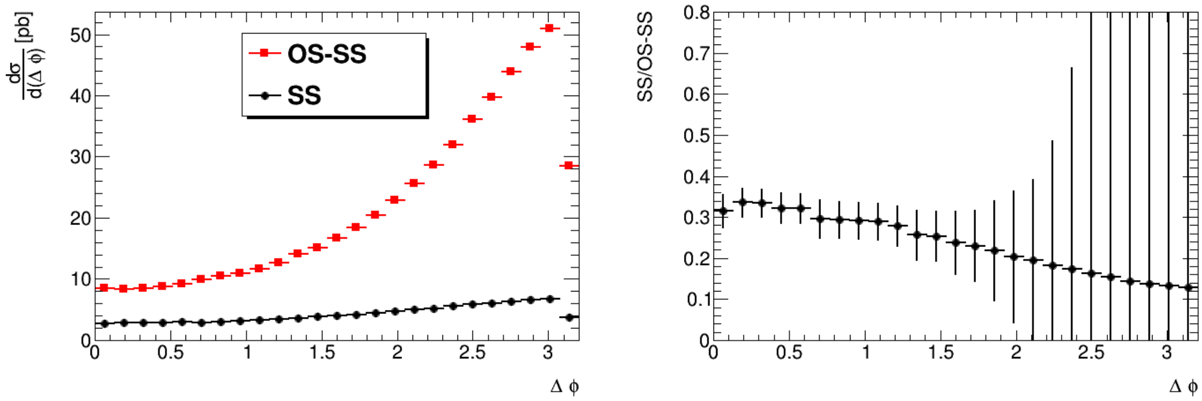

(a) (b)

Figure 52: Plots showing $\Delta\phi$ in the W^-D^+ channel (a) displays the SS charge symmetry in black and the OS-SS subtraction in red. (b) shows the corresponding ratio of SS/OS-SS.

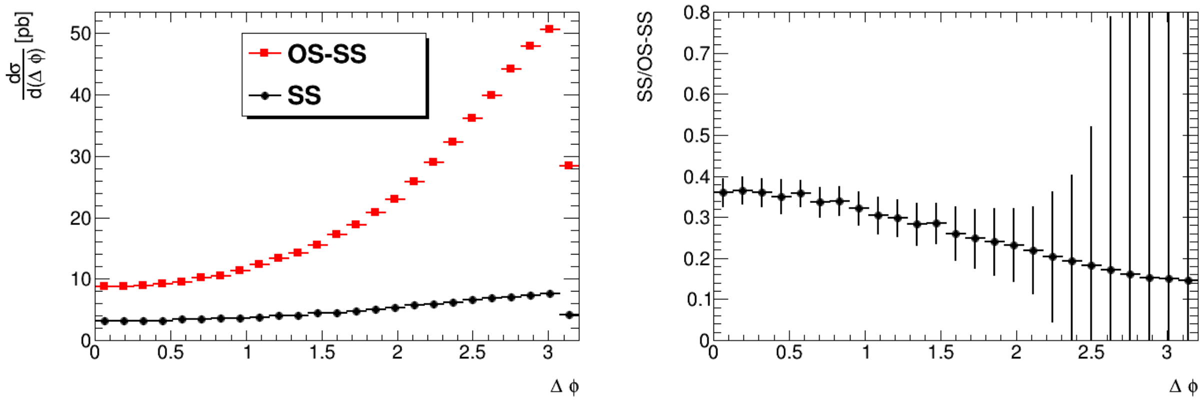

(a) (b)

Figure 53: Plots showing $\Delta\phi$ in the W^-D^{*+} channel (a) displays the SS charge symmetry in black and the OS-SS subtraction in red. (b) shows the corresponding ratio of SS/OS-SS.

B MadGraph Integrals

Table 16: Integrals of histograms for $p_T^{D^{(*)}}$ from MadGraph.

Channel	Charge	Integral			Ratio
		Total	Bin 1-12	Bin 13-25	
$W^- + D^+$	SS	13.60 ± 0.03	12.36 ± 0.03	1.2465 ± 0.0056	9.912 ± 0.092
	OS	82.709 ± 0.083	66.233 ± 0.083	16.477 ± 0.025	4.014 ± 0.045
	OS-SS	69.106 ± 0.088	53.876 ± 0.088	15.230 ± 0.026	3.54 ± 0.04
	SS/OS-SS	3.808 ± 0.013	2.739 ± 0.013	1.06870 ± 0.00061	2.562 ± 0.042
$W^+ + D^-$	SS	17.887 ± 0.035	16.213 ± 0.035	1.6744 ± 0.0064	9.684 ± 0.091
	OS	85.073 ± 0.083	68.837 ± 0.083	16.236 ± 0.025	4.240 ± 0.044
	OS-SS	67.186 ± 0.090	52.62 ± 0.09	14.562 ± 0.026	3.61 ± 0.04
	SS/OS-SS	5.310 ± 0.019	3.681 ± 0.019	1.62860 ± 0.00074	2.260 ± 0.023
$W^- + D^{*+}$	SS	15.329 ± 0.038	13.913 ± 0.038	1.4156 ± 0.0072	9.8 ± 0.1
	OS	85.270 ± 0.098	67.728 ± 0.098	17.542 ± 0.032	3.858 ± 0.048
	OS-SS	69.941 ± 0.105	53.81 ± 0.11	16.126 ± 0.033	3.336 ± 0.044
	SS/OS-SS	4.243 ± 0.019	3.105 ± 0.019	1.13790 ± 0.00074	2.727 ± 0.032
$W^+ + D^{*-}$	SS	20.152 ± 0.046	18.252 ± 0.046	1.9004 ± 0.0081	9.6 ± 0.1
	OS	87.928 ± 0.099	70.577 ± 0.099	17.351 ± 0.031	4.067 ± 0.051
	OS-SS	67.775 ± 0.109	52.33 ± 0.11	15.450 ± 0.032	3.384 ± 0.047
	SS/OS-SS	5.873 ± 0.028	4.193 ± 0.028	1.68070 ± 0.00089	2.498 ± 0.028

Table 17: Integrals of histograms for $|\eta(D^{(*)})|$ from MadGraph.

Channel	Charge	Integral			Ratio
		Total	Bin 1-12	Bin 13-25	
$W^- + D^+$	SS	13.603 ± 0.023	8.078 ± 0.023	5.53 ± 0.02	1.4 ± 0.1
	OS	82.709 ± 0.066	51.429 ± 0.066	31.281 ± 0.057	1.65 ± 0.02
	OS-SS	69.11 ± 0.07	43.35 ± 0.07	25.76 ± 0.06	1.682 ± 0.027
	SS/OS-SS	4.40 ± 0.22	2.24 ± 0.19	2.16 ± 0.12	1.04 ± 0.13
$W^+ + D^-$	SS	17.887 ± 0.027	10.561 ± 0.027	7.326 ± 0.023	1.44 ± 0.05
	OS	85.073 ± 0.067	52.782 ± 0.067	32.291 ± 0.054	1.634 ± 0.028
	OS-SS	67.186 ± 0.072	42.221 ± 0.072	24.965 ± 0.059	1.692 ± 0.036
	SS/OS-SS	5.965 ± 0.085	3.007 ± 0.068	2.96 ± 0.05	1.02 ± 0.05
$W^- + D^{*+}$	SS	15.33 ± 0.03	9.09 ± 0.03	6.236 ± 0.025	1.46 ± 0.08
	OS	85.270 ± 0.081	52.821 ± 0.081	32.448 ± 0.064	1.63 ± 0.03
	OS-SS	69.941 ± 0.086	43.729 ± 0.086	26.212 ± 0.068	1.669 ± 0.041
	SS/OS-SS	4.89 ± 0.18	2.50 ± 0.15	2.4 ± 0.1	1.0 ± 0.1
$W^+ + D^{*-}$	SS	20.153 ± 0.036	11.842 ± 0.036	8.31 ± 0.03	1.436 ± 0.049
	OS	87.93 ± 0.08	54.40 ± 0.08	33.531 ± 0.066	1.623 ± 0.031
	OS-SS	67.775 ± 0.088	42.555 ± 0.088	25.221 ± 0.072	1.69 ± 0.04
	SS/OS-SS	6.672 ± 0.079	3.347 ± 0.064	3.325 ± 0.046	1.007 ± 0.053

Table 18: Integrals of histograms for $\Delta\phi(\ell, D^{(*)})$ from MadGraph.

Channel	Charge	Integral			Ratio
		Total	Bin 1-12	Bin 13-25	
$W^- + D^+$	SS	13.603 ± 0.019	4.829 ± 0.019	8.774 ± 0.024	0.549 ± 0.059
	OS	82.709 ± 0.042	21.244 ± 0.042	61.465 ± 0.076	0.346 ± 0.004
	OS-SS	69.106 ± 0.046	16.416 ± 0.046	52.691 ± 0.079	0.312 ± 0.005
	SS/OS-SS	5.90 ± 60.81	3.59 ± 0.16	2.3 ± 60.8	1.56 ± 0.21
$W^+ + D^-$	SS	17.887 ± 0.022	6.443 ± 0.022	11.445 ± 0.028	0.563 ± 0.038
	OS	85.073 ± 0.044	22.355 ± 0.044	62.718 ± 0.074	0.357 ± 0.004
	OS-SS	67.186 ± 0.049	15.912 ± 0.049	51.273 ± 0.079	0.311 ± 0.005
	SS/OS-SS	8.07 ± 0.77	4.966 ± 0.069	3.10 ± 0.77	1.603 ± 0.114
$W^- + D^{*+}$	SS	15.329 ± 0.025	5.499 ± 0.025	9.83 ± 0.03	0.559 ± 0.025
	OS	85.270 ± 0.052	22.450 ± 0.052	62.820 ± 0.089	0.357 ± 0.004
	OS-SS	69.941 ± 0.058	16.951 ± 0.058	52.990 ± 0.093	0.320 ± 0.005
	SS/OS-SS	6.52 ± 192.05	3.96 ± 0.14	2.56 ± 192.05	1.547 ± 0.155
$W^+ + D^{*-}$	SS	20.153 ± 0.029	7.407 ± 0.029	12.746 ± 0.037	0.581 ± 0.058
	OS	87.928 ± 0.056	23.731 ± 0.056	64.197 ± 0.087	0.369 ± 0.004
	OS-SS	67.775 ± 0.063	16.324 ± 0.063	51.451 ± 0.095	0.317 ± 0.005
	SS/OS-SS	8.98 ± 0.39	5.561 ± 0.064	3.42 ± 0.38	1.6 ± 0.2

Acknowledgment

The bulk of my research took place at the University of California in Berkeley and the Lawrence Berkeley National Laboratory (LBNL). Each morning, as I passed by Robert Oppenheimer's former office, I was humbled by the opportunity to contribute, albeit in a tiny, rather miniscule way, to the advancement of science. At LBNL, the breathtaking view of the San Francisco Bay and the skyline of San Francisco from the Berkeley Hills served as a constant reminder of the honor it was to collaborate with such exceptional individuals in such a remarkable setting.
The majority of my writing endeavors were conducted at DESY (Deutsches Elektronen-Synchroton, English: German Electron Synchroton). During my time as a student in high school, I had the privilege of undertaking an internship at DESY during the school vacation. Even prior to this internship, my passion for physics was evident, but the atmosphere of the place and the values it embodied further solidified my commitment to dedicating my life to the field. Reflecting on my experiences fills me with gratitude and humility; it brings a smile to my face to think of my younger self's reaction to the realization that I now work in the very place that left such a profound impression on me.
I am deeply grateful for the immense fortune I have been granted, and I owe it to the support and guidance of certain individuals. At this juncture, I would like to extend my heartfelt thanks to them.

The person who has contributed most to the fact that I was able to write my bachelor thesis on such an exciting topic, with such wonderful people, in such beautiful places is **Kerstin Tackmann**. I would like to thank her first and foremost; for giving me this great opportunity to write this thesis, for her constant patience, her understanding, her explanations, her willingness to help me with every single problem or question and last but not least for the precious time she gave me. I am immensely grateful to her for giving me the opportunity to learn so many new things.
Kerstin's guidance and mentorship not only allowed me to pursue my academic interests, but also fostered my personal and professional development. I am deeply grateful for her invaluable insights, encouragement, and support, which have not only enriched my academic journey, but also shaped my aspirations for the future. I cannot express enough gratitude for her instrumental role in this work and I hope that with this thesis, I present her with a worthy piece of work.

In second place, I extend my sincere gratitude to my second supervisor, **Marjorie Shapiro**. Her profound professional expertise and enlightening explanations have been invaluable throughout this journey. Her unwavering support and willingness to guide me have been instrumental in the completion of this work. Whether through our insightful discussions in Berkeley or via Zoom, her mentorship has consistently propelled the progress of this research forward. I am deeply grateful for her dedication and contribution to this endeavor.

I would also like to thank **Heather Gray** for allowing me to be part of her research group and for the effort she put into making this possible.

I extend my gratitude to **Miha Muškinja**, whose guidance and mentorship during my time in Berkeley not only introduced me to the work environment and analysis but also served as a source of inspiration and motivation.

Additionally, I am thankful to **Tomohiro Yamazaki**, whose consistent provision of insightful answers to my inquiries and contribution of innovative ideas greatly enhanced the development of the analysis.

I would also like to thank my **friends** that I met during my studies in Hamburg. They supported and motivated me during the time I worked on my bachelor thesis as well as during the study of physics in general, which was not only an intellectually and academically satisfying part of my life, but they also made the time extremely pleasant from a social and leisure point of view.

I also want to cordially thank my **family**, who as always has supported me greatly in various ways, also in this work. Their unwavering encouragement, whether it was through emotional support during challenging times or practical assistance with everyday tasks, has been invaluable. Their belief in my abilities and their sacrifices to ensure my success have been a constant source of motivation. I am profoundly grateful for their love, understanding, and unwavering support.

Eigenständigkeitserklärung

Hiermit bestätige ich, dass die vorliegende Arbeit von mir selbstständig verfasst wurde und ich keine anderen als die angegebenen Hilfsmittel, insbesondere keine im Quellenverzeichnis nicht benannten Internetquellen, benutzt habe und die Arbeit von mir vorher nicht in einem anderen Prüfungsverfahren eingereicht wurde.
Die eingereichte schriftliche Fassung entspricht der auf dem elektronischen Speichermedium.
Ich bin damit einverstanden, dass diese Bachelorarbeit veröffentlicht wird.

Declaration of Authenticity

I hereby confirm that I have written this thesis independently and that I have not used any aids other than those specified, in particular no internet sources not mentioned in the list of sources, and that I have not previously submitted the thesis in another examination procedure.
The written version submitted corresponds to the version on the electronic storage medium.
I agree that this Bachelor's thesis may be published.

Hamburg, 16 April 2024

B. Bigalke

Birger J. M. Bigalke